EIEлектротехніка і лектромеханіка

Electrical Engineering & Electromechanics

Електротехніка. Визначні події. Славетні імена
Електричні машини та апарати
Електротехнічні комплекси та системи.
 Силова електроніка
Теоретична електротехніка та електрофізика
Техніка сильних електричних та магнітних полів.
 Кабельна техніка
Електричні станції, мережі і системи

ISSUE 6/2017

TABLE OF CONTENTS

M.I. Baranov

AN ANTHOLOGY OF THE DISTINGUISHED ACHIEVEMENTS IN SCIENCE AND TECHNIQUE. PART 41: COMPOSITE MATERIALS: THEIR CLASSIFICATION, TECHNOLOGIES OF MAKING, PROPERTIES AND APPLICATION DOMAINS IN MODERN TECHNIQUE

***Purpose.** Preparation of brief scientific and technical review about the state, achievements and prospects of development of works domestic and foreign scientists-specialists on materials and technologists in area of development and creation of composite materials (compos). **Methodology.** Scientific methods of collection, analysis and analytical treatment of the opened scientific and technical information of world level in area of studies about materials, related to development of basic technologies of making of new perspective compos and their application in a modern technique. **Results.** A state-of-the-art scientific and technical review is resulted about the state, achievements and prospects on the future in the world of researches on development and creation of new metallic and non-metal compos, possessing as compared to traditional homogeneous materials substantially more high physical and mechanical descriptions. Classification of compos is executed. Technologies of making of basic types of compos, findings a practical wide use enough in an aviation and space-rocket technique, engineering and row of the special areas of modern technique are briefly described. Main properties of basic types of compos and their advantage are indicated before traditional metals and alloys. The basic failings and technical application for today of different compos domains are resulted. Considerable progress is marked in technologies of making and volumes of the use in the front-rank areas of technique of compos. The possible nearest prospects are indicated in the use of compos on the future in a number of stormy developing in the whole world technical areas. **Originality.** Systematization of the scientific and technical materials, devoted the basic results of works on being in 2016 year of domestic and foreign specialists in area of development, making and application in the modern technique of the most perspective types of compos, known from the sources opened in outer informative space is executed. **Practical value.** Popularization and deepening for students, engineers and technical specialists and research workers of scientific and technical knowledges in the necessary area of development, creation and application in the modern technique of compos, extending their scientific range of interests and further development of scientific and technical progress in human society.* References 22, figures 6.*
Key words: **composite materials, basic technologies of receipt of compos, advantages of compos before traditional materials, world achievements in creation of compos.**

Приведен научно-технический обзор о состоянии, достижениях и перспективах развития работ отечественных и зарубежных ученых-материаловедов в области разработки и создания композиционных материалов, обладающих по сравнению с традиционными однородными материалами существенно более высокими физико-механическими характеристиками. Описаны основные классификации, технологии получения, свойства и области применения подобных материалов-композитов в технике. Библ. 22, рис. 6.
Ключевые слова: **композиционные материалы, основные технологии получения композитов, преимущества композитов перед традиционными материалами, мировые достижения в создании композитов.**

Introduction. Further progressive development in the world of modern technology in mechanical engineering, electrical engineering, electric power, instrument-making, aviation and rocket building industries requires the creation of a variety of new materials with their increasingly high performance properties. Scientists and specialists from many countries of the world engaged in the study of behavior in the field of material science and experimental determination of the physical and technical characteristics of various metals and alloys have long concluded that the creation of inhomogeneous solid compositions with a correct choice of their initial components may lead to new materials with their significantly improved mechanical characteristics compared to known homogeneous materials. Similar materials in materials science are called composite. According to modern concepts, *composite material* (CM) is an artificially created heterogeneous solid material consisting of two or more components with a clear interface between them [1]. One of the «oldest» and still used throughout the world of CM is a «*bulat*» containing the finest layers (sometimes strands) of high-carbon steel, which are «glued together» by soft low-carbon iron [1]. After the reasons for their plasticity, elasticity and strength were scientifically explained in metal science and in the physics of metals, and the main physicochemical pathways of a noticeable increase (strengthening) of the indices of these physical properties were established [2] in the leading material science laboratories of the world, intensive systemic the development of new non-metallic materials with their significantly increased physicomechanical characteristics. In the last decades, materials scientists of the industrially developed countries of the world are actively engaged in scientific and technical search for new CMs, purposefully creating the most promising for

their physico-mechanical properties for a number of rapidly developing areas of modern technology and relatively cheap in the production of CM (compos).

The goal of the paper is compilation of a brief scientific and technical review on the state, achievements and prospects for the development of materials research in the world in the field of development and production of composites.

1. Classification of composites. In most CMs, which are usually multicomponent materials, the components (components) used in them can be divided into a matrix (continuous throughout the volume of the CM plastic base) and included in it reinforcing elements (interrupted by the volume of CM reinforcing fillers) that have high strength, rigidity, heat resistance and other physical properties [1-3]. We note that the CM matrix ensures the monolithic nature of the created material, imparts the required shape to the created product, transfers the mechanical stress from one part of the filler medium to the other, protects the reinforcing reinforcement from mechanical damage and provides mechanical and other resistance to overall external forces. Specialists (materials scientists and technologists), varying the compositions of matrices and fillers, their percentage ratio and the spatial orientation of the filler reinforcement in the volume of CM, can now obtain a very wide spectrum of CM with the required set of their properties [1-3]. In this connection, all the composites by the form of the matrix used in the CM are now classified into [1]:

- composites with a polymer matrix;
- composites with a metal matrix;
- composites with a ceramic matrix;
- composites with an oxide-oxide system.

By the type of filler used in the CM (reinforcing component), existing and newly created composites are classified into [1]:

- fibrous composites (reinforcing components - fibrous structures of non-metals and metals);
- layered composites (reinforcing components - separate layered structures, Fig. 1);
- composites such as «filled plastics» (reinforcing components - nano- and microparticles);
- bulk composites having homogeneous dispersed non-metallic and metal structures;
- skeletal composites in which the original structures are filled with a binder.

According to the type of reinforcing filler, fibrous CM are classified into the following groups [2]:

- fiberglass with glass fibers;
- carbon fibers with carbon fibers;
- boron fibers with boron fibers;
- organic fibers with synthetic threads.

In addition, the CM according to the geometry of the reinforcing element-filler included in their composition is divided into the following main groups [4, 5]:

- with zero-dimensional fillers (structural reinforcements), whose dimensions in three spatial dimensions are of the same order;
- with one-dimensional fillers, one of the sizes of which considerably exceeds the other two;
- with two-dimensional fillers, any two sizes which significantly exceed the third.
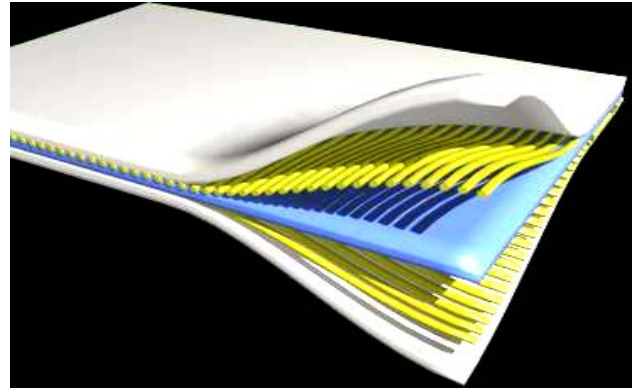
Fig. 1. Layout of individual layers in the CM [1]

According to the arrangement of the reinforcing element-filler, CMs are divided into such groups [4]:

- with an uniaxial (linear) arrangement of the filler reinforcement in the matrix in the form of parallel fibers, filaments and filamentary single crystals;
- with a biaxial (planar) arrangement of reinforcing filler, mats from filamentary single crystals and metal foils in a matrix with a parallel arrangement of their planes;
- with a three-axial (three-dimensional) arrangement of reinforcing filler and absence of a preferred direction in its arrangement.

According to the physical nature of their components, CMs are divided into the following large groups [4, 5]:

- composites containing components from various metals or alloys;
- composites containing within themselves components from various inorganic compounds (for example, oxides, carbides, nitrides, etc.);
- composites containing components from nonmetallic elements (including carbon, boron, etc.);
- composites containing components from organic compounds (for example, epoxy, polyester, phenolic resins and other chemical compounds).

As we see, CMs have a rather extensive classification. Below we will dwell in more detail on some of these composites.

2. The main technologies for manufacturing composites. Let us consider a number of composites, indicated above.

2.1. Fibrous composites. The mechanical characteristics of such CM are determined by the properties of a large number of parallel continuous fibers used in their composition. In each layer, the CM fibers

can be woven into a fabric, which is an original shape whose dimensions correspond to the geometric parameters of the final material [1-5]. The matrix of such a composite should redistribute mechanical stresses between reinforcing fibers. Therefore, the strength and modulus of elasticity of the fibers used in such a composite must be significantly greater than the strength and modulus of elasticity of the matrix. Rigid reinforcing fibers perceive the mechanical stresses that occur in the composite when it is loaded with force, and also give it strength and rigidity in the direction of fiber orientation. For example, boron fibers, as well as fibers of refractory compounds (for example, carbides, nitrides, borides and oxides) with high strength and modulus of elasticity are used to harden aluminum, magnesium and their alloys in this case. Often used as a fiber wire of high-strength steels [1-5]. For the CM under consideration, when reinforcing titanium and its alloys, molybdenum wire, sapphire fibers, silicon carbide and titanium boride are used. The increase in the heat resistance of nickel alloys is achieved by reinforcing them with tungsten or molybdenum wires [1-5]. Metal fibers are also used in those cases where high values of thermal conductivity and electrical conductivity are required for the composite to be created. Prospective reinforcing fillers for high-strength and high-modulus fibrous CM are filamentary crystals of aluminum oxide and nitride, silicon carbide and nitride, boron carbide, etc. [1-5]. Composites on a metal base have high strength and heat resistance. At the same time, they are not very plastic. However, the reinforcing fibers in the CM reduce the propagation speed (on the composite) of the cracks that originate in the matrix. This almost completely eliminates the sudden brittle failure of CM. A distinctive feature of fibrous uniaxial CM is their anisotropy of mechanical properties along and across fibers and a low sensitivity to mechanical stress concentrators. The anisotropy of the properties of *fibrous composites* is taken into account when constructing machine parts (apparatus) from them to optimize the properties of CM by matching the resistance field with the fields of mechanical stresses in it. It was found that the reinforcement of aluminum, magnesium and titanium alloys with continuous refractory fibers of boron, silicon carbide, titanium boride and aluminum oxide significantly improves their heat resistance [1-5]. Thus, aluminum alloys reinforced with boron fibers can be reliably operated at temperatures up to (450-500) °C instead of (250-300) °C [1-5]. The main disadvantage of composites with one- and two-dimensional reinforcement by their fibers is the low resistance of CM to the interlayer shear and transverse breakage. This is deprived of materials with bulk fiber reinforcement [1-5].

2.2. Disperse-hardened composites. Unlike fibrous CM in *dispersed-hardened composites*, the matrix is the main element that carries an external force load, and their fillers (dispersed particles) inhibit the motion of dislocations in it (the matrix). In such CM, high strength is achieved at a particle size (10-500) nm, and also with an average distance between them (100-500) nm and uniform distribution of them in the matrix [1-5]. In these composites, the strength and high-temperature strength, depending on the volume content of the strengthening phases in their matrix, do not obey the additivity law. The optimal content of the second phase in the matrix for different metals in these CMs is not the same, but usually does not exceed (5-10) % of the volume of the matrix material [1]. The use of stable refractory compounds (for example, thorium, hafnium, yttrium oxides, complex oxides compounds and rare earth metals) that do not dissolve in the matrix metal of the composite as hardening phases allows preserving the high strength of the CM material to temperatures approaching the melting temperature of the matrix metal [1]. In this regard, such CM are most often used as heat-resistant materials. Dispersion-hardened composites can be obtained on the basis of the majority of metals and alloys currently used in the technology (for example, aluminum, magnesium, nickel, copper, etc.) [1-5]. The most widely used similar CMs are aluminum-based alloys – SAP (sintered aluminum powder with Al_2O_3 oxide) [1]. The density of these CM is almost equal to the density of aluminum. They are not inferior to it for corrosion resistance and can even replace titanium and corrosion-resistant steels when operating in the temperature range (250-500) °C. For long-lasting strength, they exceed the deformable aluminum alloys. Thus, the long-term strength for alloys of the SAP-1 and SAP-2 type at 500 °C is (45-55) MPa [1]. According to materials scientists, there are great prospects for nickel dispersed-hardened materials. They found that nickel-based alloys with (2-3) % thorium dioxide or hafnium dioxide had the highest heat resistance (1-5). Wide-range alloys of the type ВДУ-1 (nickel hardened with thorium dioxide), type ВДУ-2 (nickel hardened with hafnium dioxide) and ВДУ-3 type (nickel matrix Ni plus 20 % by volume of chromium Cr, hardened with thorium oxide ThO). These alloys have high heat resistance. It should be noted that the introduction to these CMs (5-10) % reinforcing fillers (refractory oxides, nitrides, borides and carbides) leads to an increase in the resistance of their metal matrix to force loads. The effect of increasing the strength of the material is comparatively small. However, it is valuable here to increase the heat resistance of the resulting composite as compared to the original matrix. Thus, the introduction of fine-dispersible powders of thorium oxide or zirconium oxide into the heat-resistant chromium-nickel alloy allows to increase the temperature at which products from this alloy are capable of prolonged operation, from 1000 to 1200 °C [1-5]. We will point out that dispersed-hardened metal composites are obtained by introducing filler powder into the molten metal or by powder metallurgy methods [1-5]. Dispersion-hardened CM, as well as fibrous composites, are resistant to softening with an

increase in the temperature acting on them and to the duration of exposure to the force loading [1-5].

2.3. Fiberglass. This composite is a composition consisting of a synthetic resin that is a binder and a fiberglass reinforcing filler. In this case, continuous or short glass fibers are usually used as the filler [1, 2]. It was found that the strength of glass fibers increases sharply with a decrease in its diameter. This feature is explained by the elimination of the effect on the strength properties of thin glass fibers of irregularities and cracks occurring in thick (with a large cross section) fiberglass. We note that the properties of glass fibers also depend on the content of alkali in its composition. The best strength parameters are for alkali-free glasses of aluminoborosilicate composition [1-5]. Glass fibers are usually made in the form of yarns, bundles (rovings), glass fabrics (Fig. 2), glass mats and chopped fibers [1]. Binder in these CM is polyester, phenol-formaldehyde, epoxy and silicone resins, polyimides, aliphatic polyamides, polycarbonates, etc.

Fig. 2. General view of a fragment of the original glass fiber fabric of the type Parabeam 3D Glass fabric consisting of two woven horizontally placed parallel glass plates connected to each other by vertical glass worm and forming the so-called «sandwich-glass structure» [6]

Non-oriented glass fibers contain as a filler a short fiberglass. This makes it possible to press the details of complex shapes, including metal reinforcement [1]. In this case, the CM is obtained with isotropic strength characteristics, which are much higher than for press powders. Known representatives of such a composite are glass fibers of the АГ-4В type, as well as the DGF type (dosing glass fibers) [1-6]. They are widely used for the manufacture of power electrical components and parts of engineering products (for example, spools, seals of electric pumps, etc.). When these unsaturated polyesters are used as binder in these glass fibers, premixes like ПСК (pasty) and prepregs of the type АП and ППМ (based on the glass mat) are obtained [1]. Prepregs can be used for making light large-sized products of simple shapes (for example, car bodies, boat hulls and a number of devices) [1-6].

Oriented glass fibers contain a filler-reinforcing agent in the form of long glass fibers located in the CM oriented with separate strands and carefully glued together with a binder. Such a technology of their manufacture provides, in comparison with nonoriented glass fibers, a higher strength of the resulting glass fiber reinforced plastic [1-6]. These CMs can reliably operate under temperatures acting on them from «minus» 60 °C up to «plus» 200 °C. They are able to withstand tropical atmospheric conditions and large inertial overloads [1]. It is known that penetrating ionizing radiation has little effect on their mechanical and electrical properties.

2.4. Carbon fiber. This kind of composite contains a binder polymeric matrix (based on phenol-formaldehyde or other resin) and a carbon fiber reinforcing filler (Carbon fiber) [1-6]. Carbon fiber is a new material consisting of thin filaments with a diameter of 3 to 15 μm, formed predominantly by carbon atoms. The carbon atoms (carbon) in these filaments are combined into microscopic crystals aligned parallel to each other. Alignment of these crystals gives the carbon fiber greater tensile strength. Carbon fibers are characterized by high tension force, low specific gravity, low coefficient of temperature expansion and chemical inertness [7]. Carbon fibers are obtained from synthetic and natural fibers based on cellulose, copolymers and acrylonitrile [1, 7]. When they are made, heat treatment of the fiber is used. It is usually carried out in three stages [7]: stage 1 – oxidation at temperature of 220 °C; stage 2 – carbonization at temperatures (1000-1500) °C; stage 3 – graphitization at temperatures (1800-3000) °C). This technology leads to the formation of fibers characterized by a high content of carbon in them (up to 99.5 % by mass). The high binding energy of atoms in carbon fibers allows them to retain their strength at very high temperatures (in a neutral medium up to 2200 °C), and also at low temperatures [1-7]. From the oxidation of the surface, carbon fibers are protected by protective pyrolytic coatings. Unlike the glass fibers of carbon fiber, because of the low values of their surface energy, they are poorly wetted by the binder (matrix) used in the technologies for their production. Therefore, these fibers are etched before they are filled with a binder [1, 7]. This increases the degree of activation of carbon fibers by the content of the carboxyl group on their outer surface. Because of this, the interlayer shear strength for carbon plastics increases 1.6-2.5 times [1]. In addition, in the manufacture of the CMs under consideration, whiskerization of the filamentary carbon crystals with titan TiO is used, which provides an increase in the interlayer stiffness of carbon plastics up to two times and the strength is almost 2.8 times [1]. Often in the manufacture of *carbon fiber* they use spatially-reinforced structures. In this case, synthetic polymers serve as bonding agents (matrices), which also determines the name of the resulting composites-polymer carbon fibers. In the case where synthetic polymers are subjected to pyrolysis during the manufacture of CM, the resulting composites are called coking carbon fibers. When used in the technology of production of the pyrolytic carbon composites under

consideration, the CM obtained with it is called pyrocarbon carbon fiber [7].

Epoxyphenolic carbon fiber type КМУ-1л can operate for a long time at temperatures up to 200 °C. Carbon fiber type КМУ-3 and КМУ-2л are obtained on the basis of epoxy anilinoformaldehyde binder, which serves as a polymer matrix. These composites are considered to be the most technologically advanced carbon fiber. They can be reliably operated at temperatures up to 100 °C. Carbon fiber type КМУ-2 and КМУ-3л based on polyamide binder can be used at temperatures up to 300 °C. Carbon fibers are characterized by high statistical and dynamic fatigue resistance. They retain this property at normal and low temperatures (high thermal conductivity of the fiber prevents self-heating of the CM due to internal friction). They are water and chemically resistant. After the exposure of X-rays in air, their properties do not practically change [1-7].

Currently, one of the directions in obtaining new CM is the production of carbon fiber with a carbon matrix. At temperatures (800-1500) °C, carbonized carbonates are formed, and at (2500-3000) °C, graphitized carbon fibers are formed [1, 7]. To produce pyrocarbon materials, the reinforcement is laid out according to the shape of the article and placed in an oven through which an gaseous hydrocarbon is passed through the atmosphere (usually methane CH_4). Under a certain regime (temperature 1100 °C and residual pressure 2660 Pa), methane decomposes and the resulting pyrolytic carbon deposits on the reinforcing fiber, binding them. It should be noted that the coke formed during the pyrolysis of the binder has a high adhesion strength to the carbon fiber. In this regard, the CM obtained in this way has high mechanical and ablative properties, as well as high resistance to thermal shock. Carbon fiber with a carbon matrix of the type КУП-ВМ on the strength and toughness is 5-10 times higher than special graphites [1, 7, 8]. When heated in an inert atmosphere and vacuum, it retains its strength to temperatures of about 2200 °C. In air, it oxidizes, starting at 450 °C, and requires a protective coating.

The main advantages of carbon fibers in front of fiberglass are their lower density and higher modulus of elasticity [7]. Carbon plastics are light, strong and have practically zero coefficient of linear expansion. All types of carbon plastics conduct electricity well through themselves. High-temperature parts of rocket engines and high-speed aircraft, brake shoes and disks for jet planes and reusable spaceships and parts of electrothermal equipment are made of high-temperature carbon fiber [8].

2.5. **Boron fibers.** This CM is a composition made of a polymeric binder (matrix) and boron fibers (filler). *Boron fibers* (*boron plastics*) are distinguished by their high compressive strength, shear and shear, low creep, high hardness and elastic modulus, and thermal conductivity and electrical conductivity [1-8]. The

cellular microstructure of boron fibers provides high strength of the CM at shear at the interface between them and its matrix. In the production technology of this composite, in addition to the continuous boron fiber, complex boron glasses are also used, in which several parallel boron fibers are intertwined with glass fiber that betrays them to form stability. The use of bored leaflets facilitates the technological process of manufacturing the CM under consideration. Modified epoxy and polyamide binders are used as matrices for the production of boron fibers. Boron fibers of type КМБ-1 and КМБ-1к are designed for continuous operation at temperatures up to 200 °C, while КМБ-3 and КМБ-3к types do not require high pressure during processing and can operate at temperatures not higher than 100 °C. КМБ-2к type boron fiber is operable at temperatures up to 300 ° C [1-8]. Boron fibers have high rates of fatigue resistance. They are resistant to the effects of penetrating radiation, water, organic solvents and various fuels and lubricants. In addition, for boron fibers, the compressive strength is 2-2.5 times greater than for carbon fiber strands [1]. At the same time, the high fragility of boron plastics makes their processing difficult and imposes restrictions on the shape of products obtained from boron fibers. The technological feature of obtaining boron fibers is that the necessary boron for them is precipitated from boron chloride to a tungsten matrix-substrate, the cost of which can reach up to 30 % of the cost of the boron fiber obtained [1, 8]. In this connection, the cost of boron fiber is today high and reaches USD 400 / kg [8].

2.6. Organic fibers. These CMs are composites consisting of a polymeric binder (matrix) and reinforcing agents (fillers) in the form of synthetic fibers. *Organic fibers* have low mass, relatively high values of specific strength and rigidity. They are stable under the action of alternating loads and a sudden change in temperature [1-8]. In organic fibers the values of the modulus of elasticity and the temperature coefficients of linear expansion of the reinforcing agent (synthetic fibers) and the binder (polymeric compounds based on epoxy and other resins) are similar. Therefore, during their manufacture, the components of the binder are diffused into the fiber used and the chemical interaction between them. The structure of the resulting synthetic material is practically defect-free [1, 7]. Its porosity does not exceed (1-3) %. For comparison, note that in other CMs the porosity reaches values (10-20) % [1, 7]. The impact strength of organic fibers is high and equal to about (400-700) Pa·[1, 7]. Hence, the stability of the mechanical properties of the organic fibers follows with a sharp temperature difference, the impact of shock and cyclic force loads. Organic fibers are resistant to the action of corrosive environments and the humid tropical climate. Their dielectric properties are high, and the thermal conductivity is low. Most organic fibers can work for a long time at temperatures (100-150) °C. Based on the polyamide binder and polyoxadiazole fibers, they are able

to function reliably at temperatures (200-300) °C [1, 7]. A disadvantage of these composites is their relatively low mechanical strength under compression and high creep.

2.7. Polymer nanocomposites. This type of CM is polymers filled with nanoparticles that interact with the polymer matrix not at the macrolevel (as in the case of conventional composites), but at the molecular level [9]. Due to this interaction, a composite is formed, which has a high adhesion strength of the polymer matrix to nanoparticles. As is known, nanoparticles have linear dimensions of not more than 100 nm in one of three spatial dimensions [10]. An analysis of recent domestic and foreign studies indicates a high potential for research in the field of *polymeric nanocomposite materials* [9]. Unfortunately, these works contain a lot of technological «know-how» and access to them is currently extremely limited [2].

2.8. Intermetallides. Such a name in materials science received new chemical compounds based on compositions of the type «titanium-aluminum», «nickel-aluminum», etc. [9]. It is believed that it is *intermetallics*, as a new class of structural materials that can lead to revolutionary solutions in the development and creation of promising products for rocket and space technology. These composites have a relatively low density - from 3.7 to 6.0 g/cm^3 and have high heat resistance (up to 1200 °C) [9]. In addition, they are characterized by high levels of corrosion resistance, heat resistance and wear resistance. Intermetallic titanium-based alloys can operate up to 850 ° C without protective coatings. Alloys based on nickel – up to 1500 °C [9]. In the opinion of specialists, the use of intermetallic compounds in propulsion systems (for example, for the rotor, stator, impeller, valve group, uncooled nozzles, etc.) will increase the specific thrust of the engines by (25-30) %, and also provide a reduction in the mass of the designs of propulsion systems to 40 % [2, 9].

2.9. Eutectic composites. This type of CM is an alloy of a eutectic or close to eutectic composition, in which oriented crystals formed in the process of directional crystallization act as a strengthening phase [8]. Unlike ordinary CM, *eutectic composites* are produced in one technological operation. A directional oriented crystal structure can be obtained at the final stage of the product release. The geometric shape of the crystals formed during the corresponding operation can be in the form of fibers or plates. Directed crystallization methods already produce composites based on aluminum, magnesium, copper, cobalt, titanium, niobium and other chemical elements [8]. Therefore, these composites can be used in a wide range of temperatures [2].

2.10. Composites based on ceramics. Reinforcement of ceramic materials (matrices) with fibers, as well as metallic and ceramic dispersed particles, allows obtaining high-strength composites [8]. As a reinforcing filler, metal fibers are often used. In this case,

the tensile strength increases insignificantly, but the resistance to thermal shocks increases significantly. Because of this, the ceramic material cracks less during its heating. The properties of the CM thus obtained will depend on the ratio of the thermal expansion coefficients of its matrix and filler. Reinforcement of ceramics with dispersed metal particles provides a new type of material - *cermet* which has increased mechanical resistance, thermal conductivity and resistance to thermal shocks [8, 11]. In both cases, *ceramic composites* are produced by hot pressing (tableting with subsequent sintering under pressure) or by slip casting (filler fibers are poured with a slurry of matrix material, which after drying is sintered in special furnaces) [2, 11].

2.11. Functional gradient materials. Such new types of composites as *functional gradient materials* (FGM) are alloys consisting of hard grains of carbides, nitrides and borides of transition metals (for example, tungsten carbide, titanium carbide, titanium carbonitride, titanium diboride, etc.) forming a strong continuous framework matrix), and a metal bond (from cobalt, nickel, titanium, aluminum, etc.), the content of which varies continuously in the volume of such CM [12]. Practical realization of the layered structure of FGM is ensured by layer-by-layer pressing of carbide press powders with different contents of the above-mentioned metal bond and different grain sizes of the solid phase followed by vacuum sintering. In this case, mass transfer of the metal bond during the liquid-phase sintering from a layer with a large grain size into a layer with a smaller grain size, leading to a gradient of its content in the alloy, will be observed in the CM under consideration. Such a CM manufacturing technology makes it possible to control the gradient in the «frame-binder» system for the composite under consideration by changing its (metal bond) concentration in the pressed layers of FGM. As a result, FGM have the properties of both a hard alloy and a metal. Therefore, such composites have high hardness, thermal stability and high impact strength [2, 12].

3. Basic properties and technical characteristics of composites. Let us dwell on the advantages, properties and disadvantages of a number of these CMs.

3.1. Advantages of composites. The main advantage of CM in comparison with traditional structural materials is that during the manufacture of a composite, the material and the construction of the product are created simultaneously [1-5]. CM specialists are always created for specific technical tasks and for a particular product. Therefore, the composite in its essence can not always be a priori better than the traditional material in everything. The main advantages of most of the known composites in the world are their following properties [1-9]:

• high mechanical strength (with a temporary resistance of up to 3500 MPa);

• high mechanical rigidity (with modulus of elasticity from 130 to 240 GPa);

- high corrosion resistance in corrosive environments and wear resistance of structures from CM;
  - high fatigue mechanical strength;
  - high heat and heat resistance (up to 1650 °C);
  - high thermal protection properties of CM;
  - low coefficient of thermal expansion;
  - low density and weight (mass) characteristics, which make the structures made with the use of CM easy;
  - possibility of manufacturing from CM dimension-stable structures for various purposes.

3.2. Some properties of boron plastics. One of the most promising CM in the field of aircraft and rocket construction are boron fiber, made with the use of reinforcing boron fiber and epoxy matrices [13]. According to the results of foreign studies, the use of boron plastics makes it possible to reduce the weight of the final design of an aircraft (20-40 %), significantly increase its rigidity and increase the operational reliability of the product as a whole [13]. The specific strength ratios of boron plastics and, for example, aluminum alloys for stretching are 1.3-1.9, for compression 1.5, for shear 1.2 and for crushing 2.2. In addition, the boron plastics retain their properties in the temperature range from -60 up to +177 °C [2, 13].

3.3. Some properties of carbon plastics. It is known that carbon plastics are characterized by a relatively low specific gravity (up to 1.5 g/cm^3 while the density of aluminum alloys is about 2.8 g/cm^3, and that of titanium alloys is 4.5 g/cm^3 [13]), high stiffness values, vibration and fatigue strength [1-9]. According to the data of [13], the mechanical strength and rigidity of carbon plastics is about six times higher than that of the main grades of steel used in aircraft designs. The carbon plastics are radio transparent (they pass electromagnetic waves well through themselves) [1-9]. Carbon fibers (carbon plastics) with a carbon matrix (with specific gravity up to 1.4 g/cm^3) have high heat-shielding properties and the ability to maintain their strength characteristics at temperatures up to 2500 °C [7, 13].

3.4. Some properties of boron aluminum. In this CM with a matrix of aluminum alloys, boron fibers (sometimes coated with silicon carbide SiC) are used as the reinforcing filler [13]. Boron aluminum is 3.5 times lighter than aluminum and twice as strong as aluminum, which makes it possible to obtain significant weight savings for a number of aircraft designs. In addition, at high temperatures (up to 430 °C), the boron aluminum composite has twice the values of mechanical strength and stiffness compared to titanium [13]. Therefore, boron aluminum can compete with titanium when used in supersonic aircraft with flight speeds of about three Mach numbers (at present, only titanium alloys are used as structural material in such aircraft) [13].

3.5. Disadvantages of composites. All CMs known to date in the world have a number of significant shortcomings that hinder their wider application in various areas of modern technology [1-9]:

- high cost, which is due to the high science-intensive production of CM, the need to use special expensive equipment and raw materials in the CM technology;
- anisotropy of properties, leading to the dependence of the physico-mechanical characteristics of CM from the choice of the direction of their measurement in the finished product;
- low impact strength, which determines the choice of an increased safety factor for the product, and as a result - increased consumption of expensive CM and an increased probability of concealed defects in the product;
- high specific volume of CM in the product, which is unacceptable in areas with a strict limitation of occupied volume (for example, when creating supersonic aircraft, for which even a slight increase in the volume of elements leads to a sharp increase in wave drag);
- hygroscopicity, caused by the incompleteness of the internal structure of CM and, accordingly, propensity to absorb atmospheric moisture;
- toxicity caused by the release of toxic fumes from the structure of CM during their long-term operation;
- low operational manufacturability leading to low repairability of composites and high cost of operation of products in the construction of parts of which CM is used.

4. The main applications of composites in engineering. Areas of use of CM are not limited. The introduction of composites into modern technology provides a new qualitative leap in increasing the power of engines, power plants and vehicles, reducing the weight (mass) of machines and devices. Practical application of CM in modern technology will be considered on a number of examples.

4.1. Aviation and rocket and space technology. CMs with a metal matrix, reinforced with filamentary single crystals («whiskers»), were created in the early 1970s purposefully for aviation and space structures of aircrafts [8]. Filamentary crystals for composites are prepared by pulling a suitable melt through spinnerets. For these technical purposes, the «whiskers» of sapphire (aluminum oxide Al_2O_3) and beryllium, boron and silicon carbides, as well as aluminum, silicon and other chemical elements of length (0.3-15) mm and diameter (1-30) μm are used [8, 11]. Reinforcement of the «whiskers» of many metals can significantly increase the strength of the material being created and increase its heat resistance. Thus, the yield stress of a composite composed of silver containing 24% «whiskers» of aluminum oxide is 30 times higher than the yield strength of silver and twice as many silver-based CMs [11]. The reinforcement of «whiskers» made of aluminum oxide composites based on refractory metals tungsten and molybdenum doubles their mechanical strength at a working medium temperature up to 1650 °C [11]. This made it possible to use these heat-resistant CMs with a metal matrix in the manufacture of heat-resistant nozzles for most liquid and solid-fuel rocket engines for peaceful and military launch vehicles.

The use of boron plastics in modern technology is limited, above all, by the high cost of producing boron fibers used in them (up to USD 400 / kg [8]). In this connection, they are used mainly in products of aviation and rocket and space technology in parts and assemblies subjected to long-term power loads under the influence of an aggressive medium [8]. Due to the qualities mentioned above (see paragraphs 2.4 and 3.3), carbon plastics are considered to be very promising for the manufacture of those parts and units of airplanes that operate at high temperatures, as well as for heat shields of aircrafts and, above all, spacecraft [13]. Note that initially (in the 1970s) the use of carbon plastics in aircraft designs was insignificant (due to the high cost of carbon fiber, up to USD 900 / kg) [13]. At the beginning of the 21st century, this cost was already about USD 150 / kg. According to the forecasts of American specialists, the cost of carbon fiber will soon be up to USD 80 / kg. Based on the information given in Section 3.4, boron aluminum can also be considered one of the promising CMs, the use of which in aircraft construction can give up to 50% of the weight savings of aircraft designs [11, 13].

Fig. 3 shows a general view of the Russian medium-haul passenger aircraft of the Tu-204 type, in the designs of parts (assemblies) of which at the beginning of the 21st century the share of CM was up to 25 % [14]. We will point out that the proportion of using composites on a new Russian aircraft of the MC-21 type, developed by the «Irkut» Corporation, will amount to as much as 37 %.

Fig. 3. The general view of a medium-haul passenger aircraft of the Tu-204 type (RF, 1990's) in which up to 25% of all parts of the glider were made of composites [14]

World leaders in aircraft construction – the corporations Airbus and Boeing are also actively using composites in the designs of their aircraft. If only (10-15) % of CM from the weight of the liner was used in their A-340 and B-777 aircraft in 2000, then in 2015 this figure was not less than 50 % [14]. Fig. 4 shows the general view of the American trunk passenger aircraft type Boeing 787 Dreamliner in which the share of CM by mass (weight) exceeds 50 % [14].

It is known that the use of polymer CM in the production of aviation and space technology can reduce from 5 to 50 % weight (mass) of aircraft [11, 13]. At the same time, it should be noted that the reduction in weight

(mass), for example, of an artificial Earth satellite when it is brought to a near-earth orbit by 1 kg leads to savings of money up to USD 1000 [11]. In this regard, the tasks of the practical application of CM in the objects of rocket and space technology are today not only relevant and promising, but as defining and strategic tasks for developers and creators of this high technology.

The general view of the main passenger aircraft of the type Boeing 787 Dreamliner (USA, 2015) the fuselage and wings of which were 90 % made of composites [14]

Using the world experience of using CM in civil and military aircraft designs and taking into account the high mechanical and thermal protection properties of polymer CM, US specialists came to the conclusion that carbon fiber composites with a carbon matrix are used in the manufacture of strategic missile warheads [13, 15].

It should be noted that a number of critical parts of artificial earth satellites (for example, the frames of their radio antenna series) are already made of carbon plastic in combination with an aluminum honeycomb structure [11, 15]. Let us emphasize that at the present time, due to the special importance and availability of many technological know-how for the production in the world of high-quality carbon fiber and, accordingly, the technology for making various carbon plastic materials with it, are closed «with seven locks». According to authoritative scientists, no more than two or three countries own such technologies in the world today [16]. You can not buy them by purchasing the appropriate licenses from the developer. Therefore, many interested firms, working especially in the field of aerospace engineering, face a dilemma: [16] «*Either you buy a finished product (for example, an aircraft in which carbon fiber is used in the form of parts). Either you need to develop the necessary technology for the production of good carbon fiber*».

Fig. 5 shows the general view of the orbital compartment of the new American spacecraft Liberty for transportation of astronauts and scientific equipment to the International Space Station (ISS) [17]. The light housing of the compartment was made of polymer CM based on carbon fiber [17].

We point out that at the Scientific-&-Research Planning-&-Design Institute «Molniya» of the NTU «KhPI» in recent years, in conjunction with the State Enterprise «Antonov», the I.N. Frantsevich Institute for Problems of Materials Science of the National Academy

of Sciences of Ukraine and Boeing Corporation, certification tests of prototype of sheet specimens with dimensions in the plan of 500×500 mm of a number of CMs intended for the manufacture of composite cladding of domestic and foreign passenger airplanes (including the Boeing 787 Dreamliner [14]), on the resistance to direct action of pulsed current of artificial lightning on them [18] were carried out.

Fig. 5. The general view of the orbital compartment of the new spaceship Liberty (USA) made on 90 % of polymer composites and intended for the re-delivery of astronauts and scientific cargoes on board the ISS [17]

These tests were performed on a unique generator of artificial lightning current type УИТОМ-1 developed and created at our Institute (at the Department No. 4 for Electromagnetic Investigations) which generates a pulsed A- and long-time C- components of the simulated thunderstorm air current at the tested technical facility with normalized amplitude-temporal parameters (ATPs) [19]. In addition, these high-current high-voltage tests were conducted in accordance with the stringent requirements of the current US regulations SAE ARP 5412 and SAE ARP 5416 [20, 21]. As a result of long-term tests (with a total number of tested at the working table of the generator УИТОМ-1 of different composition and identical by the geometric dimensions of experimental samples of sheet composites of not less than 250 pieces), stable CMs were determined to directly affect the specified normalized [21] the component of the pulsed current of artificial lightning with limiting ATPs (at amplitude I_{mA} of the pulsed A- component of the current of negative polarity with a front duration ≤50 μs equal to (200±20) kA, the action integral of the pulsed A- component (2±0.4)·10^6 J/Ω, the duration of the pulsed A- component of current ≤500 μs, the amplitude I_{mC} of the long C- component of negative polarity current equal to (0.2-0.8) kA, charge of a long C- current component equal

to (200±40) K, the duration of the flow of a long C- current component equal to (0.25-1) s [18]).

Fig. 6 shows the external view of the rounded damage zone (up to 100 mm in diameter) of the experimental sheet specimen of the 3 mm thick composite lining (with its dimensions in the plan of 500×500 mm) when it is exposed to only a pulsed A- component of the artificial lightning current with an amplitude equal to I_{mA}≈−212 kA [18]. The multilayered composite of this sample had in its composition layers of fiberglass with an epoxy matrix, layers of carbon fiber with an epoxy phenol matrix, and layers of thin metal meshes acting as a reinforcing agent [7, 18].

4.2. Mechanical engineering. In the machine building industry, CM is widely used to create hard coatings on the cutting tool and protective coatings on metal surfaces with intense friction, and also for the manufacture of various parts of internal combustion engines (e.g. pistons, connecting rods, etc.) [1-9, 22]. In this case, solid structures of titanium carbide TiC are used to create wear-resistant coatings on the cutting tool [22], and for a protective coating a number of functionally different materials can be used [2, 11]: inorganic materials (modified by various additives, magnesium, iron and aluminum silicates); polymeric materials (polytetrafluoroethylenes modified with ultradisperse diamond-graphite powders and ultrafine powders of soft metals); organometallic materials containing an increased number of acidic functional groups. Due to the formation of high-strength metal-ceramic, polytetrafluoroethylene and organometallic layers on the protected surfaces in the local zone of high power loads (due to phase transitions and plasticization processes), the protective composite coatings formed are characterized by the following properties [1-9]: high adhesion to the surface of the protected metal; high purity of the working surface (up to grade 9); low porosity (at pore sizes up to 3 μm and coating thickness up to 100 μm); low coefficient of friction (up to 0.01).
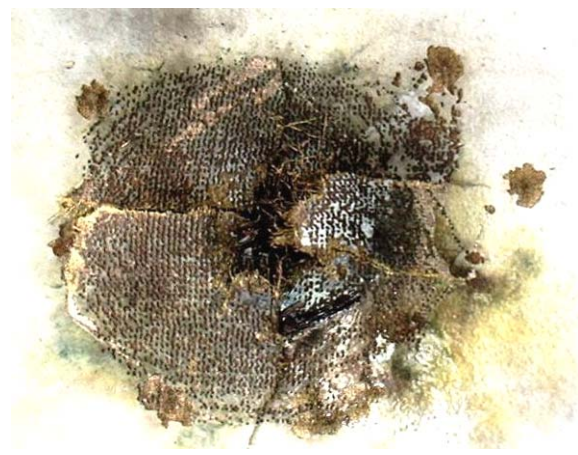

Fig. 6. The results of the action of an artificial lightning current pulse ($I_{mA} \approx -212$ kA) on a prototype aircraft skin made of multilayer CM using fiberglass, carbon fiber, and metal mesh [18]

4.3. Special fields of technology. From high-temperature cermets now make parts for jet aircraft and space technology, gas turbines, as well as various armature electric furnaces [11]. Solid wear-resistant cermets are used for the manufacture of cutting tools. In addition, cermets are used in special fields of engineering in the manufacture of fuel elements of atomic reactors based on natural uranium oxide $_{92}^{238}U$, friction materials for brake systems of various devices, etc. [11].

FGM can be effectively used in the following technical areas [12]: in military equipment (making bulletproof vests and protecting tanks and helicopters from bullet and fragmentation); for metalworking (making cutters for processing hard-to-work steels and alloys); in the mining industry (making cutters for rock drilling); in the processing industry (lining grinders for grinding solids), etc.

Dispersion-hardened composites based on sintered aluminum alloy SAP are used in the manufacture of blades of powerful compressors, fans and steam turbines [11]. CM containing reinforced filamentary single crystals have found application in the manufacture of gas turbine blades, which are made of nickel alloys reinforced with crystalline yarn of sapphire (aluminum oxide Al_2O_3) [7, 9]. This makes it possible to significantly increase the temperature of superheated steam at the inlet to the turbine (note that the ultimate strength of sapphire single crystals at a temperature of 1680 °C is not less than 700 MPa [11-17]) and, accordingly, to increase its efficiency.

Such composites known as from the middle of the 20th century as various types of textolites (in these CM as a filler, fabrics from various fibers - cotton, synthetic, glass, carbon, asbestos, basalt, etc.) and wood-laminated plastics based on phenol-formaldehyde resin have found application in high-voltage high-current electrical engineering in the manufacture of power units and load-bearing elements of insulating structures of powerful electrophysical installations for scientific and technological purposes [18].

Conclusions.

1. Metal and non-metallic composites, because of their high physical and mechanical characteristics, have already found wide practical application in many areas of modern technology (in aviation technology for highly loaded parts of aircraft and their engines, in space technology for power units of aircrafts subjected to intense heating and large overloads, elements of rigidity and thermal protection of aircraft, in the reactor building for nuclear power plants, in mechanical engineering for the creation of solid and protective coatings, etc.; before and in the automotive industry for the production of propellers and for the facilitation of bodies, frames, auto panels, etc., in turbine construction for the production of blades, in the chemical industry for autoclaves and tanks for storing and transporting chemical and petroleum products, in the mining industry in the manufacture of drilling tools, parts underground combines, etc., in civil engineering in the performance of spans of bridges, elements of prefabricated structures of high-rise structures, etc.; in high-voltage impulse technology for the manufacture of such reinforced insulation materials as fiberglass, wood-laminated plastic grade ДСПБ-Э, bakelite, bakelized plywood, etc.).

2. The complex scientific and technical task facing the producers of composites in the world is the development of new technologies for their manufacture with lower costs that would make the CM competitive with respect to traditional metals and alloys that are also involved in the struggle for a leading role in the production of future technology.

3. Composites can become for humanity a constructional material for the near future. It is these synthetic materials that successfully combine high mechanical strength with their high modulus of elasticity and low density.

REFERENCES
1. Available at: https://en.wikipedia.org/wiki/Composite_material (accessed 13 June 2015).
2. Available at: http://www.e-plastic.ru/main/articles/r2/pk01. (accessed 12 May 2016). (Rus).
3. Piatti J. *Dostizhenija v oblasti kompozicionnyh materialov* [Achievements in the field of composite materials]. Moscow, Metallurgy Publ., 1982. 304 p. (Rus).
4. Available at: http://www.mtomd.info/archives/1764 (accessed 03 March 2014). (Rus).
5. Vasil'ev V.V. *Mehanika konstrukcij iz kompozicionnyh materialov* [Mechanics of composite structures materials]. Moscow, Metallurgy Publ., 1988. 272 p. (Rus).
6. Available at: http://stroimsamolet.ru/057.php (accessed 21 October 2015). (Rus).
7. Available at: http://www.hccomposite.com/catalog/40/131 (accessed 10 May 2016). (Rus).
8. Available at: http://www.mtomd.info/archives/1764 (accessed 20 April 2015). (Rus).
9. Available at: http://www.zadachi.org.ru/?n=150240 (accessed 15 August 2014). (Rus).
10. Baranov M.I. An anthology of outstanding achievements in science and technology. Part 13: Nanotechnologies. *Electrical engineering & electromechanics*, 2013, no.2, pp. 3-13. (Rus). **doi: 10.20998/2074-272X.2013.2.01.**
11. Available at: http://www.krugosvet.ru/enc/nauka_i_tehnika/himiya/KOMPOZITSIONNIE_MATERIALI.html?page=0,0 (accessed 12 May 2015). (Rus).
12. Available at: http://dic.academic.ru/dic.nsf/ruwiki/367846 (accessed 02 January 2013). (Rus).
13. Available at: http://pentagonus.ru/publ/1976/kompozicionnye_materialy_v_aviastroenii_1976/126-1-0-1942 (accessed 01 May 2013). (Rus).
14. Available at: http://olymp.asclub.ru/publ/raboty_1_go_tura/gotovye_raboty/kak_i_gde_v_samoletostroenii_ispolzujutsja_kompozicion-nye_materialy/6-1-0-825 (accessed 21 September 2015). (Rus).
15. Available at: http://www.spblp.ru/ru/magazine/82/183 (accessed 11 November 2016). (Rus).

16. Available at: http://olgamwill.livejournal.com/5463.html (accessed 18 June 2015). (Rus).

17. Available at: http://rnd.cnews.ru/news/top/index_science.shtml?2012/05/12/489249 (accessed 22 April 2014). (Rus).

18. Baranov M.I. *Izbrannye voprosy elektrofiziki. Tom 2, Kn. 2: Teoriia elektrofizicheskikh effektov i zadach* [Selected topics of Electrophysics. Vol.2, Book 2. A theory of electrophysical effects and tasks]. Kharkiv, Tochka Publ., 2010. 407 p. (Rus).

19. Baranov M.I., Koliushko G.M., Kravchenko V.I., Nedzel'skii O.S., Dnyshchenko V.N. A Current Generator of the Artificial Lightning for Full-Scale Tests of Engineering Objects. *Instruments and Experimental Technique*, 2008, no.3, pp. 401-405. **doi: 10.1134/s0020441208030123**.

20. SAE ARP 5412: 2013. Aircraft Lightning Environment and Ralated Test Waveforms. SAE Aerospace. USA, 2013. − pp. 1-56.

21. SAE ARP 5416: 2013. Aircraft Lightning Test Methods. SAE Aerospace. USA, 2013. − pp. 1-145.

22. Vereshchaka A.S., Tret'yakov I.P. *Rezhushchie instrumenty s iznosostojkimi pokrytijami* [Tool pieces with wearproof coverages]. Moscow, Engineering Publ., 1986. 192 p. (Rus).

M.I. Baranov, Doctor of Technical Science, Chief Researcher,
Scientific-&-Research Planning-&-Design Institute «Molniya»
National Technical University «Kharkiv Polytechnic Institute»,
47, Shevchenko Str., Kharkiv, 61013, Ukraine,
phone +380 57 7076841,
e-mail: baranovmi@kpi.kharkov.ua

V. Pliugin, O. Petrenko, V. Grinina, O. Grinin, A. Yehorov

IMITATION MODEL OF A HIGH-SPEED INDUCTION MOTOR WITH FREQUENCY CONTROL

Purpose. To develop the imitation model of the frequency converter controlled high-speed induction motor with a squirrel-cage rotor in order to determine reasons causes electric motor vibrations and noises in starting modes. Methodology. We have applied the mathematical simulation of electromagnetic field in transient mode and imported obtained field model as an independent object in frequency converter circuit. We have correlated the simulated result with the experimental data obtained by means of the PID regulator factors. Results. We have made the simulation model of the high-speed induction motor with a squirrel-cage rotor speed control in AnsysRMxprt, Ansys Maxwell and Ansys Simplorer, approximated to their physical prototype. We have made models modifications allows to provide high-performance computing (HPC) in dedicated server and computer cluster to reduce the simulation time. We have obtained motor characteristics in starting and rated modes. This allows to make recommendations on determination of high-speed electric motor optimal deign, having minimum indexes of vibrations and noises. Originality. For the first time, we have carried out the integrated research of induction motor using simultaneously simulation models both in Ansys Maxwell (2D field model) and in Ansys Simplorer (transient circuit model) with the control low realization for the motor soft start. For the first time the correlation between stator and rotor slots, allows to obtain minimal vibrations and noises, was defined. Practical value. We have tested manufactured high-speed motor based on the performed calculation. The experimental studies have confirmed the adequacy of the model, which allows designing such motors for new high-speed construction, and upgrade the existing ones. References 15, tables 3, figures 15.
Key words: **induction motor, squirrel cage, high-speed, scalar control, ANSYS, RMxprt, Simplorer, high-performance computing, simulation, vibration, noise.**

Разработана имитационная модель высокоскоростного асинхронного двигателя с короткозамкнутым ротором при скалярном частотном управлении в программном пакете AnsysMaxwell&Simplorer. При моделировании на кластере высокопроизводительных расчетов выполнены параллельные вычисления полевой модели электродвигателя (AnsysMaxwell 2D) и модели, построенной на основе теории цепей (Ansys Simplorer), что позволило создать имитационные модели, приближенные к их физическим прототипам. Выполнен анализ пусковых характеристик, оптимизированы параметры электродвигателя. Даны рекомендации по выбору числа пазов статора и ротора высокоскоростного асинхронного двигателя, что позволило существенно уменьшить вибрации и шумы в режиме пуска. Библ. 15 табл. 3, рис. 15.
Ключевые слова: **асинхронный двигатель, короткозамкнутый ротор, высокоскоростной, скалярное управление, ANSYS, RMxprt, Simplorer, высокопроизводительные вычисления, моделирование, вибрация, шум.**

Introduction. High-Speed Induction Motors (HSIM) are induction motors working on high rotation speeds. At an instance HSIM, controlled from frequency converters (FC) with frequency 400 Hz, have rotation speeds up to 30000 rev/min.

In modern HSIM the increase of high speed is achieved without application of reducing gears and strap transmissions due to control from the FC. HSIM are well adjusted for a work in the weak field mode, providing the maximum wide speed range, restricted only by their mechanical construction.

At high rotation speed, there are considerable vibrations and noises both at starting and during a work in the rated mode. The high level of vibrations results in destruction of bearing in a short time, and the level of noises rising to a critical level. That is why a task of vibrations and noises diminishing in HSIM is actual for modern industrial enterprises and producers of electric engineering industry. To solve this task Ansys Maxwell & Simplorer software both for induction motor design and transient simulation were used [1, 2].

There are limited amount of works devoted to speed control of induction motor in Ansys Maxwell & Simplorer software [3, 4]. In addition, existent works are not spared attention to forming of motor smooth starting mode and features for frequency control laws realization [5, 6].

In many of publications we can find only information of motor control theory or with coupling of Ansys software with Matlab/Simulink but without detail description of control system realization [3, 7, 8]. In known software products that allow the implementation of frequency control, the mathematical models are based on differential equations [9, 10].

A distinctive feature of the Ansys software is the ability to connect the simulation model of the control system (Ansys Simplorer) to the object of the electric machine, storing the full field data (AnsysMaxwell 2D & 3D), including the state of the electromagnetic field values (magnetic induction vector with vector magnetic potential for 2D calculations and vector magnetic induction with a vector of magnetic field strength for problems in 3D formulation) in a given range of rotation frequencies. Thus, the jointly solved field problem and the mathematical model of frequency control increase the accuracy of calculations due to the operation of electromagnetic field components in space and time. The amount of data operated by the Ansys program, reaches 20-30 GB, which requires huge computing resources. Setting up a cluster of high-performance calculations (HPC), implemented by the authors using parallel computing technology, solved the problem of increasing the processing speed of a large data set.

Works devoted to the implementation of the described task are not elucidated in the technical literature or partially disclosed.

In this paper the material on the induction motor with a squirrel-cage rotor field model scalar control in

Ansys Maxwell and Ansys Simplorer with a detailed study of the simulation model is given for the first time.

Imitation modeling of the HSIM transient processes, considered in this work, allows to estimate their characteristics without making a full-scale sample, which significantly reduces the price of electric machines development and choosing their optimal parameters.

The aim of the paper is development and investigation of induction motor simulation model, controlled from the frequency converter with the using of parallel modeling on HPC cluster.

Simulation of an asynchronous drive in Ansys Maxwell. Now for the electric machines design and simulation the most used programs are Matlab/Simulink, SciLab, wxMaxima, Mathcad, Comsol Multiphysics. The advantage of Ansys Maxwell and Simulink package, compared to the known programs is an imitation of transients on mathematical models, near to their physical prototypes. Mainly it is realized due to objective approach in implementation of electric machines. The Ansys package includes three software products specialized in design and simulation of electric machines and electric drive systems: RMxprt, Maxwell 2D/3D and Simplorer [1]. It is possible to simulate electric drive with the motor, calculated previously in RMxprt (engineering project) or Maxwell 2D/3D (electromagnetic field project) [4]. The motor of RMxprt or Maxwell 2D/3D project is inserted as an object to the Simplorer shield and calculated simultaneously. The program RMxprt allows to make engineering calculation of electric machines based on the circuit of theory. On Fig. 1 the RMxprt model of an induction motor is shown.
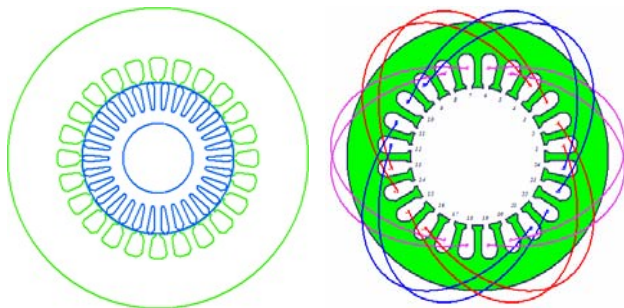

Fig. 1. Induction Motor with Squirrel Cage Rotor Model
in Ansys RMxprt

Model, calculated in RMxprt, can be exported in Maxwell 2D/3D project for the solving the field task. The exported model is formed the task of transient simulation fully adjusted for solving, including setting of materials properties, border and symmetry conditions, winding excitation and electric circuit diagram, selection of moving object with inertia torque and motion function. Templates of charts and output data shield are created too. A model of induction motor example, automatically generated in Maxwell 2D on Fig. 2 is shown.

As a result of laboratory tests of induction motors E&A of Swiss production (four-pole, 1010 Hz) and Ukrainian – series DAV (two-pole, 505 Hz), the presence of vibrations during the start-up and operation of the DAV motor was detected.

We have made numerous calculations of electromagnetic field of these motors in transient mode in

Ansys Maxwell 2D in order to find reasons that cause vibrations. Ansys offer a direct integration with a number of HPC software programs and provide parallel processing for running advanced application programs efficiently, reliably and quickly. We can enable queuing, set the design type, specify the distributed memory vendor and enable GPU for transient solves.
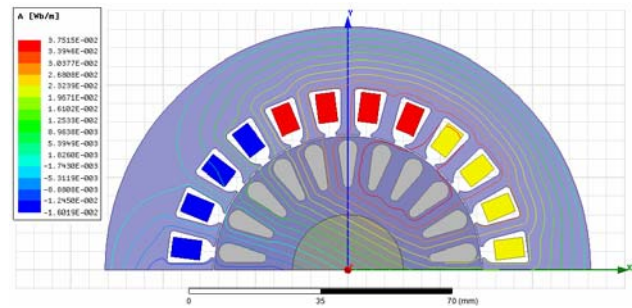
Fig. 2. Induction Motor with Squirrel Cage Rotor Model
in Ansys Maxwell 2D

All results in Ansys Maxwell&Simplorer shown in this paper, were got in HPC cluster with ten 2-core (with hyper-threading technology) processors Intel Core i3 2.40 GHz; 48 Gb of server RAM; 64x OS Microsoft Windows HPC Server 2008 R2 SP2 and dedicated server (4 cores, 8 Gb RAM). Using of this cluster allow us to provide a way to solve complex problems in a short amount of time. Some of simulation results of motors with different ratio Z_s/Z_r, and rotor slots shapes in Table 1 are shown.

As calculations have shown, the presence of vibrations is caused by reversing brake torques that arise with a certain combination of stator Z_s and rotor Z_r slots.

All motors, that have braking torque at start mode and have high level of vibrations and noises, represented by Torque-Time chart, shown on Fig. 3. On this picture the mechanical torque, registered in experiment and equal to 4.5 Nm, is shown with a dotted line. The simulation torque, equal to 5.2 Nm, is represented by a solid curve.

All motors with positive torque at start mode and without vibrations, represented by Torque-Time chart, shown on Fig.4. On this picture the mechanical torque, registered in experiment and equal to 1.2 Nm, is shown with a dotted line. The simulation torque, equal to 1.35 Nm, is represented by a solid curve.

As we can see from Table 1, the shape and material of rotor slots does not have any influence on the braking torques presence and the level of vibrations and noises.

Analysis of got results have shown that in order to eliminate magnetic vibrations, the following correlations must be performed

$$Z_2 = 2pmg \pm 2p,$$
$$Z_2 = Z_1 + 2p,$$
(1)

where g – integer, «+» is for motor mode and «–» is for generator mode.

It is need to know, that equations (1) are true only for high-speed motors with net frequency more than 200 Hz. For motors with net frequency 50-60 Hz following the equations (1) will cause synchronous braking torques from high harmonics.

Braking torques in high-speed motors with different ration of stator and rotor slots

No.	Z_s / Z_r poles	Rotor slot shape and material	Presence of braking torque
1	24/22 2p = 2	Al	Yes
2	24/28 2p = 4	Al	No
3	24/26 2p = 2	Al	No
4	24/26 2p = 2	Al	No
5	24/22 2p = 2	Al	Yes
6	24/28 2p = 4	Al	No
7	24/22 2p = 4	Al	Yes
8	24/22 2p = 2	Al	Yes
9	24/26 2p = 2	Al	No
10	24/22 2p = 2	Cu	Yes
11	24/26 2p = 2	Cu	No
12	24/22 2p = 2	Cu	Yes

High-speed induction motor simulation model. Both in RMxprt project and in Maxwell 2D/3D project, solved model can be exported as an object and becomes accessible by reference in Simplorer working shield. In Simplorer a complete electric supply and control system, including electric motors, different scopes and signals distribution are fully supported.

The design of transients in HSIM is impossible without the imitation of control system, built on the base of frequency converter. High-speed motors can be started during 5-10 min for the approaching of rated speed. For realization the law U/f = const frequency and voltage signals will be linearly rising from 0 to the rated values in starting time (t_{st}) and in relative units (f^*, u^*) will be coincide [11]:

$$f^* = u^* = \begin{cases} k_{st}t, & if \ 0 < t \le t_{st} \\ 1, & if \ t > t_{st} \end{cases}, \qquad (2)$$

where k_{st} – the rate of tempo increase, $k_{st} = 1/t_{st}$.
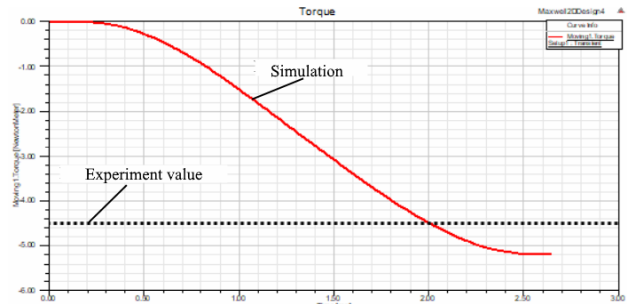
Fig. 3. Transient report of Maxwell 2D simulation for motor with vibrations
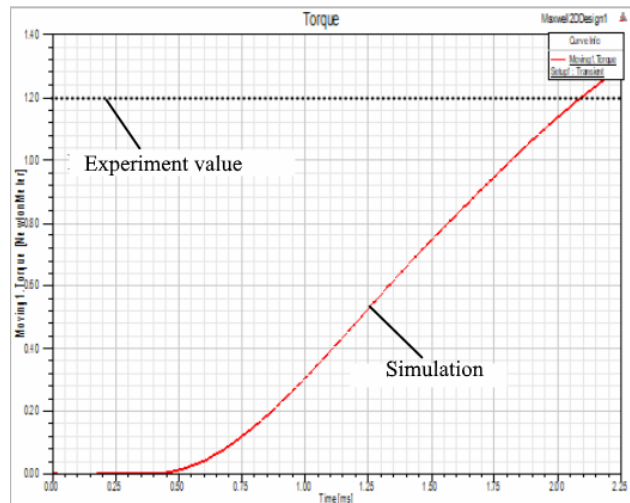
Fig. 4. Transient report of Maxwell 2D simulation for motor without vibrations

For the acceleration of motor starting processes, magnetizing first of all, voltage initial value u^* must be greater than zero. In this case a voltage change law will be the next [11]:

$$u^* = \begin{cases} u_0^* + \left(1 - u_0^*\right)k_{st}t, & if \ 0 < t \le t_{st} \\ 1, & if \ t > t_{st} \end{cases}, \qquad (3)$$

where u^*_0 – voltage relative value, $u^*_0 = u^*(0)$.

On Fig. 5 voltage and frequency signals realization in Simplorer design sheet are shown.

Below is decryption of blocks on Fig. 5:
• both STEP6 and INTEGRAL blocks forms time function (STEP6 block has Time Step value 0, Final Value 1 and Initial Value 1);
• GAIN6 block scales time value to starting time $1/t_p$;
• LIMIT1 block limits a signal at the level ±1;
• CONST5 block sets the boost voltage value (in relative units);
• GAIN block with the label U calculates $1 - u_0$ value by equation (3);

- GAIN block with the label *Uf* has value 1 and finalizes the equation (3);
- GAIN block with the label *f* has a rated frequency value and calculates actual frequency value in Hz;
- GAIN block with the label *speed* converts speed frequency value from Hz to rad/s and has value 60/*p*;
- Data block ICA sets the model constant parameters values.
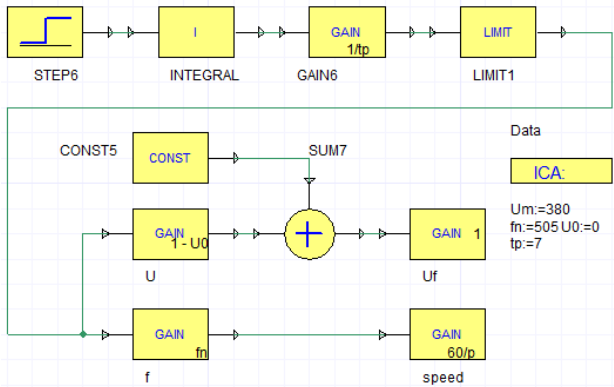
Fig. 5. *U/f* control signals realization in Simplorer

AC voltage source in Simplorer forming the output electric voltage with given function. If we set the frequency signal on AC voltage input port, we will get an error result. Instead of the expected voltage equation $U = U_m \cdot \sin(\omega t + \varphi_0)$ we will obtain $U = U_m \cdot \sin(\omega(t)t + \varphi_0)$ where we have a variable angular speed function $\omega(t)$ under the sinus instead of constant value ω. If frequency is linearly growing, the motor speed will be double from the rated value. To obtain the correct frequency signal, it is necessary to change the form of AC voltage Sourceblock in property Simplorer from harmonic time controlled function to EMF value. Also it is need to take an integral from variable speed function to get the correct angle value $\delta = \int \omega(t) dt$ as on Fig. 6 is shown.
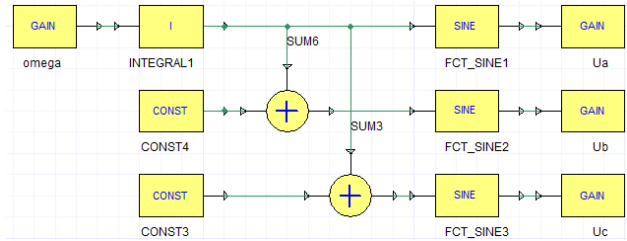
Fig. 6. AC Voltage Source signals block diagram in Simplorer

Below is decryption ofblocks on Fig. 6:
- GAIN block with the label *omega* has the value 2π and calculates angular speed;
- CONST4 block has the value $-2\pi/3$ and give time shift value for phase B;
- CONST3 block has the value $2\pi/3$ and give time shift value for phase C;
- GAIN blocks with the labels *Ua*, *Ub* and *Uc* with the same value U_f converts voltage value from relative to real (V) units;
- SINE block is standard sinus function.

The full block diagram of induction motor scalar control in Simplorer on Fig. 7 is shown. The induction motor model in presented block diagram is an imported object from RMxprt project.
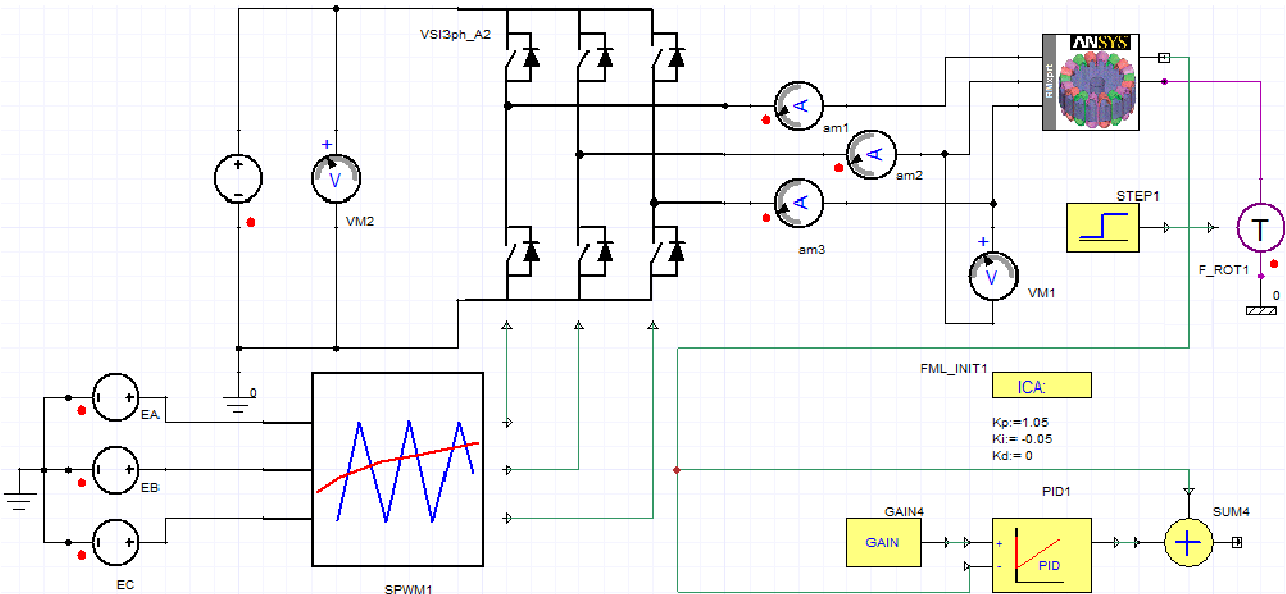
Fig. 7. High-speed induction motor main block diagram in Ansys Simplorer

Description of structure scheme shown on Fig. 7:
- *EA*, *EB* and *EC* blocks is AC Voltage source blocks and takes values from *Ua*, *Ub* and *Uc* GAIN blocks respectively;
- SPWM1 is sinusoidal PWM block;
- DC Voltage source block has the value $U_m\sqrt{2}$;
- VSI3phA2 block is Voltage Source Inverter;

- GAIN4 block converts the motor speed from rev/min to rad/s and has a value $2\pi/p$;
- PID controller block takes parameter values from ICA block;
- summation block SUM4 sends the output speed value to the GAIN block with the label *omega* (Fig. 8);
- F_ROT1 and STEP1 blocks realizes the mechanical torque value on motor shaft.

Simulation results. Before the transient simulation an induction motor in authors' design Java program [12, 13], Ansys RMxprt [14] and Ansys 2D [15] was developed. As induction motor a high-speed motor «DAV-22» of Ukraine production was taken.

The housing-less bipolar induction motor with a rated power 20 kW, line voltage 380 V and frequency 505 Hz has a built-in version and serves for driving a high-speed turbine.

The test bench was located in a vibro-acoustic chamber. At the stand, the electric motor was tested in idle mode, locked rotor motor and was connected to the Altivar (Schneider Electric production) frequency converter. The start of the electric motor was carried out according to the soft start program set in the frequency converter with a discrete frequency adjustment from 10 Hz to 505 Hz. Boost voltage was set to 50 V value.

During the tests, the currents in the motor phases, the three phases voltage of the motor and the frequency converter, frequency converter output frequency, the rotation speed, the noise and vibration levels, the temperature of the stator windings, as well as the moving torque value were registered. Summary data of the experiment and modeling results in Table 2 is given.

Fig. 8. Diagram of calculation and experiment results: rated current (I) and moving speed (n)

Fig. 9. Diagram of calculation and experiment results: starting current (Is) and torque (Ms) ratio, braking (Mb) and rated (M) torques

Table 2

High-speed induction motor data

Parameter Name	Parameter Value		
	Model	Experiment	Deviation, %
Rated current, A	36.45	39.05	6.66
Efficiency, %	91.25	90.10	1.28
Moving speed, rev/min	30064	29994	0.23
Starting current ratio	6.84	6.2	10.33
Starting torque ratio	0.69	0.61	13.11
Braking torque ratio	3.01	2.6	15.77
Copper losses, W	378	361	4.71
Rotor losses, W	221	190	16.32
Steel looses	404	400.1	0.97
Rated torque, Nm	6.35	6.37	0.31

Fig. 10. Diagram of calculation and experiment results: copper (Pcu), rotor (Pr) and steel (Ps) losses and efficiency

Comparative diagrams of the calculated parameters and parameters obtained as a result of experimental studies on Fig. 8-10 are shown. The symbol «M» on the diagram columns denotes the columns relating to the modeling, and the symbol «E» – to the experiment.

Analyzing the obtained results, the estimation error can be divided on three categories: energy, mechanical and power losses. In the energy category, which includes currents in the stator windings, efficiency and the starting current ratio, the highest convergence has the efficiency (deviation 1.28 %) and the smallest one – the starting current ratio (10.33 %).In the mechanical category (moving torques and speed), the minimum deviation of the calculated data from the experimental ones is the rated speed (0.23 %) and the rated torque (0.31 %), and the maximum – the braking torque (15.77 %).

In the losses category the most accurately calculated is steel loss (deviation 0.97 %), and the greatest error in the determination are losses in the rotor (16.32 %). The average error based on the results of calculation and experiment is 6.97 %.

The high discrepancies between the calculated values of the results obtained as a result of the full-scale experiment are due to the simplifications of the mathematical model (the field in the zone of the frontal parts was not calculated, the cross-section of the machine in the field calculation was considered without taking into account the slot skew, the properties of the steel were determined by main magnetization curve without splitting it into the tooth and yoke zones, did not take into account the presence of bearing shields).

Meanwhile, integral parameters, such as efficiency, current, rated torque, important for the evaluation of the model, have high convergence, which indicates the acceptability of the obtained results for engineering calculations.

In addition, the 100 % convergence of mathematical modeling is the fact of confirmation or absence of increased vibrations with different combinations of the number of stator and rotor slots.

After Ansys Maxwell & RMxprt calculation, the motor object with the full base of field calculations was imported in Ansys Simplorer. In simulation, as well as in real experiment, the soft start time value was 4s and total

simulation time was 6s. The speed vs time graph on Fig. 11 is shown. Dash lines represented the given speed and the solid one — actual motor speed in rev/min.
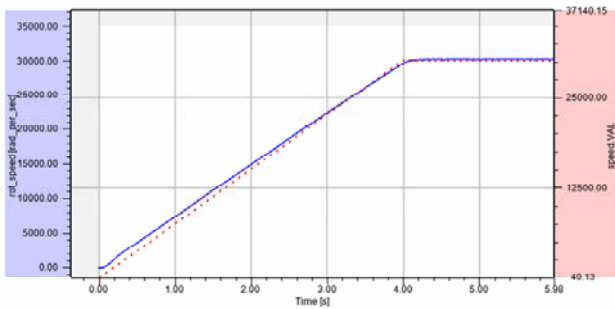
Fig. 11. Motor moving speed, rev/min vs time

Motor currents on Fig. 12 are shown. The dashed line (bottom graph, scaling by the time axis for steady state) indicates the value of the motor current obtained during the experimental studies.
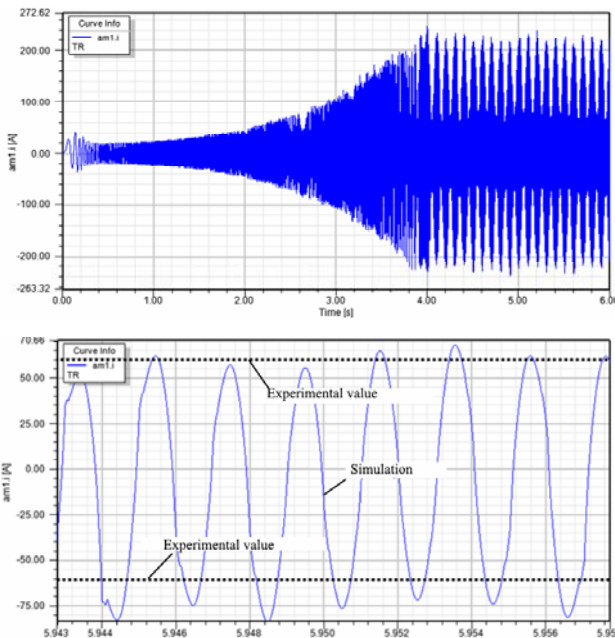
Fig. 12. Motor phase currents vs time

The graph of the one phase line voltage on Fig. 13 is shown.

The characteristic of the motor torque for a mode with vibrations on Fig. 14 is shown (scaled section on the time axis). The dashed line indicates the torque magnitude registered in experiment. This value also has good convergence with the torque magnitude, obtained during field calculations (Fig. 3).
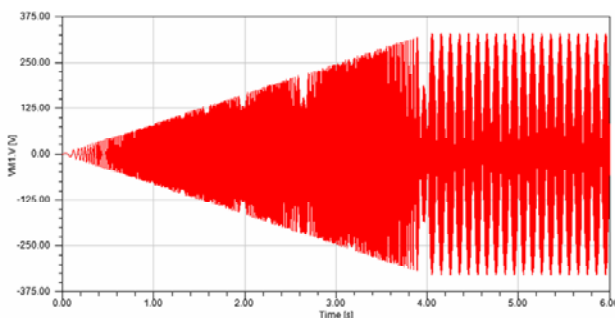
Fig. 13. Motor one phase voltage vs time
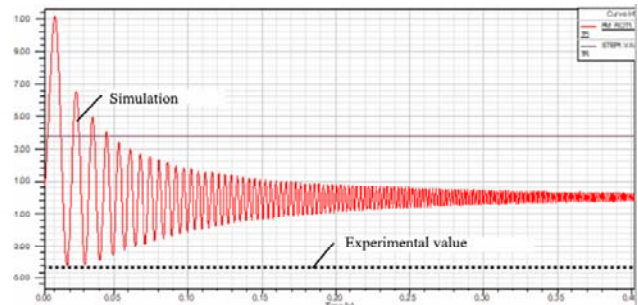
Fig. 14. Motor torque chart (full time range) with brake values

The characteristics of the motor torque for the mode without vibration on Fig. 15 is shown (scaled section on the time axis). The dashed line indicates the torque magnitude registered in experiment. This value also has good convergence with the torque magnitude, obtained in field calculations (Fig. 4).
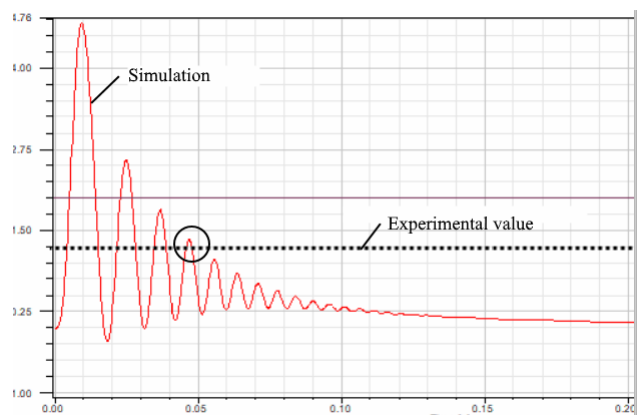
Fig. 15. Motor torque chart (scaled time range) without brake values

Comparative characteristics of the modeling results and experimental studies in Table 3 is given.

As follows from the given research results, the dependences of speed and voltage correspond to the task of equations (2) – (3) and accurately represent the set values of the control system.

Table 3

Results of imitation modeling and experiment

Parameter Name	Model	Experiment	Deviation,%
Rated current, A	39.1	39.05	0.13
Rated speed, rev/min	30064	29994	0.23
Negative starting torque value, Nm	–4.8	–4.5	6.67
Positive starting torque value, Nm	1.3	1.2	8.33

The results of the simulation were compared with actual factory experiments and have a good correlation (minimum deviation 0.13 %, maximum 8.33 %, average error 3.84 %) with experimental data from a certified factory laboratory.

Conclusions.

1. The simulation model of a high-speed induction motor with scalar frequency control in Ansys & Simplorer has been developed and investigated using parallel modeling on a cluster of high-performance computations, which makes it possible to create simulation models that are close to their physical prototypes. The results of the

simulation have good convergence with the results of experimental studies (deviation is not more than 8.33 %).

2. Using the simulation model, the correlation between the number of stator and rotor slots and the number of pole pairs of a high-speed induction motor with a rated frequency above 200 Hz is obtained for the first time and can significantly reduce vibration and noise in the motor start-up mode.

3. The developed simulation model of a high-speed induction motor allows to optimize its characteristics without using expensive actual tests and can be widely used both in the development of induction motors and in the educational process.

REFERENCES

1. Ansys Maxwell 2D v.15 – Electromagnetic and Electromechanical Analysis: users guide. Ansys, Inc., Pittsburgh, release 15.0, 2012. 628 p.
2. Ansys Maxwell 3D v.15 – Electromagnetic and Electromechanical Analysis: users guide. Ansys, Inc., Pittsburgh, release 15.0, 2012. 1006 p.
3. Electric machines considering power electronics. Ansys, Inc., Pittsburgh, 2012, 58 p.
4. The design of electric machines using Maxwell and Simplorer. Ansys, Inc., 2013. 48 p.
5. Zhao X., Liu H., Zhang J., Zhang H. Simulation of field oriented control in induction motor drive system. *TELKOMNIKA Indonesian Journal of Electrical Engineering*, 2013, vol.11, no.12, pp. 7555-7563. **doi: 10.11591/telkomnika.v11i12.3674.**
6. Behera P.K., Behera M.K., Sahoo A.K. Speed control of induction motor using scalar control technique. *International Journal of Computer Applications*, 2014, no.1, pp. 37-39.
7. Apostoaia C.M. Co-simulation platform for AC drives control systems. *Proc. WASET International Conference on Electric Machines and Drive Systems (ICEMDS '2012)*, Paris, France, Nov. 2012, pp. 1879-1886.
8. Ramesh K., Kumar C.R., Murali P.B. Modeling and implementation of vector control for induction motor drive. *International Journal of Computer Applications*, 2015, vol.3, no.2, pp. 80-91.
9. 32-BIT Microcontroller 3-Phase ACIM Scalar Control Application Note. Spansion, Inc., revision 1.0, 2015. 22 p.
10. Scalar (V/f) Control of 3-Phase Induction Motors. Texas Instruments, Inc., sPRABQ8, 2013. 25 p.
11. Zelenov A.B. *Teorijaj elektroprivoda* [Electric drive theory]. Alchevsk, 2005. 508 p. (Rus).
12. Zablodskii N.N., Pliugin V.E., Petrenko A.N. Using of object-oriented design principles in electric machines development. *Electrical Engineering & Electromechanics*, 2016, no.1, pp. 17-20. **doi: 10.20998/2074-272X.2016.1.03.**
13. Zablodskij N., Pliugin V., Fligl S., Lettl J. Dynamic simulation of the double-stator induction electromechanical converter with ferromagnetic rotor. *4th International Conference on Power Engineering, Energy and Electrical Drives*, Istanbul, Turkey, May 2013, pp. 1448-1453. **doi: 10.1109/powereng.2013.6635828.**
14. Zablodskii N.N., Plyugin V.E., Gritsyuk V.Y., Grin' G.M. Polyfunctional electromechanical energy transformers for technological purposes. *Russian Electrical Engineering*, 2016, vol.87, no.3, pp. 140-144. **doi: 10.3103/s1068371216030123.**
15. Zablodskiy N., Pliugin V. 3D magnetic filed distribution in a screw double-stator induction motor. *2015 16th International Conference on Computational Problems of Electrical Engineering (CPEE)*, Lviv, Ukraine, Sep. 2015, pp. 239-241. **doi: 10.1109/cpee.2015.7333386.**

V. Pliugin[1]*, Doctor of Technical Sciences, Professor,*
O. Petrenko[1]*, Candidate of Technical Sciences, Associate Professor,*
V. Grinina[1]*, PhD Student,*
O. Grinin[1]*, Engineer,*
A. Yehorov[2]*, Candidate of Technical Sciences, Associate Professor,*
[1] O.M. Beketov National University of Urban Economy in Kharkiv,
17, Marshal Bazhanov Str., Kharkiv, 61002, Ukraine,
e-mail: vlad.plyugin@gmail.com
[2] National Technical University «Kharkiv Polytechnic Institute»,
2, Kyrpychova Str., Kharkiv, 61002, Ukraine.

V.F. Bolyukh, A.I. Kocherga, I.S. Schukin

INFLUENCE OF ARMATURE PARAMETERS OF A LINEAR PULSE ELECTROMECHANICAL CONVERTER ON ITS EFFICIENCY

Purpose. The evaluation of the effect of armature parameters on the efficiency of a linear pulsed electromechanical converter, taking into account the power, speed, constructive and environmental parameters. Methodology. First, the height of the electrically conductive, coil and ferromagnetic armature of a linear pulse electromechanical converter is determined, at which the highest velocity develops. An integral efficiency index is introduced, which takes into account, in a relative way, the power, speed, energy, electrical and field characteristics of the converter. Variants of the efficiency evaluation strategy are used that take into account the priority of each indicator of a linear pulse electromechanical converter using the appropriate weighting factor in the integral efficiency index. Results. A mathematical model of a linear pulsed electromechanical converter is developed. It is established that as the height of the electroconductive, coil and ferromagnetic armature increases, the force pulse increases. The greatest speed develops with the use of a coil armature, and the smallest with an electroconductive armature. In the converter with coil and ferromagnetic armature, practically the same values of the electrodynamic and electromagnetic force pulse are realized, while in the converter the electrodynamic force is 1.52 times smaller in the converter by the electrically conductive armature. It is established that with all efficiency evaluation strategies, the converter with a coil armature is the most effective, even in spite of its constructive complexity, and the converter with a ferromagnetic armature is the least effective, although it is constructively the simplest. Originality. For the first time, using the integral efficiency index, which takes into account the power, speed, energy, electrical and field indices in a relative way, it is established that with all efficiency evaluation strategies, the converter with a coil armature is the most effective, and the converter with a ferromagnetic anchor is the least effective. Practical value. The height of the electrically conductive, coil and ferromagnetic armature of a linear pulse electromechanical converter is determined, at which the highest speed develops. It is shown that when using an electrically conductive armature, the value of the electrodynamic force pulse is lower than when using a coil and ferromagnetic armature. It is established that the converter with a coil armature is the most efficient, and the converter with a ferromagnetic armature is the least effective. References 11, tables 3, figures 2.
Key words: **linear pulse electromechanical converter, mathematical model, electrically conductive, coil and ferromagnetic armature, integral efficiency index, efficiency evaluation strategy.**

Разработана математическая модель линейного импульсного электромеханического преобразователя (ЛИЭП), описывающая быстропротекающие и взаимосвязанные электромагнитные и электромеханические процессы, проявляющиеся при перемещении якоря относительно индуктора. Показано, что при увеличении высоты электропроводящего, катушечного и ферромагнитного якорей ЛИЭП происходит увеличение импульса силы. Наибольшая скорость развивается в ЛИЭП с катушечным якорем, а наименьшая – в ЛИЭП с электропроводящим якорем. В ЛИЭП с катушечным и ферромагнитным якорями реализуются практически одинаковые значения импульса электродинамической и электромагнитной силы, а в ЛИЭП с электропроводящим якорем импульс электродинамической силы в 1,52 раза меньше. Введен интегральный показатель эффективности, который в относительном виде учитывает силовые, скоростные, энергетические, электрические и полевые показатели. Установлено, что при всех стратегиях оценки эффективности наиболее эффективным является ЛИЭП с катушечным якорем, а наименее эффективным является ЛИЭП с ферромагнитным якорем. Библ. 11, табл. 3, рис. 2.
Ключевые слова: **линейный импульсный электромеханический преобразователь, математическая модель, электропроводящий, катушечный и ферромагнитный якоря, интегральный показатель эффективности, стратегия оценки эффективности.**

Introduction. One of the promising devices of modern electromechanics are linear pulse electromechanical converters (LPEC) which provide a high speed of the actuator element (AE) on a short active site, and/or create powerful power pulses with little movement. LPEC are used in many branches of science and technology as electromechanical accelerators and shock-power devices [1-4].

In construction, electromagnetic hammers and perforators, devices for driving piles and anchors are used; in the mining industry – butchers, rock separators, vibrators; in geological prospecting – vibroseismic sources; in mechanical engineering – drives of mills of cold rolling of pipes, presses, hammers with a large range of impact energy; in the chemical and medical-biological industry – vibromixers and batchers. LPEC are used in magnetic pulse devices for pressing ceramics powders,

cleaning containers from sticking loose materials, destroying information on digital media, etc. Such converters are used in fast-acting valve and switching devices, in testing complexes for testing response products to shock loads, in aviation and space technology, in research facilities, for example, to study micro-meteorological impacts on space or responsible ground facilities. The problem of providing high speed for high-speed electrical apparatus is topical.

A feature of considered LPECs is that they operate with a short working cycle and a shock load that multiple exceeds the load of traditional linear motors of continuous action. LPEC of induction, electrodynamic and electromagnetic types the most widely used [5]. In these converters there is an electromagnetic interaction of the movable armature with a stationary inductor excited from

a pulsed source, usually a capacitive energy storage (CES). In these types of LPEC, the main difference is in the design of a movable armature, which ensures the acceleration of AE.

In the inductive-type LPEC, the electrically conducting armature (EA) is a relatively thin copper disk in which eddy currents are induced from the inductor, so that an electrodynamic repulsive force occurs between them.

In the LPEC of the electrodynamic type, the coil armature (CA) is a movable coil that is electrically connected to the inductor, i.e. it is fed by the same current, so that an electrodynamic repulsive force also occurs between them.

In the electromagnetic-type LPEC the ferromagnetic armature (FA) is a relatively thick-walled disk on which the electromagnetic force of attraction from the inductor side acts. Considering the considerable flux density of magnetic fields, it is advisable to use an external ferromagnetic shield (FS) with low electrical conductivity in the LPEC made either from a magnetodielectric or with radial cuts [6]. This shield increases the magnetic fields in the active zone of the LPEC and reduces the magnetic scattering fields which is important for closely located electronic devices and maintenance personnel.

LIEP with the types of armature under consideration provide different power and speed indicators creating different values of the flux density of magnetic scattering fields into the surrounding space. LPECs have a different mass of active elements, a constructive complexity that determines their reliability and the value of the excitation current of the inductor which is important for the electronic control system. As a consequence, for a well-founded choice of the type of LPEC armature, it is necessary to take into account many different disparate indicators.

The task of choosing the armature type for LPEC is actual. Thus, in [2], a comparative analysis of the LPEC with EA and CA is considered, and in [7] - LPEC with EA and with FA. In these works only electromechanical characteristics of the LPEC are considered, without considering the reliability of the design of the armature, the magnetic scattering fields, the interconnected electric, force, speed and mobile armature parameters and the presence of external FS.

Based on this, efficiency of the LPEC it is necessary to estimate the efficiency of the LPEC using an integrated indicator that takes into account its force, speed, power and electrical parameters, as well as the reliability of the armature design and the magnetic scattering field that negatively affects close-lying electronic devices and maintenance personnel. However, such studies have not been carried out so far, which makes it difficult to implement a reasonable and comprehensive selection of the electrically conductive, ferromagnetic or coil armature for LPEC.

The goal of the paper is the estimation of the influence of the parameters of the LPEC armature on its efficiency when taking into account the force, speed, constructive and environmental indicators.

Mathematical model. In LPEC under excitation from CES, fast interconnected electromagnetic and electromechanical processes occur when the armature moves relative to the inductor. Implementation of the mathematical model of LPEC using the theory of electric circuits does not allow to fully describe the totality of spatio-temporal processes [8]. Proceeding from this, the mathematical model of LPEC is used which is based on the finite element method.

Since these LPECs have axial symmetry, it is advisable to use a 2D mathematical model with spatially-distributed parameters [3]. To determine the electromagnetic parameters of the LPEC in the cylindrical coordinate system $\{r, z\}$, the magnetic vector potential A is calculated from the equation:

$$\frac{\partial}{\partial r}\left(\frac{1}{r\mu(B)}\frac{\partial(rA)}{\partial r}\right) + \frac{\partial}{\partial z}\left(\frac{1}{\mu(B)}\frac{\partial A}{\partial z}\right) + \sigma\frac{\partial A}{\partial t} = j_n , \quad (1)$$

where $\mu(B)$ is the magnetic permeability depending on the magnetic flux density B of the ferromagnetic material; σ is the electrical conductivity of the armature and the inductor; j_n is the current density in the active element; $n = 1$ is the index of the inductor; $n = 2$ is the index of the coil armature.

Components of the magnetic flux density vector are calculated by using known relations:

$$B_z = \frac{1}{r}\frac{\partial(rA)}{\partial r}; \ B_r = -\frac{\partial A}{\partial z} . \quad (2)$$

As boundary conditions the relation $n \times A = 0$ is used, where n is the unit vector of the outer normal to the surface. For the ferromagnetic materials the nonlinear magnetization curve $B = f(H)$ is used.

The current in the inductor i_1 is described by the equation:

$$(R_e + R_1)\cdot i_1 + L_e\frac{di_1}{dt} + \frac{1}{C}\int i_1 dt + \frac{N_1}{s}\int_V \frac{dA_l}{dt}dv = 0;$$

$$\frac{1}{C}\int_0^t i_1 \cdot dt = U_0, \quad (3)$$

where R_e is the active resistance of the external circuit; R_1 is the active resistance of the inductor; L_e is the inductance of the external circuit; U_0 is the CES charging voltage; C is the CES capacitance; N_1 is the number of turns of the inductor; s is the of the cross-section of the inductor permeated by the magnetic flux; A_l is the projection of the magnetic vector potential on the direction of traversal of the contour; V is the volume of the inductor.

The electrodynamic or electromagnetic forces acting on the armature are found using the Maxwell tension tensor:

$$f_z = 0.5\oint_S [H(B\cdot n) + B(H\cdot n) - n(H\cdot B)]ds , \quad (4)$$

where S is the area bounding the armature cross-section; n is the unit vector of the normal to the surface of the armature.

The force pulse determining the force action on the armature from the inductor side is described by the expression:

$$F_z = \int_0^t f_z \, dt \, . \tag{5}$$

The velocity v_z of the armature with AE along the z-axis is described by the equation [3]:

$$(m_2 + m_e)\frac{dv_z}{dt} = f_z(z) - k_P \Delta z(t) - k_T v_z(t) - \\ - 0.125 \pi \gamma_a \beta_a D_{ex2}^2 v_z^2(t), \tag{6}$$

where m_2 is the armature mass; m_e is the AE mass; k_P is the coefficient of elasticity of the buffer element, e.g. spring; k_T is the coefficient of dynamic resistance; γ_a – is the air density; β_a is the aerodynamic resistance coefficient; D_{ex2} is the outer diameter of the armature; Δz is the value of the armature displacement.

Equations (1) – (6) describe electromechanical process in the LPEC at initial conditions: $u_c(0)=U_0$; $i_1(0)=0$; $\Delta z(0)=0$; $v_z(0)=0$, where u_c is the CES voltage.

In the calculation, we assume the absence of mechanical movements (recoil) of the inductor, the deformation of the elements, and the strictly axial disposition and movement of the armature relative to the inductor.

The solution of the system (1) – (6) is obtained using the finite element method with integration over spatial variables and the improved Gear method in time integration. When moving the armature, a «deformable» mesh is used. To solve the problem, the computer model of LPEC was developed in the software package *Comsol Multiphysics* which allows adaptively changing the mesh and monitoring errors when working with various numerical solvers [9]. The estimated time step automatically is varied depending on the convergence conditions and the error indices of the solutions obtained. The solution of the system of equations is performed using the BDF (*backward differentiation formula*) method with fixed time step, irregular mesh and using the PARDISO solver.

The main parameters of the LPEC. Let's consider LIPEC with electrically conductive, coil and ferromagnetic armature, and unchanged dimensions. LPEC has a coaxial configuration and contains a FS covering the inductor from the end and outer sides [6]. The armature is made in as a flat disk, one side of which faces the inductor, and the second one interacts with the AE. The main parameters of the LPEC are:

Inductor: outer diameter D_{ex1}=100 mm, inner diameter D_{in1}=10 mm, section of copper bus $a \times b$=1.8×4.8 mm², the number of turns of the bus $N = 46$;

FS: the height of the disk base H_{3a}=8 mm, the outer diameter of the shell D_{ex3b}=118 mm, the inner diameter of the shell D_{in3b}=102 mm.

CES: capacitance C=2850 µF, voltage U_0=400 V. The electronic system forms an aperiodic pulse of excitation of the inductor using an inverse diode [5].

Weight of the AE m_e=0.5 kg.

The EA is made as a massive disk of technical copper, and the CA and FA are made of a magnetodielectric with the magnetic properties of steel Ст.10. The CA and inductor are made with the same geometric parameters and are wound with a copper bus.

Table 1 shows the differing parameters of the LPEC elements due to the type of armature.

Influence of armature height on LPEC indicators. Electromechanical characteristics of the LPEC with EA, CA, and FA are presented in [10]. We consider the influence of the height of the armature of these types on the LPEC on the maximum velocity V_m and the valueof the impulse of the electrodynamic or electromagnetic force acting on the armature. Despite the different structure of the movable armature in the converters under consideration, they can realize different heights while preserving the remaining parameters. The height of the EA and the FA is determined by the height of the copper and ferromagnetic disks, respectively. The height of the CA is determined by the width of the bus with an unchanged number of its turns.

Table 1

Different LPEC parameters

Indicator, designation, unit	LPEC armature type		
	CA	FA	EA
Inductor height, H_1, mm	5	10	10
Armature outer diameter, D_{ex2}, mm	100	118	100
Armature inner diameter, D_{in2}, mm	10	0	6
Armature height, H_2, mm	5	5	2.5
Initial distance between inductor and armature, Δz_0, mm	1	5	1
Armature mass, m_2, kg	0.345	0.535	0.205
FS shell height, H_{3b}, mm	24	21	24

The cross-section of the inductor bus remains unchanged. We introduce a dimensionless geometric parameter characterizing the height of the armature:

$$\varepsilon = \frac{H_2}{H_1} \, . \tag{7}$$

Let's consider the range of the height variation of armature, in which the maximum speed of the armature with the AE V_m is located (Fig. 1). When the height of the armature is increased, an increase in the force impulse F_z occurs in all LPECs. When the geometric parameter ε of the CA is changed from 0.2 to 1.2, the value of the force impulse F_z increases by a factor of 2.03.When the geometric parameter ε of the FA changes from 0.4 up to 1.4, the value of F_z increases by a factor of 2.52. And when the parameter ε of EA changes from 0.1 to 0.5, the value of F_z increases by 1.94 times. Thus, with increasing the height of the considered types of the armature in the LPED, the value of the electrodynamic force impulse F_z increases, but in different degrees.

With an increase in the height of the armature, an increase in its mass also occurs. This causes that, the maximum speed of the armature with AE V_m on the

specified height has a more complex dependence. The maximum values of the speeds of the types of LPEC armature considered are realized at different heights, which is the most rational for them. The least low, from this point of view, is the EA (H_2=2.2 mm), and the highest is the FA (H_2=10.5 mm). In the CA, the maximum speed is realized at the armature, the rational height of which is H_2=6.1 mm.

In Table 2 shows the values of the force impulse F_z and the maximum armature speed V_m at a rational height, which is represented as a geometric parameter ε. As follows from the obtained results, at a rational height of the armature, the fastest speed takes place in the LPEC with CA, and the smallest one in the LPEC with EA. In the LPEC with CA and FA, practically the same values of the electrodynamic and electromagnetic force impulse are

realized, while in the LPEC with EA the electrodynamic force pulse is 1.52 times smaller.

Fig. 2 shows the distribution of the magnetic flux density at the moment of the maximum force in the LPEC with different types of armature. In the LPEC with EA, the greatest magnetic flux density takes place in the gap between the inductor and the armature. At the same time, on the outer surface of the armature the field is almost completely shielded. In the LPEC with CA, the greatest magnetic flux density appears between the armature and the inductor, over which the same current flows. In this case, the magnetic field partially extends beyond the surface of the armature. In the LPEC with the FA, the maximum magnetic flux density occurs in the inner cylindrical core, which is covered by an inductor. In this case, a considerable magnetic flux density of the scattering field is observed.
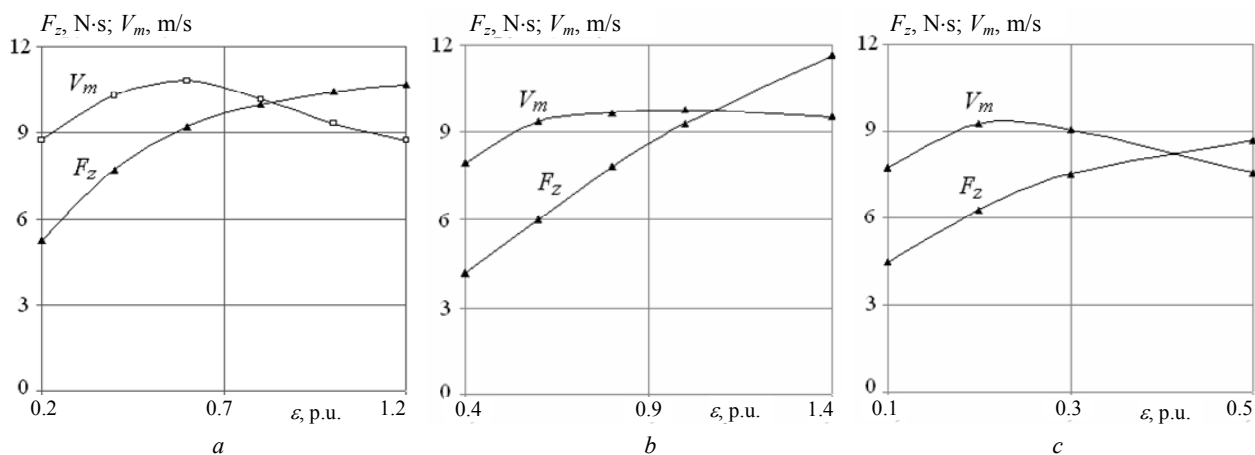
Fig. 1. The change in the moment of the force F_z and the maximum velocity V_m of the armature with AE as a function of the value of the parameter ε for: CA (*a*), FA (*b*), and EA (*c*)

Table 2

The F_z and V_m values for the LPEC with different types of armature for a rational value of the parameter ε

Armature type	ε^*, p.u.	F_z, N·s	V_m, m/s
EA	0.22	6.1	9.32
CA	0.61	9.3	10.82
FA	1.05	9.3	9.75

As calculations show that electromechanical processes occur most rapidly in the LPEC with CA, and

the current in the inductor and the electrodynamic forces take the greatest values. In the LPEC with FA, electromechanical processes proceed most slowly, and the maximum value of the electromagnetic forces here is the smallest. The velocities of the LPEC with CA and EA, where the electrodynamic repulsive forces act, after a sharp initial increase practically do not change. In LPEC with FA, where the electromagnetic force of attraction acts, the indicated speed constantly increases until the moment of the armature collision with the FS.

Fig. 2. The distributions of the magnetic flux density in the LPEC with EA (*a*), CA (*b*), and FA (*c*) at the moment of the maximum of the force: 1 – inductor, 2 – armature, 3 – FS

Evaluation of the efficiency of LPEC. To evaluate the LPEC with different types of armature, having a rational height at which the fastest armature speed with AE takes place, we introduce the integral efficiency indicator K^* [11]. This indicator in a relative form takes into account the force, speed, power, electrical and field (magnetic flux density of the field of scattering) indicators:

$$K^* = \beta\left(\alpha_1 f_{zm}^* + \alpha_2 V_m^* + \alpha_3 W_{kin}^* + \frac{\alpha_4}{j_{1m}^*} + \frac{\alpha_5}{B_{ex}^*}\right), \quad (8)$$

where j_{1m} is the maximal current density in the inductor, f_{zm} is the maximum value of the force acting on the moving armature from the side of the inductor, V_m is the maximum value of the speed of the armature with AE, W_{kin} is the kinetic energy of the LPEC, B_{ex} is the averaged value of the magnetic flux density of the field of scattering, β is the armature reliability factor, α_j are the weight factors of the corresponding LPEC indicators satisfying the relation:

$$\sum_{j=1}^{5} \alpha_j = 1 . \quad (9)$$

The averaged value of the magnetic flux density of the field of scattering B_{ex} is calculated on the contour located at a distance $2H_1$ from the lower end and side sides and at a distance $4H_1$ from the upper side of the inductor.

All LPEC indicators are normalized with respect to the LPEC with EA and marked with asterisks. Thus, the integral indicator of the efficiency of the LPEC with EA $K^*=1$.

We use the reliability factors for the FA $\beta = 1.2$, for the EA $\beta = 1$, for the CA $\beta = 0.8$. The increased reliability of the FA is due to the design of a massive ferromagnetic disk. The lower reliability of the EA is due to the cdesign of a thin-walled copper disk that is less stable to electrodynamic forces. Even lower reliability of the CA is due to the presence of a movable contact between the inductor and the armature, which is made in the form of a multi-turn coil compounded with epoxy resin.

Let's consider several variants of the strategy for assessing the efficiency of the LPEC (Table 3). The priority of the LPEC indicator is estimated by the value of the corresponding weighting coefficient α_j.

Table 3

Variants of the evaluation strategy and the values of the integral indicator of the efficiency of the LPEC with FA and with CA, p.u.

Variant	α_1	α_2	α_3	α_4	α_5	K^* (with FA)	K^* (with CA)
I	0.2	0.2	0.2	0.2	0.2	0.703	1.518
II	**0.4**	0.15	0.15	0.15	0.15	0.656	1.556
III	0.15	**0.4**	0.15	0.15	0.15	0.676	1.335
IV	0.15	0.15	**0.4**	0.15	0.15	0.720	1.474
V	0.15	0.15	0.15	**0.4**	0.15	0.829	1.218
VI	0.15	0.15	0.15	0.15	**0.4**	0.631	2.004
VII	**0.35**	0.1	0.1	0.1	**0.35**	0.584	2.043
VIII	0.1	**0.35**	0.1	0.1	**0.35**	0.605	1.822

In the variant of strategy VII in which the highest priority is given to the amplitude of the force acting on the armature and the value of the magnetic flux density of the scattering field, the efficiency of the LPEC with the FA is the smallest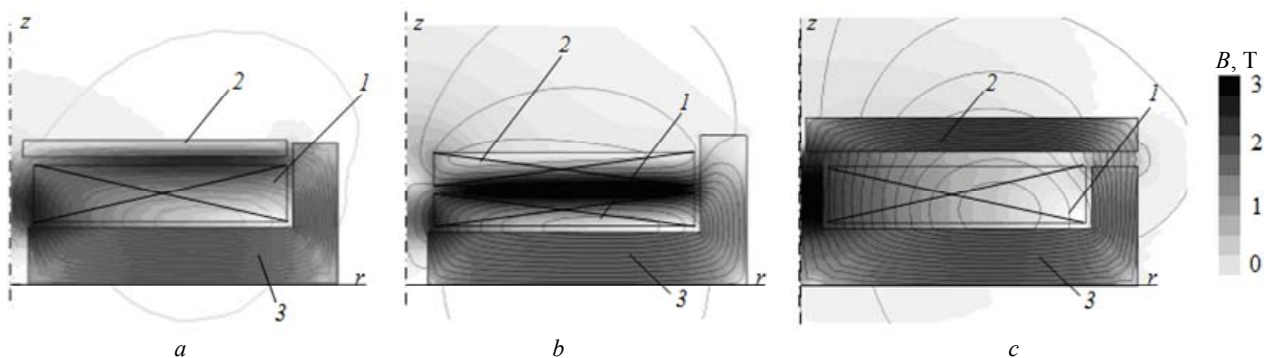, and the efficiency of the LPEC with CA is the largest. In the variant of strategy V in which the highest priority is given to the value of the inductor current pulse, the efficiency of the LPEC with FA is greatest, and the efficiency of the LPEC with FA is the smallest although it is constructively the simplest.

Thus, for all efficiency assessment strategies, the LPEC with CA is the most effective, even in spite of its constructive complexity, and the LPEC with FA is the least effective, although it is constructively the simplest.

Conclusions.

1. A mathematical model of the LPEC has been developed which describes fast and interconnected electromagnetic and electromechanical processes manifested when the armature moves relative to the inductor which is excited by the CES.

2. It is shown that as the height of the electrically conducting, coil and ferromagnetic armature of the LPEC increases, the force impulse increases.

3. The greatest speed takes place in LPEC with CA, and the smallest one in LPEC with EA. In the LPEC with CA and FA, practically the same values of the electrodynamic and electromagnetic force impulse are realized, while in the LPEC with EA the electrodynamic force impulse is 1.52 times smaller.

4. Using the integral efficiency indicator which takes into account in a relative way the force, speed, power, electrical and field indicators, it is established that for all evaluation strategies the LPEC with CA is most effective, even in spite of its constructive complexity, and the LPEC with FA is the least efficient, although it is constructively the simplest.

REFERENCES

1. Balikci A., Zabar Z., Birenbaum L., Czarkowski D. Improved performance of linear induction launchers. *IEEE Transactions on Magnetics*, 2005, vol.41, no.1, pp. 171-175. **doi: 10.1109/tmag.2004.839283.**

2. Bissal A., Magnusson J., Engdahl G. Comparison of two ultra-fast actuator concept. *IEEE Transactions on Magnetics*, 2012, vol.48, no.11, pp. 3315-3318. **doi: 10.1109/tmag.2012.2198447.**

3. Bolyukh V.F., Luchuk V.F., Rassokha M.A., Shchukin I.S. High-efficiency impact electromechanical converter. *Russian electrical engineering*, 2011, vol.82, no.2, pp. 104-110. **doi: 10.3103/s1068371211020027**.

4. Young-woo Jeong, Seok-won Lee, Young-geun Kim, Hyun-wook Lee. High-speed AC circuit breaker and high-speed OCD. *22nd International Conference and Exhibition on Electricity Distribution (CIRED 2013)*, 2013, 10-13 June, Stockholm, Paper 608. **doi: 10.1049/cp.2013.0834.**

5. Bolyukh V.F., Shchukin I.S. *Lineinye induktsionno-dinamicheskie preobrazovateli* [Linear induction-dynamic converters]. Saarbrucken, Germany, LAP Lambert Academic Publ., 2014. 496 p. (Rus).

6. Bolyukh V.F., Oleksenko S.V. The influence of the parameters of a ferromagnetic shield on the efficiency of a linear induction-dynamic converter. *Russian Electrical Engineering*, 2015, vol.86, no.7, pp. 425-431. **doi: 10.3103/s1068371215070044.**

7. Bolyukh V.F., Oleksenko S.V., Shchukin I.S. Comparative analysis of linear pulse electromechanical converters

electromagnetic and induction types. *Technical Electrodynamics*, 2016, no.5, pp. 46-48. (Rus).

8. D.-K. Lim, D.-K. Woo, I.-W. Kim, D.-K. Shin, J.-S. Ro, T.-K. Chung, H.-K. Jung. Characteristic Analysis and Design of a Thomson Coil Actuator Using an Analytic Method and a Numerical Method. *IEEE Transactions on Magnetics*, 2013, vol.49, no.12, pp. 5749-5755. **doi: 10.1109/tmag.2013.2272561**.

9. Comsol Multiphysics modeling and simulation software. Available at: http://www.comsol.com (accessed 05 May 2015).

10. Bolyukh V.F., Oleksenko S.V., Shchukin I.S. Efficiency of linear pulse electromechanical converters designed to create impact loads and high speeds. *Electrical engineering & electromechanics*, 2015, no.3, pp. 31-40. (Rus). **doi: 10.20998/2074-272X.2015.3.05.**

11. Bolyukh V.F., Kocherga A.I., Shchukin I.S. Multicriterial selection of parameters of the external screen of a linear pulse electromechanical transducer. *Electrotechnic and computer systems*, 2017, no.25(101), pp. 106-116. (Rus).

V.F. Bolyukh[1], *Doctor of Technical Science, Professor,*
A.I. Kocherga[1], *Postgraduate Student,*
I.S. Schukin[2], *Candidate of Technical Science, Associate Professor,*
[1] National Technical University «Kharkiv Polytechnic Institute»,
2, Kyrpychova Str., Kharkiv, 61002, Ukraine,
phone +380 57 7076427,
e-mail: vfbolyukh@gmail.com
[2] Firm Tetra, LTD,
2, Kyrpychova Str., Kharkiv, 61002, Ukraine,
phone +380 57 7076427,
e-mail: tech@tetra.kharkiv.com.ua

O. Petrenko, B. Liubarskiy, V. Pliugin

DETERMINATION OF RAILWAY ROLLING STOCK OPTIMAL MOVEMENT MODES

Purpose. To develop a methodology for simulating of an electromotive railway rolling stock in terms of power-optimal modes on a track with a given profile and a set motion graph. Methodology. We have used combined genetic algorithm to determine optimum modes of an electromotive railway rolling stock motion: a global search is performed by a genetic algorithm with a one-point crossover and roulette selection. At the final stage of the optimization procedure we have used Nelder-Mead method for the refinement of the optimum. Results. We have obtained that traction motor on a tramcar, while driving on a fixed site, has an excessive power of the cooling system. Its using only in the considered area allows to modernize the cooling system in the way of its power reducing, which in turn provides an opportunity to increase the overall efficiency of the electromotive railway rolling stock. Originality. For the first time, we have obtained the train motion equation in the program-oriented form. This allows to use it for determination of electromotive railway rolling stock optimal control laws according to the Hamilton-Jacobi-Bellman method. Practical value. We have made the computer program to determine optimum modes of an electromotive railway rolling stock motion. The experimental studies of program results for the track section have confirmed the adequacy of the model, which allows to solve the traffic modes optimization problem for the tram track sections and increase the overall efficiency of the electromotive railway rolling stock. References 19, figures 3.
Key words: **electromotive railway rolling stock, genetic algorithm, cooling system, traction motor, tramcar, control laws, optimization problem, efficiency.**

Разработана методика моделирования движения асинхронного тягового двигателя при движении электроподвижного состава по энергооптимальным режимам на участке пути с заданным профилем и установленным графиком движения. Определены оптимальные режимы движения электроподвижного состава на основе метода Гамильтона-Якоби-Беллмана. Определение режимов работы тягового привода предложено проводить заранее на основании решения задачи условной оптимизации его режимов. Определение оптимальных режимов работы тягового привода было проведено на основе комбинированных методов условной минимизации функции. Использование предлагаемой методики позволяет повысить общий КПД электроподвижного состава. Библ. 19, рис. 3.
Ключевые слова: **электроподвижной состав, генетический алгоритм, система охлаждения, тяговый двигатель, вагон трамвая, законы управления, проблема оптимизации, коэффициент полезного действия.**

Introduction. The processes of energy conversion in traction electromechanical converters (traction motors) relate to constant losses in different elements of its construction. The most of power loss are caused by physical processes of energy conversion [1-5]. The temperature of the traction motors design parts increases with the operating time and may exceed the permissible design limitations. This is especially true for the windings insulation temperature, which is limited to the thermal class of applied insulation [2-5]. To reduce the temperature on traction motors, cooling systems that increase the efficiency of the heat transfer of the motor construction components are used.

However, cooling systems need additional costs for their efficient work, which in turn reduces the efficiency of the electric vehicle in general. Thus, the creation of an efficient cooling system for electromotive vehicles is one of the most important scientific and technical problems solved by many leading scientists in the field of railway transport [1-5].

The following ways are possible to solve this problem: reduction of losses in the elements of traction motors design and increase of efficiency of the cooling system. Optimization of traction motors designing processes, which is common in most enterprises of leading electrotechnical manufacturers, allows to create traction motors optimal by their efficiency [1].

However, the modes of their operation on the electromotive railway rolling stock (ERRS), which moves at different speeds and under different load conditions, significantly reduce its overall efficiency [1, 6-12].

Determination of optimal motion modes by energy consumption criteria can improve the efficiency of the cooling system of traction motors [1, 6-12].

The paper considers the solution of this problem for the most common motors in production now – an asynchronous traction motors (ATM) on the base of Hamilton-Jacobi-Bellman method.

The aim of the paper to improve the methodology of an electromotive railway rolling stock simulation in terms of power-optimal modes on a track with a given profile and a set motion graph.

The task of optimizing of the traction drive modes. The basic states of the simulation method for the electromotive rolling stock in terms of power-optimum modes at the track with a given profile and a fixed motion graph and initial developments were described in papers [17, 18]. In this paper we present the results of further authors researches that were begun in previous works.

The determination of the ATM-SVI circuit efficiency based on the approaches proposed in the works [1, 13] is carried out, which include the following: to solve the problem of determining the optimal modes of the traction drive, four problems of the conditional optimization of the parameters of the traction drive must be solved (in acceleration modes $U_{op} = 1$, regenerative braking mode $U_{op} = 5$, maintaining mode of a given movement speed $U_{op} = 2.3$).

The efficiency of the traction drive in a certain mode of its work will be evaluated according to the criterion of maximum of its efficiency, subject to compliance with the requirements imposed by the operation modes.

Therefore, the task of determining the efficiency of the traction drive is to find the extremum of the drive factor function.

The efficiency of the traction drive (Fig. 1) can be given under the next equation:

$$\eta_1 = \left| \begin{array}{cc} \left[\begin{array}{l} U_{op}=1; \\ \eta_1 \to \max, \\ F_d \to \max, \\ |F_d| < |F'_k|, \\ v < v_{\max} \\ F_d > 0 \end{array} \right. & \left\{ \begin{array}{l} U_{op}=2; \\ \eta_1 \to \max, \\ |F_d| < |F'_k|, \\ v < v_{\max} \\ F_d > 0 \end{array} \right. ; \\[2em] \left\{ \begin{array}{l} U_{op}=3; \\ \eta_1 \to \max, \\ |F_d| < |F'_k|, \\ v < v_{\max} \\ F_d < 0 \end{array} \right. ; & \left\{ \begin{array}{l} U_{op}=5; \\ \eta_1 \to \max, \\ F_d \to \min, \\ |F_d| < |F'_k|, \\ v < v_{\max} \\ F_d < 0 \end{array} \right. \end{array} \right.$$

(1)

where η_1 – efficiency of the asynchronous traction motor (ATM) circuit – standalone voltage inverter (SVI), U_{op} – the operation mode of an electromotive railway rolling stock (ERRS), F_d – traction or braking force created by ERRS, F'_k – limitation for engagement force of wheel-rail contact, v – railway rolling stock speed, $v_{\max}$ – constructive movement speed. $U_{op} = 4$ – outburst mode is an idle mode, so it is not considered in determining of drive efficiency.

For each of these tasks, it is necessary to consider two modes: the use of single-time or spatial-vector pulse-width modulation (PWM). The mode of acceleration and regenerative braking are similar. Apply the method of vector objective functions proposed in [1, 14]. As a target function for the acceleration mode, we select a vector function with the next parameters:

$$F_{c1} = \begin{bmatrix} 1-\eta_1 \to \min, \\ -F_d \to \min, \end{bmatrix}.$$

(2)

The first component is chosen in such way that when it is minimized, the maximization of the efficiency of the traction drive can be obtained.

For regenerative braking mode, the vector target function has the form:

$$F_{c5} = \begin{bmatrix} 1-\eta_1 \to \min, \\ F_d \to \min, \end{bmatrix}.$$

(3)

For a given speed maintaining mode we select as a target function:

$$F_{c3} = F_{c4} = 1-\eta_1 \to \min .$$

(4)

The value of losses, and hence the efficiency of the drive, can be determined based on the slip of the traction motor, the motor voltage (phase or line) and the rotation speed. Because the operating modes are determined for all motion speeds (ATD rotation speeds), the rotation speed is a predetermined constant given in solving problem of finding the optimal traction drive operation mode.

Thus, the target functions to determine the traction drive optimal operating modes were chosen, which allow to find the optimal traction drive modes when different PWM modes are using.

The general formulation of an optimal control in real time in [13] is described.

Software-oriented model of the ERRS motion. As an optimization method, a combined genetic algorithm was chosen: a global search is performed by a genetic algorithm with a one-point crossover and roulette selection. At the final stage of the optimization procedure, the refinement of the optimum by the Nelder-Mead method is carried out [1, 13-19].

Let us consider the representation of the train motion equation in the program-oriented form, which will allow to use it for determination of the optimal control laws according to the Hamilton-Jacobi-Bellman method.

In this paper, the forces and supports are calculated as follows:

Acceleration force F_A (for one time step)

$$F_A = m \frac{v(t)-v(t-tstep)}{tstep} ,$$

(5)

where m – train weight, a conjunction;

$$a = \frac{v(t)-v(t-tstep)}{tstep} ,$$

(6)

where a – the equivalent constant acceleration, which is subjected to a train at a speed difference $v(t) - v(t-tstep)$ in one time step, due to the assumption that for each time step the acceleration is constant and the speed is linearly dependent on the time for each time step.

The main resistance to rolling F_{rr} (for one time step).

Since the velocity is linearly dependent on the time for each transition (time step), the rolling resistance for each time step can be calculated according to the average speed step and is equal to:

$$v_{avg} = \frac{v(t)+v(t-tstep)}{2} .$$

(7)

Thus, the main motion resistance for each time step will be:

$$F_{rr} = a_{rr} + b\, v_{avg} + c\, v_{avg}^2 ,$$

(8)

where a_{rr}, b, c – coefficients which for the tram car T-3 VPA with a full load 30000 kg have the following values: 1500 N, 0 N·c/m, and 1.5 N·c^2/m accordingly.

As a result, the force for ERRS moving on *tstep*:

$$F_{tot} = (1+\gamma)F_A + F_{rr} + F_s + F_{rk} .$$

(9)

where F_s, F_{rk} – resistance forces from the slopes and curves determined by the following equations:

$$F_s = m\, g\, \frac{i}{1000} ,$$

(10)

$$F_{rk} = \frac{c_{r0}}{R - c_{r1}}\, m ,$$

(11)

where c_{r0}, c_{r1}– constants, determined by [15]; R – radius of the curve, i – slope, g – gravitational acceleration.

The required energy for movement on *tstep*, considering the limitations and the assumption that the velocity changes linearly over time, using [15] is listed below.

For the time step from the state n–1 to the state n, from the equation of equally accelerated motion, the traveled distance can be obtained by equations (13).

$$E = \sum_{t=tstep}^{T} \frac{sign}{(\eta_1)^{sign}} \begin{pmatrix} (1+\gamma)F_A + a_{rr} + \\ + b\,v_{avg} + \\ + c \cdot v_{avg}^2 + \dfrac{c_{r0}}{R - c_{r1}} \cdot m + \\ + mg\,\dfrac{i}{1000} \end{pmatrix} \times$$

$$\times \frac{v(t) + v(t-tstep)}{2} \cdot tstep$$

$$\left| (1+\gamma)F_A + a_{rr} + b*v_{avg} + \right.$$
$$\left. + c*v_{avg}^2 + \frac{c_{r0}}{R - c_{r1}} \cdot m + mg\,\frac{i}{1000} \right| \le$$

$$\le 9.81\,k_s m \cdot 1000$$

where k_s – the coefficient of clutch, which for the tram is 0.16, v_{avg} – average speed per step.

$$\Delta x_n = v_{n-1}\,\Delta t_n + \frac{1}{2}\,a_n\,\Delta t_n,$$

$$\Delta x_n = v_{n-1} * \Delta t_n + \frac{1}{2}\,\frac{v_n - v_{n-1}}{\Delta t_n}\,\Delta t_n^2 \Rightarrow$$

$$\Delta x_n = v_{n-1}\,\Delta t_n + \frac{1}{2}\,v_n\,\Delta t_n - \frac{1}{2}\,v_{n-1}\,\Delta t_n \Rightarrow \quad (13)$$

$$\Delta x_n = \frac{1}{2}\left(v_{n-1} + v_n\right)\Delta t_n \Rightarrow$$

$$x_n - x_{n-1} = \frac{1}{2}\left(v_{n-1} + v_n\right)\Delta t_n \Rightarrow$$

$$x_n = x_{n-1} + \frac{1}{2}\left(v_{n-1} + v_n\right)\Delta t_n .$$

where x_n, v_n, a_n – position of the train, its speed and acceleration at n step.

For one hour step we have:

$$x_t = x_{t-tstep} + \frac{1}{2}\left(v_{t-tstep} + v_t\right)tstep , \quad (14)$$

where x_t – final position of the train for one $tstep$; $x_{t-tstep}$ – the initial position of the train for one $tstep$.
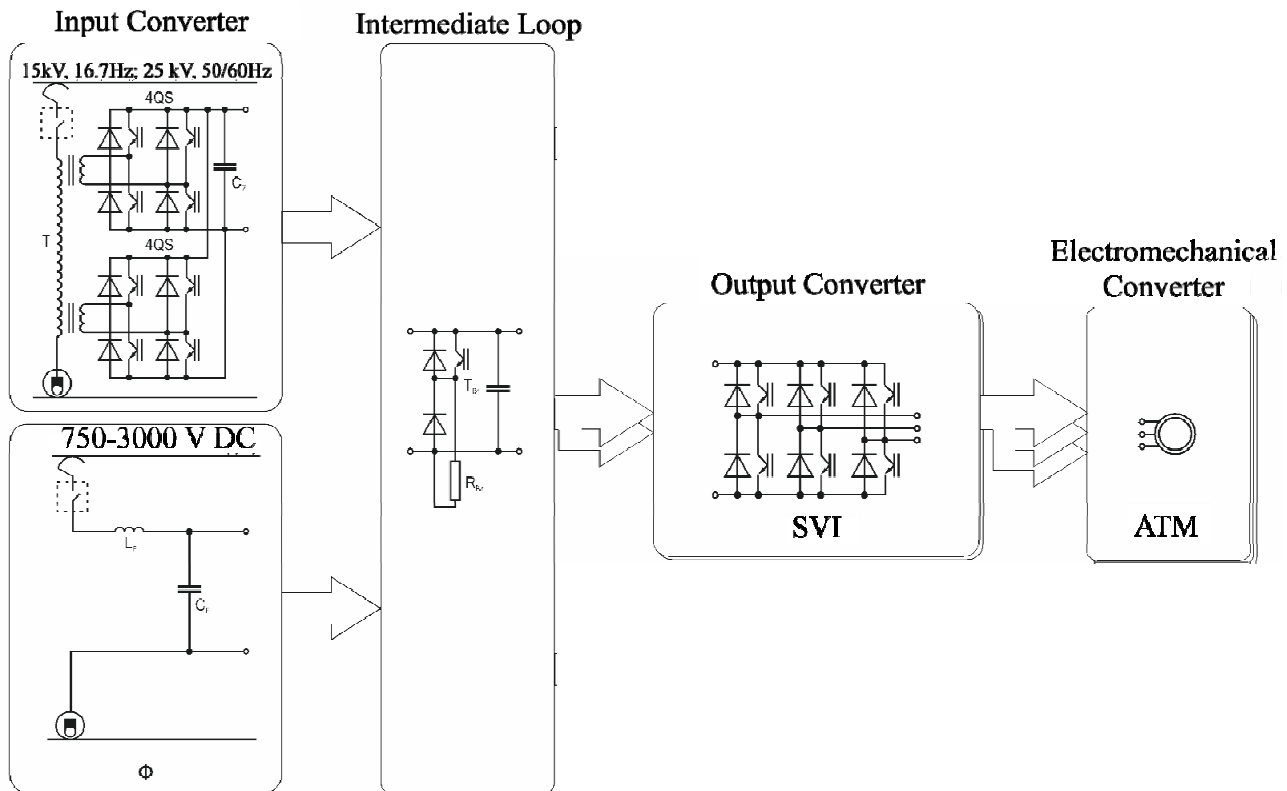
Fig. 1. The typical scheme of traction drive

Expression (14) gives the final position of the train for transfer, when the initial position, the initial and final velocities are known, as well as the value of the time step.

Thus, the resulting equations (12 – 14) allow to improve the simulation method of the electromotive rolling stock in terms of energy optimum modes.

The solution of the traffic modes optimization problem for the track section from the tram depot «Saltovske» to the turning circle of 602 district in Kharkiv and in the reverse direction was carried out. The results of solving the traction problem with tram traffic in optimal mode on Fig. 2 are shown. According to the results of solving the traction problem, the losses in the elements of the traction motor design on Fig. 3 are shown.

By means of a comparative analysis of experimentally determined and computing traction characteristics and efficiency values, the adequacy of the proposed mathematical model for the drive efficiency determination of the was established.

The maximum deviation in the calculation of losses is 7.42 %, which is quite acceptable for the carried-out calculations.
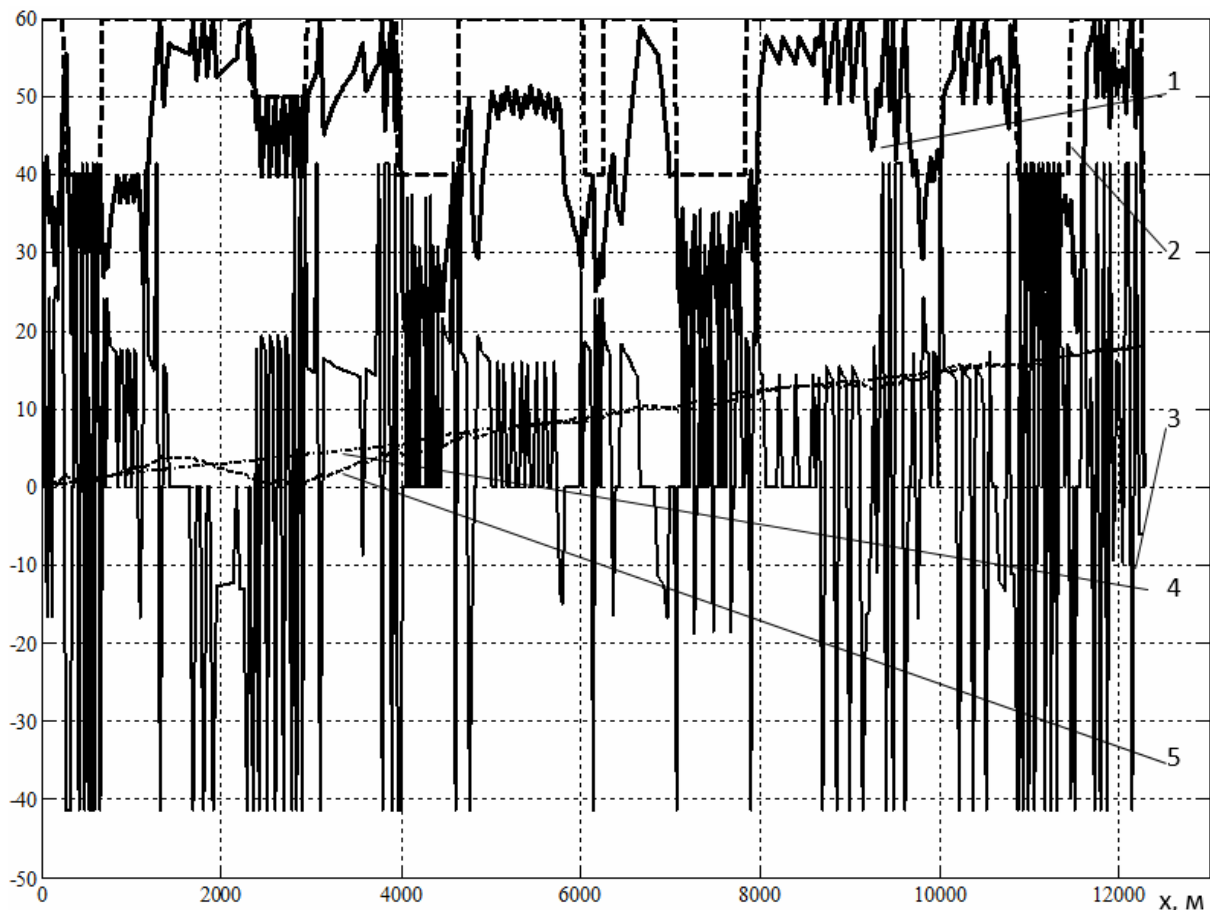
Fig. 2. The solution results of the traction movement task for the tramcar T-3VPA with traction motor AD931 on the track section
from the tram depot «Saltovske» to the turning circle of 602 district in Kharkiv and in the reverse direction:
1 – movement speed (v), km/h ; 2 – speed limitation , km/h; 3 – traction force, (F_{rr}) kN; 4 – movement time (t), min, 5 – losses (E), kW·h
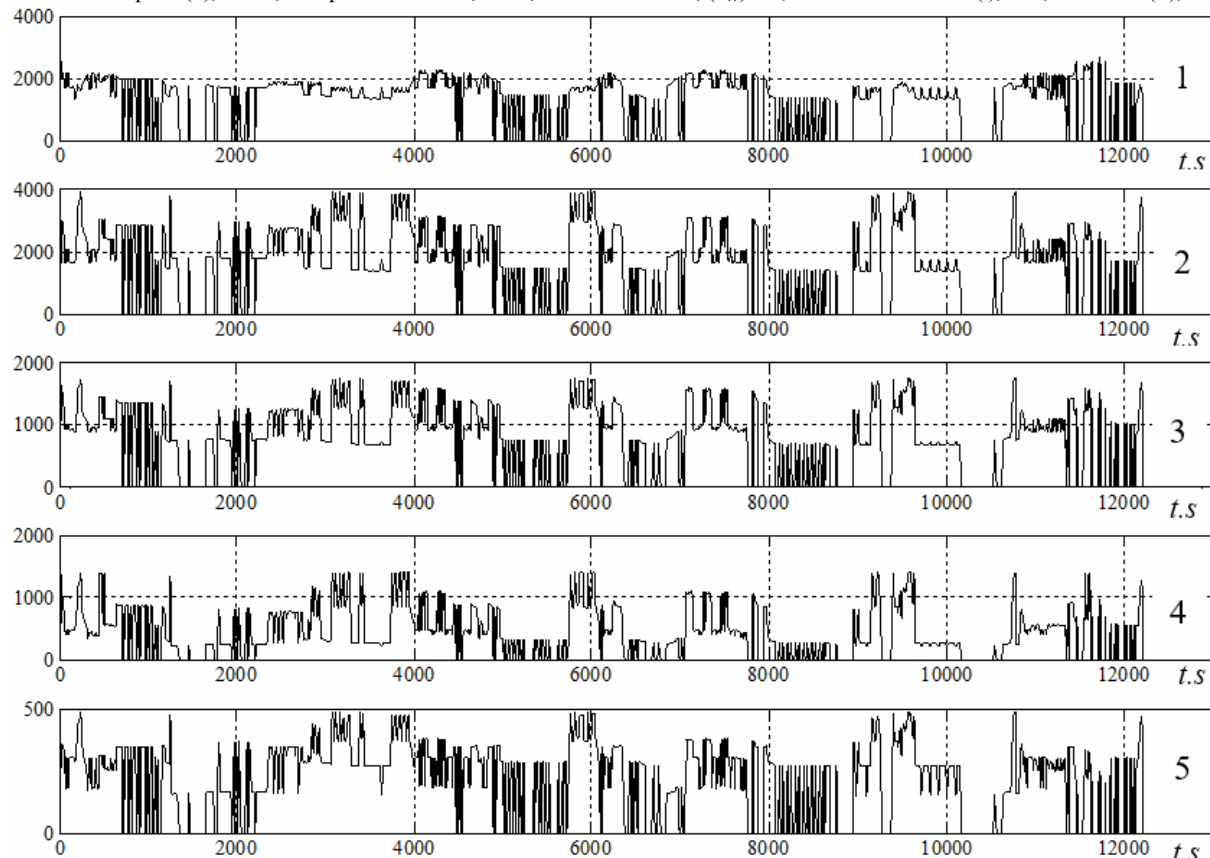
Fig. 3. Loses in traction motor: 1 – core loss P_1, W; 2 – rotor loss P_2, W; 3 – copper losses in stator winding at a slot part P_3, W;
4 – copper losses in stator winding at a front part P_4, W; 5 – mechanical losses P_5, W

Conclusions.

1. Using the genetic algorithm and the Yakobi-Hamilton-Belman method the calculated ratios for the determination of the railway electromotive traction drive efficiency are obtained. On this base the methodology of ATM motion simulation during the movement of the electromotive rolling stock according to the power-optimal regimes on the track section with the given graph and the set motion schedule is improved.

2. The adequacy of the obtained equations, which determine the efficiency both the maximum efficiency value of the ATM-SVI circuit in different operating modes under the coupling constraints, and constructive speed, is confirmed by the results of the experiment on the section of the tramway from the depot «Saltovske» to the turning circle of 602 district in Kharkiv. The maximum deviation in the calculation of losses does not exceed 7.42 %.

3. According to the results of solved traction problem, the change in losses in the elements of the traction tram traction design was first determined.

4. The use of advanced methodology is proposed to be carried out in advance based on solving the problem of work modes conditional optimization.

REFERENCES
1. Liubarskiy B.G. *Teoretychni osnovy dlya vyboru ta ocinky perspektyvnyh system elektromehanichnogo peretvorennya energiyi elektroruhomogo skladu. Diss. dokt. techn. nauk* [The theoretical basis for the selection and evaluation of advanced systems of electromechanical energy conversion of electric rolling stock. Doc. tech. sci. diss.]. Kharkiv, 2014. 368 p. (Ukr).
2. Petrenko O.M., Liubarskiy B.G., Riabov E.S. Investigation of the asynchronous traction motor windings temperature influence on the autonomous inverter voltage operating modes. *Electrification of transport*, 2016, no.12, pp. 87-91. (Rus).
3. Noskov V.I. Thermal modal traction engine locomotive. *Bulletin of NTU «KhPI»*, 2012, no.62(968), pp. 142-147. (Rus).
4. Kosmodanianskyi A.S. *Teoreticheskie osnovy i razrabotka system regulirovanija temperatury tjagovyh elektricheskih mashin lokomotivov. Diss. dokt. techn. nauk* [Theoretical foundations and development of temperature control systems for traction electric cars of locomotives. Doc. tech. sci. diss.]. Moscow, 2002. 285 p. (Rus).
5. Shcherbatov V.V., Rapoport O.L., Tsukublin A.B. Modeling the thermal state of the traction motor for resource forecasting. *Bulletin of the Tomsk Polytechnic University. Geo Assets Engineering*, 2005, vol.308, no.7, pp. 156-159. (Rus).
6. Getman G.K. *Nauchnye osnovy opredelenija racional'nogo moshhnostnogo rjada tjagovyh sredstv zheleznodorozhnogo transporta* [Rolling electrical complex on the basis of the criterion of minimizing the area under the curve of motion]. Dnipro, Dnipro National University of Railway Transport named after academician V. Lazaryan Publ., 2008. 444 p. (Rus).
7. Mokin O.B., Mokin B.I. *Modelyuvannya ta optymizaciya ruhu bagatomasovyh elektrychnyh transportnyh zasobiv poverhnyamy zi skladnym relyefom* [Modeling and optimization of movement of multi-mass electric vehicles with difficult terrain surfaces]. Vinnitsa, VNTU Publ., 2013. 192 p. (Ukr).
8. DmitrienkoV.D., Zakovorotnyi A.Yu. *Modelirovanie i optimizacija processov upravlenija dvizheniem dizel'-poezdov* [Modeling and optimization of diesel train trains control processes]. Kharkiv, NTMT Publ. Center, 2013. 248 p. (Rus).
9. Petrenko O.M., Liubarskiy B.G. Determination of the efficiency of the electromotive structure. Key points and approaches. *Information and control systems on the railway transport*, 2015, no.6, pp. 8-13. (Ukr).
*10.* Todorov E. Optimal control theory. *Bayesian Brain: Probabilistic Approaches to Neural Coding*, 2006, chap. 12, pp. 268-298. **doi: 10.7551/mitpress/9780262042383.003.0012.**
11. Kappen H.J. Optimal control theory and the linear Bellman equation. *Bayesian Time Series Models*, 2011, pp. 363-387. **doi: 10.1017/cbo9780511984679.018.**
12. Kanemoto Y. *Theories of urban externalities.* Holland, North-Holland Publ., 1980. 189 p.
13. Riabov E.S., Petrenko O.M., Overianova L.V. Analysis of losses in the traction induction motor under various power conditions. *Eurasian Union of Scientists*, 2016, no.12(33), chapt. 2, pp. 59-65. (Rus).
14. SeverinV.P., Nikulina E.N. *Metody odnomernogo poiska* [Methods of one-dimensional search]. Kharkiv, NTU KhPI Publ., 2013, 124 p. (Rus).
15. Panagiotis G. *Study on optimal train movement for minimum energy consumption.* Sweden, School of Innovation, Design and Engineering Publ., 2013. 82 p.
16. Balaji M., Kamaraj V. Design of high torque density and low torque ripple switched reluctance machine using genetic algorithm. *European Journal of Scientific Research*, 2010, vol.47, no.2, pp. 187-196.
17. Petrenko O.M., Domanskyi O.V., Liubarskiy B.G. Method of rolling stock asynchronous traction drive modes optimization. *Mechanics and engineer*, 2016, no.1, pp. 59-67. (Ukr).
18. Petrenko O.M., Liubarskiy B.G., Gliebova M.L. Software-oriented mathematical model of vehicle movement. *Bulletin of NTU «KhPI»,* 2016, no.6(1178), pp. 89-95. (Ukr).
19. Owatchaiphong S., Fuengwarodsakul N.H. Multi-objective based optimization for switched reluctance machines using fuzzy and genetic algorithms. *2009 International Conference on Power Electronics and Drive Systems (PEDS)*. **doi: 10.1109/peds.2009.5385926.**

O. Petrenko[1], Candidate of Technical Sciences, Associate Professor,
B. Liubarskiy[2], Doctor of Technical Sciences, Professor,
V. Pliugin[1], Doctor of Technical Sciences, Professor,
[1] O.M. Beketov National University of Urban Economy
in Kharkiv,
17, Marshal Bazhanov Str., Kharkiv, 61002, Ukraine,
e-mail: petersanya1972@gmail.com
[2] National Technical University «Kharkiv Polytechnic Institute»,
2, Kyrpychova Str., Kharkiv, 61002, Ukraine.

V.A. Yarovenko, P.S. Chernikov

A CALCULATION METHOD OF TRANSIENT MODES OF ELECTRIC SHIPS' PROPELLING ELECTRIC PLANTS

The purpose of the work is to develop the method for calculating the transient modes of electric ships' propelling electric plants during maneuver. This will allow us to evaluate and improve the maneuverability of vessels with electric motion. Methodology. The solution to the problems is proposed to be carried out on the basis of mathematical modeling of maneuvering modes. The duration of transient modes in an electric power plant at electric ships' maneuvers is commensurable with the transient operation modes of the vessel itself. Therefore, the analysis of the electric power plants' maneuvering modes should be made in unity with all the components of the ship's propulsion complex. Results. A specified mathematical model of transient regimes of electric ship's propulsion complex, including thermal motors, synchronous generators, electric power converters, propulsion motors, propellers, rudder, ship's hull is developed. The model is universal. It covers the vast majority of modern and promising electric ships with a traditional type of propulsors. It allows calculating the current values of the basic mode indicators and assessing the quality indicators of maneuvering. The model is made in relative units. Dimensionless parameters of the complex are obtained. These parameters influence the main indicators of the quality of maneuvering. The adequacy of the suggested specified mathematical model and the developed computation method based on it were confirmed. To do this, the results of mathematical modeling for a real electric ship were compared with the data obtained in the course of field experiments conducted by other researchers. Originality. The mathematical description of a generator unit, as an integral part of an indivisible ship's propulsion complex, makes it possible to calculate the dynamic operation modes of electric power sources during electric vessels' maneuvering. There is an opportunity to design the electric ships' propulsion power plant according to the final result – according to the indicators characterizing the vessel and its maneuvering properties. The use of a system of dimensionless units provides a generality to the results obtained. Electric ships with equal values of dimensionless parameters will have correspondingly the same values (in relative units) of maneuvering quality indicators. Practical value. The developed mathematical model and the research method constructed on its basis allow calculating the current values of the basic regime parameters of all the components of the ship's propulsion complex. A mathematical apparatus for estimating the main indicators of the quality of electric ships' maneuvering is proposed. There is an opportunity to improve the electric ships' maneuvering characteristics by optimizing the operation of propulsion motors.
References 21, tables 2, figures 3.
Key words: **electric ship's propelling electric plant, mathematical model of transient modes, calculation method.**

Целью работы является разработка метода расчета переходных режимов гребных электроэнергетических установок в составе судовых пропульсивных комплексов. Методика. На маневрах продолжительности переходных режимов в электроэнергетической установке соизмеримы с переходными режимами работы судна. Поэтому анализ маневренных режимов ее работы следует проводить в единстве со всеми составными частями судового пропульсивного комплекса. Результаты. Разработаны уточненная математическая модель и метод расчета переходных режимов всех составных частей пропульсивного комплекса электрохода на маневрах. Найдены безразмерные параметры комплекса. Они определяют основные показатели качества маневрирования. Адекватность модели и метода расчета подтверждены сравнением результатов математического моделирования с натурными экспериментами. Научная новизна. Метод расчета позволяет рассчитывать динамические режимы работы всех составных частей комплекса. Появляется возможность проектирования гребных электроэнергетических установок по конечному результату – по показателям качества маневрирования судна. Практическое значение. Метод расчета позволяет проводить исследования поведения пропульсивных комплексов на маневрах и отыскивать пути повышения маневренности электроходов. Библ. 21, табл. 2, рис. 3.
Ключевые слова: **электроэнергетическая установка электрохода, математическая модель переходных режимов, метод расчета.**

Actuality of the problem. In recent years, interest in the use of electromotion on ships of the merchant and navy has noticeably increased in the world shipbuilding industry. This is due to a number of undeniable advantages inherent in such a method of power transfer to propellers: the possibility of using high-speed thermal engines (TEs), using simplified design engines (non-reversible TEs are installed), splitting the total power into several parts and the ability of each heat engine to operate several screws which increases the vitality and flexibility of the power plant), the reduction of shaft length, the wide use of automation systems. The most important advantage of electromotion before the traditional drive of ship propulsors is the ability to provide high maneuverability of vessels equipped with this type of power plant. It is the maneuvering qualities of the propeller system that ensure, above all, the safety of maneuver operations by ships.

Modern rowing electrical installations (REIs) are built on the basis of induction frequency-controlled electric motors and based on valve propulsion motors. At the same time, a large number of vessels are in operation, the power plants of which are constructed using an alternating-direct current system. In this regard, both the design of modern electric trains with high maneuvering properties as well as the tasks of improving the management of rowing power plants of vessels in service are very relevant. Moreover, the need to assess the maneuverability of newly built electric boats is already at the initial stages of their design, and increasing the efficiency of performing maneuver

operations of existing vessels is undoubtedly relevant at any stage of their life cycle.

State of the issue under consideration. A distinctive feature of the work of electric boats on maneuvers is that the duration of the transient processes in the ship electric power plant (SEPP) is commensurate with the duration of the transient processes of the ship's movement. Therefore, the traditional assumptions about the constancy of the speed of the propellers during the movement of the ship on maneuvers (as well as vice versa) are not acceptable. All the components of the electric motor complex are in close interconnection. Only when solving particular problems is it permissible to consider any element of a single propulsion complex in isolation from the others. (This, in particular, refers to the steady movement). When analyzing unsteady regimes, propulsion power plants should be considered in unity with all other elements of the propulsion complex, including SEPP, propellers and hull. Only in this setting can a thorough analysis of their maneuvering operating modes and assess the maneuverability of the electric ship.

An analysis of the state of the issue under consideration shows the following. Studies of transient modes of operation of propulsion power plants have a long history. Numerous research works deal with the problems of analytical and machine methods of calculating the basic maneuvering regimes – starting, stopping, reversing propellers. However, even today they all have a serious shortcoming. In practice, only the electric part of the propulsion system (generators, propulsion motors, converters, control panels, control stations) is meant and implied under the electromotive system without primary engines and propulsors. In particular, this is clearly presented in [1-4]. The main distinguishing feature of these and other thorough works is that the speed of the vessel's motion is considered constant throughout the considered maneuvers. Thus, the propulsion system is considered in isolation from a single ship propulsion complex. Of course, as a result of this simplification, it is much easier to analyze the maneuvering modes of the REI operation, but at the same time, the accuracy of the results obtained is reduced and, most importantly, the system principle of the approach to the analysis of operating modes of ship electric power plants is violated. There is no possibility to evaluate the efficiency of the electric power plant operation according to the «final result» – in terms of the quality of the maneuver performance of the electric boat as a whole.

The second distinctive feature of earlier studies is that the overwhelming majority of them have been performed with respect to specific electric trains (at best – to specific series of electric boats), to specific propulsion systems. The results of the calculations obtained with the help of these methods refer to specific SEPPs and can not be extended to other electric vessels. This does not allow us to carry out wide, valid scientific generalizations. This reduces the scientific value of the results of the investigations carried out.

An attempt to eliminate these shortcomings was undertaken by one of the authors of this paper in [5]. To analyze the maneuvering regimes of rowing electric power plants as part of propulsion complexes of electric ships, he developed a corresponding mathematical model. It describes the transient modes of operation of all components of the complex. The model is universal, covers the vast majority of modern and prospective electric boats with a traditional type of propulsors. At the same time, when describing the processes occurring in thermal engines, a number of assumptions were adopted that do not allow analyzing the dynamic modes of their operation. In addition, a mathematical description of the processes occurring in synchronous generators was built on the basis of a vector diagram of the generator, which also made it impossible to fully appreciate the dynamic modes of their operation. Thus, the mathematical description of the transient modes of operation of diesel generators is in need of improvement, which led to the need for this work.

The goal of the paper is development of an improved mathematical model of transitional modes of propulsion power plants of electric boats and a method of calculating on its basis maneuverable modes of operation of ships.

The solution of the problem was carried out with reference to the most common electric-motive system – on the basis of frequency-controlled induction propulsion motors.

A method for solving the problem. The structural diagram of the SEPP «thermal engine – synchronous generator – frequency converter – induction motor» of the propulsion complex of the electric ship is shown in Fig. 1. It corresponds to the generally accepted in the theory of electromotion the layout of the electric power plant [14, 16, 20]. At the same time, in accordance with the goal, namely, the need to improve the design and management of electric power plants in terms of the quality of maneuver operations performed by the ship, it additionally includes propellers, the steering wheel and the body of the electric ship.

The propulsion complex consists of two «power» circuits. Here: thermal motors – D, synchronous generators (SG) – G, frequency converters of electricity – SE, induction propulsion motors (IPM) – M, propellers – P, rudder – H and hull.

Elements of the automatic control system and the main parameters linking the power units and control signals: speed regulators of the primary engine – DR; automatic voltage regulators of the generator – GR; M_D and ω_D – the torque and angular speed of rotation of the heat engine; M_G – electromagnetic torque of the generator; U_d and U_q – the generator voltage along the longitudinal and transverse axes (internal coordinates); I_d and I_q – generator currents along the longitudinal and transverse axes (internal coordinates); U_G – voltage at the generator output; ω_{Set} – set the angular velocity of the speed controller; ξ_D – the course of the fuel pump rail; $\Delta\xi_D$ – the increment in the stroke of the fuel pump rail; $1/T_s p$ – the link of the servomotor; K_{Fb} and K_{is} – the gain factors for the links of rigid and flexible (isodromic) feedbacks; U_f and I_f – excitation voltage and current of the synchronous generator; I_G, I_M – currents of SG and IPM; α_{Set} and γ_{Set} – relative frequency and voltage of the

converter (setting values); α and γ – the relative frequency and voltage at the output of the converter (taking into account the feedbacks); FC – the functional converter forming the law of frequency control $\gamma = f(\alpha)$; M_P and P_P – the torque and emphasis of propellers; M_M and ω_M – the torque and the angular velocity of the IPM rotation.

Isodromic all-regulators of indirect action are used as regulators of the rotation speed of the heat engine [8, 9]. As regulators of the voltage of synchronous generators [9, 10], combined (based on the control action and on the deviation of the regulated variable) regulators are used.
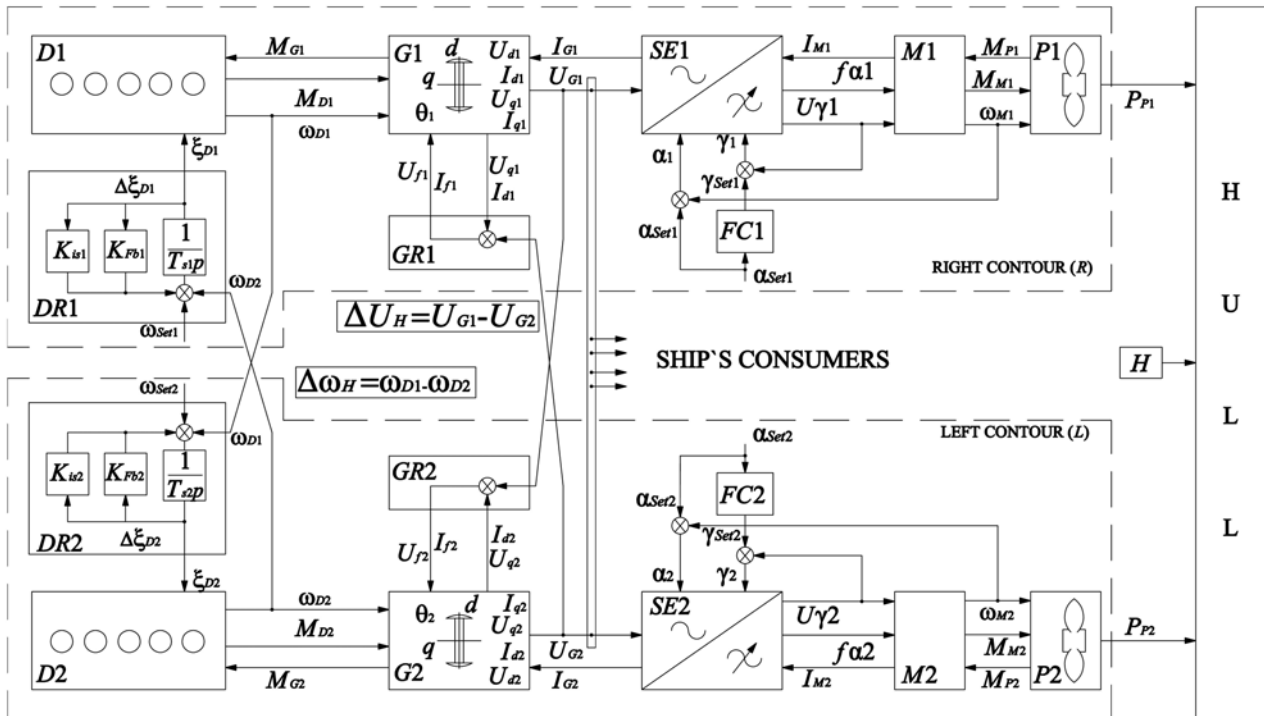
Fig. 1. Structural diagram of the propulsion complex of the electric ship

The system of equations describing the transient modes of operation of the electric power plant as part of the propulsion complex of the electric motor is presented below.

To make the results of the analysis more general, the model is reduced to relative units. As a result, the criteria for the dynamic similarity of propulsion complexes were revealed. These are the dimensionless parameters of the system «thermal engines – propulsion system – propulsors – hull». The ranges of the values of these parameters are found, covering the majority of series of electric boats with a traditional propeller drive. It is these parameters that determine the current values of the relative regime parameters of all components of the complex and determine the numerical values of the main quality indicators of maneuvering. This approach allows us to give a generality to the results obtained – electric vessels with equal values of dimensionless parameters will have the same values (in relative units) of the maneuvering quality parameters, respectively. There is an opportunity to generalize the results of research.

Relative values of performance indicators will be indicated by a symbol with a bar. (The index «0» corresponds to the values of the modes indicators when the electric motor operates in the nominal steady-state mode.)

For example, the relative electromagnetic torque of the generator:

$$\overline{M_G} = \frac{M_G}{M_{G0}}.$$

To simplify the perception of the material, the term «relative» is omitted from the text below.

The relative time is determined differently:

$$T = \frac{v_0}{L}t,$$

where v_0 is the vessel speed, L is the vessel length, t is the current time.

The final version of the generalized mathematical model of transient and steady-state operating modes of propulsion complexes of electric motors is presented below.

Heat engine and speed controller of its rotation.

Equation of motion of the heat engine [5]:

$$\frac{d\overline{\omega_D}}{dT} = N_D\left(\overline{M_D} - \overline{M_G}\right), \qquad (1)$$

where

$$N_D = \frac{M_{D0}L}{J_D\omega_{D0}v_0} \qquad (2)$$

is the criterion of dynamic similarity, J_D is the moment of inertia of the engine and the generator brought to the shaft of the heat engine.

The torque of the heat engine can be represented as the relative displacement of the fuel pump rail [8]:

$$\overline{M_D} = \overline{\xi_D}. \qquad (3)$$

The heat engine power:

$$\overline{P_D} = \overline{M_D \omega_D}.$$ (4)

The equations of transient processes in the regulator of the speed of rotation of a thermal engine, taking into account rigid and flexible feedbacks and taking into account the operation of the active power distribution system (with parallel running generating sets (GS)), can be represented as [9, 10].

Increment of the stroke of the fuel pump rail:

$$\frac{d\overline{\xi_D}}{dT} = K_P\left(1 - \left(\overline{\omega_D} - \Delta\overline{\omega_H}\right)\right) - K_{Fb}\overline{\Delta\xi_D} - K_{is}\overline{\Delta\xi_D},$$ (5)

where K_P, K_{Fb}, K_{is} are the gain factors for the regulated value (change in the speed of rotation of the heat engine), rigid feedback and flexible (isodromic) feedback, respectively;

$$\Delta\overline{\omega_{H1}} = \int_0^t \overline{U_{s1}}\,dt$$ (6)

is the difference in the angular frequencies of rotation of the generators;

$$\overline{U_{s1}} = \frac{\overline{I_{ae1}} - \overline{I_{ae2}}}{k_{ae1}}$$ (7)

is the voltage on the servomotor; k_{ae} is the gain factor of the automatic control loop of the active load distribution system;

$$\overline{I_{ae1}} = \overline{U_{d1}I_{d1}} + \overline{U_{q1}I_{q1}},$$ (8)

is the active component of the SG current.

For the heat engine of the second generator set, the equations are written similarly.

A synchronous generator and an automatic voltage regulation system. In contrast to the «classical» [11] description of the SG, processes that are incommensurable with the time constants of the main components of the propulsion complex of the electric drive are not taken into account here, namely, the transformer EMF in the stator windings [12]. In view of the smallness, we neglect the active resistance of the armature [13], the mutual inductance, which is incommensurably small in comparison with the inductance of the excitation winding, as well as the flux linkages of the damper windings.

The combined system of automatic voltage regulation of synchronous generators includes a control loop for reactive power distribution (with parallel GSs).

Switching angle:

$$\gamma_G = \arccos\left(1 - K_{\gamma G}\frac{|\overline{I_G}|}{|\overline{U_G}|}\right),$$ (9)

where

$$K_{\gamma G} = \frac{0{,}5\left(3x_d'' + x_q''\right)}{\sqrt{6}},$$ (10)

x_d'' and x_q'' are the supertransitive inductive resistance along the axes d and q.

Angle of phase shift between vectors $\overline{I_G}$ and $\overline{U_G}$:

$$\varphi_G = \frac{\gamma_G}{2}.$$ (11)

Angle of phase shift between vectors $\overline{E_G}$ и $\overline{I_G}$:

$$\psi_G = \operatorname{arctg}\left(\frac{\sin\varphi_G}{\cos\varphi_G} + \frac{x_q\overline{I_G}}{\overline{U_G}\cos\varphi_G}\right),$$ (12)

where x_q is the synchronous inductive resistance along the axis q.

Angle of phase shift (load angle) between vectors $\overline{E_G}$ and $\overline{U_G}$:

$$\theta_G = \psi_G - \varphi_G.$$ (13)

Generator currents (internal coordinates d-q):

$$\overline{I_d} = -\overline{I_G}\sin\psi_G,$$ (14)

$$\overline{I_q} = \overline{I_G}\cos\psi_G.$$ (15)

Generator voltages (internal coordinates d-q):

$$\overline{U_d} = -K_{d1}\overline{I_G}\cos\psi_G,$$ (16)

$$\overline{U_q} = -K_{q1}\overline{I_G}\sin\psi_G + K_{q2}\overline{I_f},$$ (17)

where I_f is the current of the field winding of the generator.

Increment of the excitation current:

$$\frac{d\overline{I_f}}{dT} = N_f\left(\begin{array}{c} K_{f1}K_{Uq}\overline{U_q} + K_{f2}K_{Id}\overline{I_d} - \\ -K_{f3}K_U\left(\overline{U_G} - \left(1 - \Delta\overline{U_{H1}}\right)\right) - \overline{I_f} \end{array}\right),$$ (18)

where

$$\Delta\overline{U_{H1}} = \frac{\overline{I_{re1}} - \overline{I_{re2}}}{k_{re1}}$$ (19)

generators' voltages difference;

$$\overline{I_{re1}} = \overline{U_{q1}I_{d1}} - \overline{U_{d1}I_{q1}}$$ (20)

s the reactive component of the SG current;

$$K_{d1} = \frac{\sin\theta_0}{\cos\psi_0},$$ (21)

$$K_{q1} = \frac{1 - \cos\theta_0}{\sin\psi_0},$$ (22)

$$K_{q2} = 1,$$ (23)

$$K_{Uq} = \frac{U_{G0}}{U_{f0}},$$ (24)

$$K_{Id} = \frac{I_{G0}x_d}{U_{f0}},$$ (25)

$$K_U = \frac{U_{G0}}{U_{f0}}$$ (26)

are the dimensionless parameters;

$$N_f = \frac{LU_{f0}}{L_fI_{f0}v_0}$$ (27)

is the criterion for dynamic similarity; L_f is the inductance of self-induction of the excitation winding; U_f and I_f are the voltage and current of the field winding; K_{f1}, K_{f2}, K_{f3} are the gain factors for the main signal, the disturbance and the deviation of the controlled variable, respectively; k_{re} is the gain factor of the automatic control loop of the reactive load distribution system.

Electromagnetic torque of the generator:

$$\overline{M_G} = -K_{G1}\overline{I_G^2}\sin\psi_G\cos\psi_G + K_{G2}\overline{I_f I_G}\cos\psi_G, \quad (28)$$

where

$$K_{G1} = \frac{(L_d - L_q)I_{G0}^2}{M_{G0}}, \quad (29)$$

$$K_{G2} = \frac{M_{ad}I_{f0}I_{G0}}{M_{G0}} \quad (30)$$

are the dimensionless parameters; L_d and L_q are the inductances of self-induction of the armature winding along the d- and q- axes; M_{ad} is the inductance of mutual induction along the d-axis.

The relations (9) – (30) were obtained in [6, 7].

Voltage on the generator output:

$$\overline{U_G} = \sqrt{\left(\overline{U_d^2} + \overline{U_q^2}\right)}. \quad (31)$$

Active power of the generator:

$$\overline{P_G} = \overline{U_G}\,\overline{I_G}\cos\varphi_G. \quad (32)$$

A converter of the electric power. Considering the frequency converter as a non-inertial «quantizer» of electricity with ideal gates, we do not take into account the electromagnetic processes taking place in it, and we consider that the current at the output of the converter is continuous, and the converter itself does not go beyond the region of normal loads [14]. The converter type is a frequency converter with an autonomous voltage inverter (FC with AVI).

Output voltage versus input one:

$$\overline{U_M} = \gamma\overline{U_G}, \quad (33)$$

where U_M is the IPM voltage

Rowing electric motor. In the mathematical model [5], a mathematical description of the generalized propulsion motor is given. As a special case from it, a mathematical model of an induction electric motor (IM) follows with frequency control. It is based on the exact classical scheme for the replacement of blood pressure, which determines the necessary assumptions and simplifications. The voltage at the stator terminals is considered to be sinusoidal, the saturation of the steel of the machine is not taken into account, the distribution of the flow along the arc of the air gap is assumed to be sinusoidal, the steel losses in the stator are taken into account approximately, and in the rotor are not taken into account [15, 16].

Equation of motion of the IPM:

$$\frac{d\overline{\omega_M}}{dT} = N_M\left(\overline{M_M} - \overline{M_P}\right), \quad (34)$$

where

$$N_M = \frac{M_{M0}L}{J_M\omega_{M0}v_0} \quad (35)$$

is the criterion of dynamic similarity;

$$\overline{M_M} = K_M\,\overline{I_M}\,\overline{\Phi_M}\cos\varphi_M \quad (36)$$

is the IPM torque;

$$\overline{I_M} = C_{M24}\gamma\frac{1}{\sqrt{C_{M17} + C_{M18}\alpha^2 + \dfrac{C_{M21} + C_{M22}\alpha^2}{\left(C_{M19}\alpha - C_{M20}\overline{\omega_M}\right)^2} + \dfrac{C_{M23}\alpha}{C_{M19}\alpha - C_{M20}\overline{\omega_M}}}} \quad (37)$$

is the motor current;

$$\overline{\Phi_M} = C_{M25}\gamma\sqrt{\frac{x_{2M}'^2\left(C_{M19}\alpha - C_{M20}\overline{\omega_M}\right)^2 + r_{2M}'^2}{\left(b_M^2 + c_M^2\alpha^2\right)\left(C_{M19}\alpha - C_{M20}\overline{\omega_M}\right)^2 + \left(d_M^2 + e_M^2\alpha^2\right)r_{2M}'^2 + 2r_{1M}r_{2M}'\alpha\left(C_{M19}\alpha - C_{M20}\overline{\omega_M}\right)}} \quad (38)$$

is the IPM magnetic flux;

$$\cos\varphi_M = \frac{1}{\sqrt{1 + C_{M26}\left(C_{M19}\alpha - C_{M20}\overline{\omega_M}\right)^2}} \quad (39)$$

is the motor power factor;

$$C_{M17} = \frac{b_M^2}{r_{2M}'^2}, \quad (40)$$

$$C_{M18} = \frac{c_M^2}{r_{2M}'^2}\alpha_0^2, \quad (41)$$

$$C_{M19} = \alpha_0, \quad (42)$$

$$C_{M20} = \frac{\omega_{M0}}{\omega_{1Mn}}, \quad (43)$$

$$C_{M21} = d_M^2, \quad (44)$$

$$C_{M22} = e_M^2\alpha_0^2, \quad (45)$$

$$C_{M23} = 2\frac{r_{1M}}{r_{2M}'}\alpha_0, \quad (46)$$

$$C_{M24} = \sqrt{C_{M17} + C_{M18} + \frac{C_{M21}}{\beta_{M0}^2} + \frac{C_{M22}}{\beta_{M0}^2} + \frac{C_{M23}}{\beta_{M0}}}, \quad (47)$$

$$C_{M25} = \sqrt{\frac{\left(b_M^2 + c_M^2\alpha_0^2\right)\left(C_{M19}\alpha_0 - C_{M20}\omega_{M0}\right)^2 + \left(d_M^2 + e_M^2\alpha_0^2\right)r_{2M}'^2 + 2r_{1M}r_{2M}'\alpha_0\left(C_{M19}\alpha_0 - C_{M20}\omega_{M0}\right)}{x_{2M}'^2 + \dfrac{r_{2M}'^2}{\beta_{M0}^2}}}, \quad (48)$$

$$C_{M26} = \frac{x_{2M}'^2}{r_{2M}'^2} \quad (49)$$

are the dimensionless parameters;

$$b_M = r_{1M}\left(1 + \tau_{2M}\right), \quad (50)$$

$$c_M = x_{0M}\tau_M, \quad (51)$$

$$d_M = \frac{r_{1M}}{x_{0M}}, \quad (52)$$

$$e_M = 1 + \tau_{1M} \quad (53)$$

are the constant coefficients of asynchronous frequency-controlled IPM;

$$\tau_{1M} = \frac{x_{1M}}{x_{0M}}, \qquad (54)$$

$$\tau_{2M} = \frac{x'_{2M}}{x_{0M}}, \qquad (55)$$

$$\tau_M = \tau_{1M} + \tau_{2M} + \tau_{1M}\tau_{2M} \qquad (56)$$

are the scattering coefficients; J_M is the moment of inertia of the motor; K_M is the constant constructive coefficient; ω_{1Mn} is the rotational frequency of the stator magnetic field; r_{1M} and r'_{2M} are the active resistances of stator and rotor (reduced); x_{1M} and x'_{2M} are the inductive resistance of the stator and rotor (reduced) of the IM; x_{0M} is the inductive magnetization resistance; β_{M0} is the absolute slip of the IM rotor. The relations (34) – (49) were obtained in [5].

Electric power plant control. Management is carried out from the control station (CS) on the bridge. The main task is to control the movement of the vessel in real time. The output signal of the CS forms two control actions on the frequency converter (with respect to the frequency α and the voltage γ).

Relative frequency of the output voltage of the frequency converter *SE* [5]:

$$\alpha = \alpha_{Set} - K_{\alpha P}\alpha_P - K_{\alpha\omega}\alpha_\omega - $$
$$- K_{\alpha f}\left(\alpha_f - \alpha_{f\,max}\right) - K_{\alpha M}\left(\alpha_M - \alpha_{M\,max}\right) -, \qquad (57)$$
$$- K_{\alpha I}\left(\alpha_I - \alpha_{I max}\right) - K_{\alpha PD}\left(\alpha_{PD} - \alpha_{PD\,max}\right)$$

where α_{Set} is the reference value of the relative frequency; α_P is the corrective communication for IPM power; α_ω is the corrective coupling for the angular velocity of rotation of the IPM; α_f is the cut-off according to the output frequency of the frequency converter; α_M is the cutoff on the torque of the IPM; α_I is the cutoff of the stator current of the IPM; α_{PD} is the cut-off according to the power consumed by the electromotive system; $K_{\alpha P}$, $K_{\alpha\omega}$, $K_{\alpha f}$, $K_{\alpha M}$, $K_{\alpha I}$, $K_{\alpha PD}$ are the gain factors that are determined by the particular control system.

Relative output voltage of the converter *SE* [5]:

$$\gamma = \gamma_{Set} - K_{\gamma I}\left(\gamma_\Gamma - \gamma_{I max}\right) - K_{\gamma U}\gamma_U, \qquad (58)$$

where γ_{Set} is the reference value of the relative voltage of the frequency converter – a signal that is a function of the relative frequency and the adopted voltage control law; γ_U is the corrective coupling for the IPM voltage; γ_I is the current stator cutoff of the IPM; $K_{\gamma I}$, $K_{\gamma U}$ are the gain factors. In each specific case, the automatic control system has its own «set» of control signals for each control channel. It is these control actions that directly affect the performance indicators of ship maneuver operations.

Propellers. The hydrodynamic reversal characteristic of the propeller, taking into account the ship's motion along a curvilinear trajectory, is represented in the form of a parabolic polynomial [17, 18].

Propeller torque:

$$\overline{M_P} = a_{21}\overline{\omega_P}^2 + b_{21}\overline{\omega_P v_e} + c_{21}\overline{v_e}^2 + a_M\overline{v}^2 tg^2\alpha_{Bev}, \quad (59)$$

where a_{21}, b_{21}, c_{21} are the coefficients of the universal characteristic of the screw (are constant in certain ranges of measurement of $\overline{\omega_P}$ and $\overline{v_e}$); $\overline{\omega_P}$ is the angular velocity of rotation of the propeller; $\overline{v_e}$ is the rate of

water leakage onto the propeller; $\overline{v}$ is the speed of the vessel; a_M is the constant coefficient; α_{Bev} is the angle of the bevel of the water flow.

Propeller stop:

$$\overline{P_P} = a_{11}\overline{\omega_P}^2 + b_{11}\overline{\omega_P v_e} + c_{11}\overline{v_e}^2 + a_P\overline{v}^2 tg^2\alpha_{Bev}, \quad (60)$$

where a_{11}, b_{11}, c_{11} are the coefficients of the universal characteristic of the propeller; a_P is the constant coefficient.

The body of the electric boat. The movement of the vessel along the free water surface in the associated coordinate system *GXYZ* whose origin coincides with the center of gravity of the vessel *G* is considered. The *GXY* plane is parallel to the ship's main plane, the *GX* axis is located in the center plane and directed to the bow, the *ZY* axis to the starboard, *GZ* axis – vertically up. The associated moment λ_{26} is neglected [19].

The components of the ship's speed along the axes *X*, *Y* and the speed of rotation around the *Z* axis:

$$\frac{d\overline{v_X}}{dT} = C_{\lambda 2}\overline{v_Y \Omega_Z} + $$
$$+ N_X\left\{\sum_J K_{Pj}\overline{P_{ej}} - C_{RX}\beta_{RP}\overline{v}^2 - \overline{R_X}\right\}, \qquad (61)$$

$$\frac{d\overline{v_Y}}{dT} = -\frac{1}{C_{\lambda 2}}\overline{v_X \Omega_Z} + $$
$$+ \frac{N_X}{C_{\lambda 2}}\left\{\sum_J K_{Pj}\alpha_{jz}\overline{P_{ej}} - C_{RY}\beta_{RP}\overline{v}^2 - \overline{R_Y}\right\}, \qquad (62)$$

$$\frac{d\overline{\Omega_Z}}{dT} = -\frac{N_\Omega}{N_X}C_{\lambda 21}\overline{v_X v_Y} + $$
$$+ N_\Omega\left\{\begin{matrix}\sum_j K_{Pj}h_{Pj}\overline{P_{ej}} + \left(\overline{M_{PZ}} - \overline{M_{DZ}}\right) + \\ + C_{RY}\overline{X_R}\beta_{RP}\overline{v}^2\end{matrix}\right\}, \qquad (63)$$

where

$$\overline{R_X} = \left\{\begin{matrix}C_{11}\cos 1{,}5\beta_{dr} - C_{12}\sin^4 1.5\beta_{dr} + \\ + C_{13}\left(\dfrac{2\beta_{dr}}{\pi}\right)^3\end{matrix}\right\}\overline{v}^2 \qquad (64)$$

is the longitudinal force of the rudder;

$$\overline{R_Y} = \left\{\begin{matrix}C_{21}\sin 2\beta_{dr}\cos\beta_{dr} + C_{22}\sin^2\beta_{dr} + \\ + C_{23}\sin^4 2\beta_{dr}\end{matrix}\right\}\overline{v}^2 \qquad (65)$$

is the transverse power of the rudder;

$$\overline{M_{PZ}} - \overline{M_{DZ}} = \left[\begin{matrix}C_{61}\sin 2\beta_{dr} + C_{62}\sin\beta_{dr} + \\ + C_{63}\sin^3 2\beta_{dr} + \\ + C_{64}\sin^4 2\beta_{dr}\end{matrix}\right]\overline{v}^2 - $$
$$- C_{65}\overline{\Omega_Z}\overline{v}^2 \qquad (66)$$

is the turning torque;

$$C_{\lambda 2} = \frac{m + \lambda_{22}}{m + \lambda_{11}}, \qquad (67)$$

$$C_{\lambda 21} = \frac{2(\lambda_{22} - \lambda_{11})}{m + \lambda_{11}}, \qquad (68)$$

$$C_{RX} = \frac{\mu_{rx} \frac{\rho}{2} v_0^2 S_C (1 - \psi)^2}{\sum K_{Pj} P_{ej0}}, \qquad (69)$$

$$C_{RY} = \frac{\mu_K \frac{\rho}{2} v_0^2 S_C (1 - \psi)^2}{\sum K_{Pj} P_{ej0}}, \qquad (70)$$

$$C_{11} = \frac{R_{X0}}{\sum K_{Pj} P_{ej0}}, \qquad (71)$$

$$C_{12} = \frac{0.07 \frac{\rho}{2} v_0^2 F_D}{\sum K_{Pj} P_{ej0}}, \qquad (72)$$

$$C_{13} = \frac{c_4 \frac{\rho}{2} v_0^2 F_D}{\sum K_{Pj} P_{ej0}}, \qquad (73)$$

$$C_{21} = \frac{0.5 C_Y^{\beta} \frac{\rho}{2} v_0^2 F_D}{\sum K_{Pj} P_{ej0}}, \qquad (74)$$

$$C_{22} = \frac{c_2 \frac{\rho}{2} v_0^2 F_D}{\sum K_{Pj} P_{ej0}}, \qquad (75)$$

$$C_{23} = \frac{c_3 \frac{\rho}{2} v_0^2 F_D}{\sum K_{Pj} P_{ej0}}, \qquad (76)$$

$$C_{61} = \frac{2m_1 \frac{\rho}{2} v_0^2 F_D}{\sum K_{Pj} P_{ej0}}, \qquad (77)$$

$$C_{62} = \frac{2m_2 \frac{\rho}{2} v_0^2 F_D}{\sum K_{Pj} P_{ej0}}, \qquad (78)$$

$$C_{63} = \frac{2m_3 \frac{\rho}{2} v_0^2 F_D}{\sum K_{Pj} P_{ej0}}, \qquad (79)$$

$$C_{64} = \frac{2m_4 \frac{\rho}{2} v_0^2 F_D}{\sum K_{Pj} P_{ej0}}, \qquad (80)$$

$$C_{65} = \frac{2\left[0.739 + 8.7\frac{T}{L}\right] C_{m0}^{\omega} \frac{\rho}{2} v_0^2 F_D}{\sum K_{Pj} P_{ej0}} \qquad (81)$$

are the dimensionless parameters;

$$N_X = \frac{L \sum K_{Pj} P_{ej0}}{(m + \lambda_{11}) v_0^2}, \qquad (82)$$

$$N_{\Omega} = \frac{L^3 \sum K_{Pj} P_{ej0}}{2(J_Z + \lambda_{66}) v_0^2} \qquad (83)$$

are the dynamic similarity criteria; X_R is the distance from the center of the coordinate system to the rudder; P_{ej} and K_{Pj} are the useful thrust of the propeller and its share in the total flow, respectively; L is the length of the vessel; m is the mass of the vessel; ρ is the specific density of water; λ_{11} и λ_{22} are the connected masses of water along the X and Y axes; λ_{66} is the connected moment of inertia of water; μ_{rx} is the drag coefficient of the rudder; μ_K is coefficient of lateral power of the rudder; ψ is the angle of the course; S_C is the reduced area of the rudder; c_4 is the coefficient of the longitudinal positional force of the water resistance; C_Y^{β}, c_2, c_3 are the coefficients of the body strength; m_1, m_2, m_3, m_4 are the coefficients of the positional moment of resistance; F_D is the reduced area of the submerged part of the ship's diametrical plane; M_{PZ} and M_{DZ} are the positional and damping moments of resistance; C_{m0}^{ω} is the coefficient of the damping moment of resistance; β_{dr} is the drift angle; J_Z is the moment of inertia of the vessel when it rotates about the Z axis.

Angle of attack of the helm:

$$\beta_{RP} = K_R \beta_R - \chi_C \left(\text{arctg} \beta_{dr} - \varepsilon \frac{\overline{\Omega_Z}}{\overline{v}} \right), \qquad (84)$$

where β_R is the angle of rotation of the helm; χ_C is the reduced coefficient of impact of the body and propellers on the rudder; ε is the value determined by the ratio l_R/L (l_R is the distance between the rudder and the midriangle frame). The relations $(61) - (84)$ were obtained in [5].

The developed mathematical model allows to comprehensively analyze transients of propulsion complexes of electric boats on maneuvers.

To analyze the maneuvering modes of operation, a package of applied programs has been developed. The base program is a program that allows calculating the laws of time variation of relative regime indicators, when the electric power performs a variety of maneuvers. At the same time during the analysis of maneuvering regimes:

• dimensionless parameters of the component parts of the complex are calculated;

• for the maneuver under study, the control parameters are entered in accordance with the positions of the handles of the control posts and the shifting of the rudder;

• initial conditions are given;

• according to the selected maneuvers, the laws governing each power circuit are formed;

• current values of the main mode parameters of each power circuit are calculated in the course of the maneuver;

• the hydrodynamic forces and torques acting on the vessel are determined; the current values of the ship's motion parameters in the coordinate system associated with it are calculated, and then in the unrelated coordinate system.

The solutions of the system of equations $(1) - (84)$ presented above is a solution of the Cauchy problem. The Runge-Kutta-Merson method was used as the solution method.

The final results of the calculations are presented in numerical form and in the form of ready-made graphs of the time variation of the mode indicators:

a) for each power circuit:

– angular speed of rotation – ω_D, torque – M_D and power of the heat engine – P_D;

– output voltage – U_G and current – I_G of the generator;

– excitation current of the generator – I_{fG};

– relative control voltage of the converter – γ;

– voltage – U_M and current – I_M of the propeller motor;

– torque – M_M and angular rotation speed – ω_M of the propulsion motor;

b) on the parameters of the vessel's movement:

– speed of movement – v;

– components of the speed v along the longitudinal axis $X - v_X$ and along the transverse axis $Y - v_Y$;

– angular velocity of rotation about the axis $Z - \Omega_Z$;

– angle of drift – β_{dr} and heading angle – ψ of the vessel.

If necessary, any other parameters, obtained during the calculation, can be recorded.

To confirm the adequacy of the developed mathematical model and the calculation method based on it, we compare the results of mathematical modeling with the data published in [20, 21] obtained in the course of field experiments by other researchers.

We use the oscillograms of acceleration and reversal of the propulsion power plant of the nuclear-powered ship «Arktika» presented in these publications.

Recalculated (for convenience of comparative analysis) into relative values, these oscillograms are shown, respectively, in Fig. 2, 3 by solid lines. Here, the dashed lines show the current values of the mode parameters obtained with the aid of the developed calculation method.
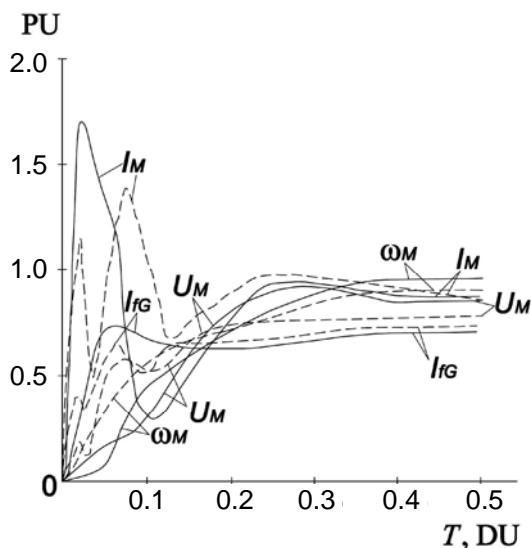
Fig. 2. Comparison of the theoretical calculation of the acceleration of the REI of the nuclear-powered electric ship «Arktika» with experimental data

The main parameters of the propulsion complex necessary for calculating the dimensionless parameters and the dynamic similarity criteria are presented in Table 1.

The generalized dimensionless parameters and the dynamic similarity criteria calculated from the above relationships are given in Table 2.
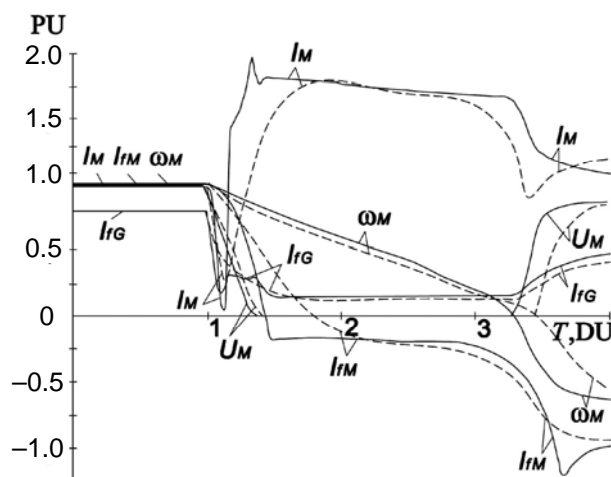
Fig. 3. Comparison of the theoretical calculation of the alternating reversals of the REI of the nuclear-powered electric ship «Arktika» with experimental data

Table 1

The main parameters of the propulsion complex

Length of the vessel by c.w.l.	136 m
Vessel speed	21 knots
Nominal parameters of thermal engines:	
power	27 600 kW
rotation speed	3500 RPM
Nominal parameters of synchronous generators:	
power	9000 kW
voltage	780 V
rotation speed	3500 RPM
power factor	0.88
winding data, p.u.:	
x_d	0.96
x_q	1.12
x''_d	0.14
x''_q	0.16
Nominal parameters of propulsion electric motors:	
power	17600 kW
Armature current	9200 A
rotation speed	130 RPM

Table 2

Dimensionless parameters and criteria for dynamic similarity of the nuclear-powered ship «Arktika»

K_M	K_{d1}	K_{q1}	K_{q2}	K_{G1}
1.071	1.12	0.294	1	−0.029
K_{G2}	N_D	N_{fG}	N_M	N_X
1.684	0.641	5.6	6.06	0.2
$K_{\gamma G}$	K_P	K_{Fb}	K_{is}	a_{21}
0.118	900	2	0.5	1.73
a_{11}	b_{21}	b_{11}	c_{21}	c_{11}
1.73	0.33	0.33	−1.06	−1.06

The control laws of each power circuit are given in the mathematical model in accordance with oscillograms of full-scale tests [16, 17]:

a) at acceleration $0 \leq T \leq T_1$:

$$\overline{U_{Gset}} = 0.8\left(1 - e^{-K_1 T}\right), \qquad (85)$$

$$\overline{U_{Mset}} = 1; \qquad (86)$$

b) at reversing from the forward to the rear $T_1 \le T \le T_2$:

$$\overline{U_{Gset}} = 0.8 - 1.5\left(1 - e^{-0.8K_2(T-T_1)}\right), \qquad (87)$$

$$\overline{U_{Mset}} = 1 - 1.5\left(1 - e^{-K_2(T-T_1)}\right) - \qquad (88)$$

for $\omega_M > 0$;

$$\overline{U_{Gset}} = 0.1 + 0.5\left(1 - e^{-1.5K_2(T-T_1)}\right), \qquad (89)$$

$$\overline{U_{Mset}} = -0.5 - 0.5\left(1 - e^{-K_2(T-T_1)}\right) - \qquad (90)$$

for $\omega_M \le 0$;

c) at reversing from the rear to forward $T_2 \le T \le T_3$:

$$\overline{U_{Gset}} = 0.1 + 0.7\left(1 - e^{-1.5K_3(T-T_2)}\right), \qquad (91)$$

$$\overline{U_{Mset}} = 0.5 + 0.5\left(1 - e^{-K_3(T-T_2)}\right) - \qquad (92)$$

for $\omega_M < 0$;

$$\overline{U_{Gset}} = 0.6 - 1.5\left(1 - e^{-0.8K_3(T-T_2)}\right), \qquad (93)$$

$$\overline{U_{Mset}} = -1 + 1.5\left(1 - e^{-K_3(T-T_2)}\right) - \qquad (94)$$

for $\omega_M \ge 0$;

where U_{Gset}, U_{Mset} are the control signals in the excitation systems of the SG and IPM, respectively; K_1, K_2, K_3 are the time constants.

The results of calculating the mode indicators (I_{fG}, U_M, ω_M, I_M) carried out according to the developed method in accordance with the relations (18), (33), (34), (37) in the qb64 application package, matlab are shown by dashed lines in Fig. 2, 3.

Comparison of the calculated results with the developed method with the experimental data shows a fairly good convergence. Trends in the change of mode indicators coincide. Certain discrepancies in the initial stages of transient processes are expected, and are explained by the settings and gain factors of the automatic control system, which for each ship have their own values.

Thus, the conducted studies confirm the acceptability of the proposed mathematical model and the developed method for calculating the maneuvering operating modes of electric vessels.

Conclusions:

1. A refined mathematical model and a method for calculating on its basis the operating conditions of propulsion power plants in the composition of propulsion complexes of electric boats are proposed. The method makes it possible to calculate the current values of the basic mode indicators both in the steady-state and in the dynamic modes of electric power plants, and evaluate the performance indicators of electric boats on maneuvers.

2. The adequacy of the developed method of calculation is confirmed by the results of full-scale tests conducted by independent researchers.

3. The use of the developed method of calculation opens up wide possibilities in the study of transient and steady-state operating conditions for propulsion complexes of vessels with electric movement.

REFERENCES
1. Vasin I.M *Sozdanie perspektivnykh elektrotekhnicheskikh i energeticheskikh kompleksov sudovykh edinykh elektroenergeticheskikh sistem. Diss. dokt. techn. nauk* [Creation of perspective electrotechnical and power complexes of ship single electric power systems. Doc. tech. sci. diss.]. St.-Petersburg, 2011. 445 p. (Rus).
2. Egorov L.E *Komp'iuternoe modelirovanie edinoi vysokovol'tnoi sudovoi elektroenergeticheskoi sistemy s propul'sivnymi kompleksami tipa azipod v normal'nykh i avariinykh rezhimakh raboty. Diss. kand. tech. nauk* [Computer modeling of a single high-voltage ship electric power system with propulsion complexes of the azipod type in normal and emergency operation modes. Cand. tech. sci. diss.]. St. Petersburg, 2014. 183 p. (Rus).
3. Hansen J.F. *Modeling and control of marine power system: Thesis for the degree of Philosophy Doctor.* Norwegian University of Science and Technology, 2008. 119 p.
4. Radan D. *Integrated control of marine electrical power system: Thesis for the degree of Philosophy Doctor.* Norwegian University of Science and Technology, 2008. 231 p.
5. Yarovenko V.A. *Raschet i optimizatsiia perekhodnykh rezhimov propul'sivnykh kompleksov elektrokhodov* [Calculation and optimization of transient regimes of propulsion complexes of electric vessels]. Odessa, Mayak Publ., 1999. 188 p. (Rus).
6. Yarovenko V.A., Podlyakh A.E., Chernikov P.S. The mathematical model of a synchronous generator in the composition of a propulsion complex of an electric vessel. *Bulletin of the ONMU*, 2011, vol. 33, pp. 35-45. (Rus).
7. Chernikov P.S. Investigation of transient regimes of generator aggregates of propulsion complexes of electric vessels. *Problems of technology: Scientific and production magazine*, 2011, no.3, pp. 45-55. (Rus).
8. Gorb S.I. *Analiz sistem avtomaticheskogo regulirovaniia chastoty vrashcheniia sudovykh dizel'nykh ustanovok* [Analysis of automatic control systems for the speed of ship diesel engines]. Moscow, Mortekhreklama Publ., 1989. 44 p. (Rus).
9. Tokarev L.N. *Sistemy avtomaticheskogo regulirovaniia* [Automatic control systems]. St. Petersburg, Notabene Publ., 2001. 190 p. (Rus).
10. Chan Viet Hung. *Issledovanie perekhodnykh protsessov v avariinykh rezhimakh sudovoi elektroenergeticheskoi sistemy. Diss. kand. tech. nauk* [Investigation of transient processes in the emergency modes of the ship electric power system. Cand. tech. sci. diss.]. St. Petersburg, 2007. (Rus).
11. Kopylov I.P. *Elektromekhanicheskie preobrazovateli energii* [Electromechanical energy converters]. Moscow, Energy Publ., 1973. 400 p. (Rus).
12. Konoplev K. G. *Impul'snoe regulirovanie sinkhronnykh generatorov* [Impulse regulation of synchronous generators]. Sevastopol, SevNTU Publ., 2008. (Rus).
13. Merkuriev G.V., Shargin Yu.M. *Ustoichivost' energosistem* [Stability of power systems]. St. Petersburg, NOU Center for the Training of Energy Personnel Publ., 2005. (Rus).
14. Kuznetsov N.A., Kuropatkin P.V., Khaikin A.B., Khomyakov N.M. *Osnovy proektirovaniia grebnykh elektricheskikh ustanovok* [Basic design of rowing electrical installations]. Leningrad, Shipbuilding Publ., 1972. 656 p. (Rus).
15. Bulgakov A.A. *Chastotnoe upravlenie asinkhronnymi dvigateliami* [Frequency Control of Asynchronous Motors]. Moscow, Energoizdat Publ., 1982. 216 p. (Rus).

16. Khaikin A.B., Vasilyev V.N., Polonsky V.I. *Avtomatizirovannye grebnye elektricheskie ustanovki* [Automated rowing electrical installations]. Moscow, Transport Publ., 1986. 424 p. (Rus).

17. Pershitz R.Ya. *Upravliaemost' i upravlenie sudnom* [Controllability and control of the ship]. Leningrad, Shipbuilding Publ., 1983. 272 p. (Rus).

18. Nebesnov V.I. *Voprosy sovmestnoi raboty dvigatelei, vintov, i korpusa sudna* [Questions of the joint operation of engines, propellers, and hull of the vessel]. Leningrad, Shipbuilding Publ., 1965. 247 p. (Rus).

19. Voytkunsky Ya.I., Pershitz R.Ya., Titov I.A. *Spravochnik po teorii korablia* [Handbook of ship theory]. Leningrad, Shipbuilding Publ., 1973. 512 p. (Rus).

20. Aizenshtadt E.B., Gilerovich Yu.M., Gorbunov B.A., Serzhantov V.V. *Grebnye elektricheskie ustanovki: Spravochnik* [Rowing electrical installations. Reference book]. Leningrad, Shipbuilding Publ., 1985. 304 p. (Rus).

21. Baranov L.N., Malishevsky V.E. Results of tests of modernized regulators of power plants of nuclear icebreakers of the «Arktika» type]. *Power installations and equipment of sea-going vessels*, 1990, pp. 74-78. (Rus).

V.A. Yarovenko[1]*, Doctor of Technical Science, Professor,*
P.S. Chernikov[1]*, Senior Instructor,*
[1] Odessa National Maritime University,
34, Mechnikova Str., Odessa, 65007, Ukraine,
phone +380 50 5980683,
e-mail: yarovenko@3g.ua; chernikov@onmu.odessa.ua

V.M. Mikhailov, K.V. Chunikhin

TESTING OF NUMERICAL SOLUTION OF THE PROBLEM OF DETERMINING SOURCES OF MAGNETOSTATIC FIELD IN MAGNETIZED MEDIUM

Purpose. Testing of numerical solution algorithm for integral equation for calculation of plane meridian magnetostatic field source distribution at interfaces of piecewise homogeneous magnetized medium by means of electrostatic analogy. Methodology. The piecewise homogeneous medium consists of three regions with different magnetic permeabilities: the shell of arbitrary meridian section, external unlimited medium outside the shell, and the medium inside the shell. For testing external homogeneous magnetic field effect on spherical shell is considered. The analytical solution of this problem on the basis of electrostatic analogy from the solution of the problem uniform electrostatic field effect on dielectric shell is obtained. We have compared results of numerical solution of integral equation with the data obtained by means of analytical solution at the variation of magnetic permeabilities of regions of medium. Results. Integral equation and the algorithm of its numerical solution for calculation of source field distribution at the boundaries of piecewise homogeneous medium is validated. Testing of integral equations correctness for calculation of fictitious magnetic charges distribution on axisymmetric boundaries of piecewise homogeneous magnetized medium and algorithms of their numerical solutions can be carried out by means of analytical solutions of problems of homogeneous electrostatic field effect analysis on piecewise homogeneous dielectric medium with central symmetry of boundaries – single-layer and multilayer spherical shells. In the case of spherical shell in wide range of values of the parameter λ_k, including close to ± 1, numerical solution of integral equation is stable, and relative error in calculating of fictitious magnetic charges surface density and magnetic field intensity inside the shell is from tenths of a percent up to several percent except for the cases of very small values of these quantities. Originality. The use analytical solutions for problems of calculation of external electrostatic field effect on piecewise homogeneous dielectric bodies for testing integral equations of magnetostatics and algorithms for their numerical solutions. Practical value. The described method of testing integral equations of magnetostatics and their numerical solutions can be used for calculation of magnetic fields of spacecraft control system electromagnets. References 12, tables 2, figures 3.
Key words: **plane meridian magnetostatic field, piecewise homogeneous magnetized medium, integral equation, electrostatic analogy, fictitious magnetic charge.**

Выполнена проверка правильности интегрального уравнения второго рода для расчета распределения источников плоскомеридианного магнитостатического поля на границах раздела кусочно-однородной намагничиваемой среды и его численного решения. Для этого использованы электростатическая аналогия и аналитическое решение задачи о воздействии однородного электростатического поля на сферическую диэлектрическую оболочку в кусочно-однородной диэлектрической среде. Подтверждена правильность интегрального уравнения и его численного решения при помощи аппроксимирующей системы алгебраических уравнений. Сделан анализ влияния магнитных проницаемостей однородных областей среды на распределение фиктивных магнитных зарядов на поверхностях и напряженность магнитного поля внутри сферической оболочки. Библ. 12, табл. 2, рис. 3.
Ключевые слова: **плоскомеридианное магнитостатическое поле, кусочно-однородная намагничиваемая среда, интегральное уравнение, электростатическая аналогия, фиктивный магнитный заряд.**

Introduction. For the calculation of magnetostatic fields in inhomogeneous magnetized media, the use of integral equations of the second kind with respect to the density of fictitious magnetic charges in the volume and on the interfaces of the sections of the medium is effective [1-3]. Integral equations are approximated on a spatial mesh by systems of algebraic equations of high order, which are solved using computers. As in the formulation of integral equations, and with their approximation, errors can be made, connected, for example, with inconsistencies in the directions of vectors, integrating on the elementary part of the computational domain with the singular point of the kernel of the integral equation.

The relevance of this work is due to the need to verify the correctness of the used algorithms and labor-intensive computation procedures using tasks that have analytical (exact) solutions – testing. The number of such solutions in magnetostatics is relatively small. In the known papers, exact solutions of problems of calculating analogous physical fields are not fully utilized, giving preference to more accurate, in the opinion of the authors, numerical methods.

The goal of the work is use of electrostatic analogy for testing the algorithm for the numerical solution of the integral equation for the surface density of fictitious magnetic charges at the interfaces of homogeneous regions of a piecewise homogeneous magnetized medium in the case of a plane meridian magnetostatic field.

Main equations and formulae. Let it be required to test the algorithm for solving a problem for a piecewise homogeneous medium consisting of three homogeneous regions with different constant absolute magnetic permeabilities μ_k ($k = \overline{1,3}$). The shell of an arbitrary meridian section (region 2) divides the unbounded environment into regions 1 and 3, respectively, outside and inside the shell (Fig. 1). In the particular case, region 3 is absent, i.e. there is an axisymmetric body in an unbounded medium, for example, the core of an electromagnet. Using the electrostatic analogy of the problem under consideration [1, 4-6], we represent the scalar potential φ_m of the magnetostatic field due to the magnetic properties of the medium in the form [3, 7, 8]:

$$\varphi_m(Q) = \frac{1}{\pi\mu_0} \int_l \frac{\sigma_m(M) r_M K(k)}{\sqrt{(z_Q - z_M)^2 + (r_Q + r_M)^2}} dl_M \ , \ (1)$$

where $Q, M \in l$ are the point of observation and point

with current coordinates, respectively; μ_0 is the magnetic constant; $\sigma_m(M)$ is the surface density of fictitious magnetic charges; l, dl_M are the total contour of the meridian section of the shell and its element with center at the point M, respectively; $l = l_1 + l_2$, $l_{1,2}$ are the outer and inner parts of the total contour, respectively; $K(k)$ is the complete elliptic integral of the first kind of module k [9];

$$k = 2\sqrt{\frac{r_Q r_M}{(z_Q - z_M)^2 + (r_Q + r_M)^2}}\;;$$

r_Q, r_M and z_Q, z_M are the radial and axial cylindrical coordinates of points Q and M.

The strength of the magnetic field due to the magnetic properties of the medium, and the resulting magnetic field are respectively equal [1]

$$\vec{H}_m = -\operatorname{grad}\varphi_m \qquad (2)$$

and

$$\vec{H} = \vec{H}_0 + \vec{H}_m\,, \qquad (3)$$

where $\vec{H}_0$ is the external magnetic field strength.

Following the idea of the method [1], we note that in order to perform calculations using formulae (1) – (3), it is necessary to find an unknown function $\sigma_m(Q)$, $Q \in l$ by solution of the integral equation

$$\sigma_m(Q) - \frac{\lambda_k}{\pi}\int_l \sigma_m(M)S(Q,M)dl_M = 2\mu_0\lambda_k H_{0n}(Q), \quad (4)$$

where

$$S(Q,M) = \frac{k}{2\sqrt{r_Q^3}}\left\{\sqrt{r_M}\left[K(k) + \frac{1}{k'^2}\times\right.\right.$$

$$\times\left.\left(\frac{r_M + r_Q}{2r_M}k^2 - 1\right)E(k)\right]\cos(\vec{1}_r,\vec{n}_Q) + \qquad (5)$$

$$+ \frac{z_Q - z_M}{2\sqrt{r_M}}\left(\frac{k}{k'}\right)^2 E(k)\cos(\vec{1}_z,\vec{n}_Q)\right\};$$

$\vec{1}_r$, $\vec{1}_z$ are the orts of cylindrical coordinates r and z; $\vec{n}_Q$ is the unit normal to the contour l in the point $Q \in l$; $E(k)$, k' is the complete elliptic integral of the second kind of the module k and the additional module of complete elliptic integrals [9]; $k' = \sqrt{1 - k^2}$;

$$\lambda_k = \frac{\mu_{k+1} - \mu_k}{\mu_{k+1} + \mu_k}, \, k = 1, 2;$$

$H_{0n}(Q)$ is the normal projection of $\vec{H}_0$.
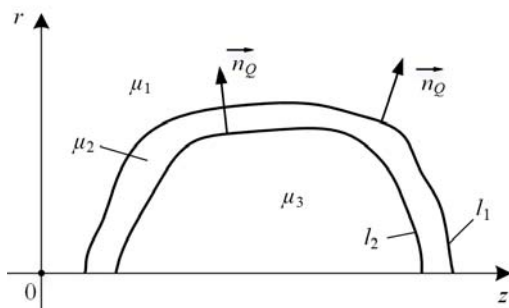

Fig. 1. An axisymmetric shell in a piecewise homogeneous magnetized medium

The particular case of the problem under consideration. For testing, we consider a particular case of the problem described above – the effect of external constant homogeneous magnetic field directed along the axial coordinate z on the spherical shell in a piecewise homogeneous magnetized medium (Fig. 2). The meridian section of this shell is symmetric about the r axis, therefore, for the points M and M' with such symmetry $\sigma_m(M') = -\sigma_m(M)$ and the domain of definition of $\sigma_m(M)$ is halved. We transform the integral equation (4) for this case to the form:

$$\sigma_m(Q) - \frac{\lambda_k}{\pi}\int_l \sigma_m(M)[S(Q,M) - S(Q,M')]dl_M = \qquad (6)$$

$$= 2\mu_0\lambda_k H_0\sin\theta,$$

where θ is the spherical coordinate of elevation angle (Fig. 2).
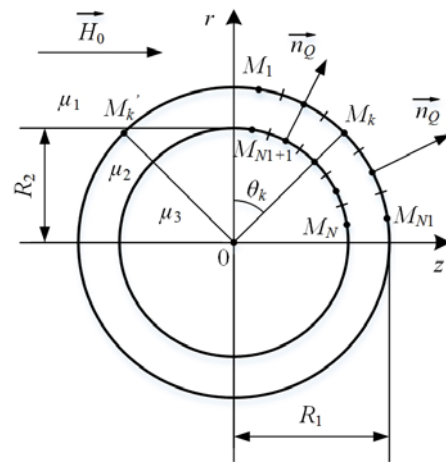
Fig. 2. A spherical shell in a piecewise homogeneous magnetized medium

The total integration contour l in equation (6) consists of two halves l_1 and l_2 symmetric about the r-axis, located in the region $z \geq 0$. The functions $S(Q, M)$ и $S(Q, M')$ entering the kernel of this equation, we determine by formula (5), having adopted in it $\cos(\vec{1}_r,\vec{n}_Q) = \cos\theta$, $\cos(\vec{1}_z,\vec{n}_Q) = \sin\theta$, $z_{M'} = -z_M$, $r_{M'} = r_M$. In addition, it is necessary to take into account the change in the z-coordinates of the symmetric points M' in calculating the modulus k. After solving equation (6), the intensity of the homogeneous magnetic field at an arbitrary point Q inside the shell (region 3) is found using the formula that follows from (1) – (3):

$$H_i(Q) = H_0 + \frac{1}{8\pi\mu_0}\int_l \sigma_m(M)\times$$

$$\times\frac{1}{r_Q\sqrt{r_Q r_M}}(S_1 - S_1')dl_M, \qquad (7)$$

where

$$S_1 = (z_Q - z_M)\frac{k^3}{k'^2}E(k). \qquad (8)$$

The function S_1' in the integrand of the second term (7) is determined by formula (8), replacing in it, as well as in the formula for determining k, the coordinate z_M on $z_{M'}$.

When forming the functions $S(Q, M)$ and $S(Q, M')$ entering the kernels of equations (4), (6), formulas were used to calculate the projections of the plane meridian electrostatic field from [3, 8]. The contour l was divided into N elementary regions with nodal points M_k at their center, which form a spatial mesh, and $k = \overline{1, N_1}$ at $M_k \in l_1$ and $k = \overline{N_1 + 1, N}$ at $M_k \in l_2$ (Fig. 2). Equation (6) was transformed into a system of algebraic equations on a mesh using the quadrature formula of rectangles. The diagonal elements of the $N \times N$ matrix of this system of equations, corresponding to the elementary sections of the contour with the singular point of the kernel of equation (6), were determined by the method described in [10]. The system of algebraic equations was solved by a direct method based on the inversion of the matrix of the left-hand sides and the subsequent multiplication of the inverse matrix by the column vector of the right parts.

Analytical solution of a similar electrostatic problem of the action of an external homogeneous electric field on a dielectric spherical shell is known [11]. Using this solution, we obtain formulas for calculating the distribution of the surface density of fictitious magnetic charges on the boundary surfaces, as well as the intensity of the homogeneous magnetic field H_i inside the magnetized shell:

$$\sigma_m(R_1, \theta) = \mu_0\left(\frac{2}{R_1^3}(B_1 - B_2) + H_0 + A_2\right)\sin\theta ; \quad (9)$$

$$\sigma_m(R_2, \theta) = \mu_0\left(\frac{2B_2}{R_2^3} + H_i - A_2\right)\sin\theta ; \quad (10)$$

$$H_i = -9H_0 \Big/ \left[c_{\mu 1}\left(\frac{\mu_2}{\mu_1} + 2\right) - 2c_{\mu 2}\left(\frac{R_2}{R_1}\right)^3\left(\frac{\mu_2}{\mu_1} - 1\right)\right], (11)$$

where R_1, R_2 are the radii of the boundary surfaces (Fig. 2);

$$B_1 = R_1^3\left[H_0 + A_2\left(1 + c_\mu\left(\frac{R_2}{R_1}\right)^3\right)\right]; \quad B_2 = c_\mu R_2^3 A_2;$$

$$c_{\mu 1} = \mu_3/\mu_2 + 2 ; \quad c_{\mu 2} = 1 - \mu_3/\mu_2 ; \quad c_\mu = c_{\mu 2}/c_{\mu 1} ;$$

$$A_2 = H_i c_{\mu 1}/3 .$$

The values of σ_m and H_i obtained by numerical solution of the integral equation (6) and calculations by the formula (7) will be called approximate, and using (9) – (11) – exact.

Table 1, 2 show the values of $\sigma_m^* = \sigma_m / (\mu_0 H_0)$ and $H_i^* = H_i / H_0$, respectively, and Fig. 3 shows the variation curves for σ_m^* vs θ [0, $\pi/2$] on the boundary surfaces of the shell at $\mu_1 = \mu_0$, $R_2/R_1 = 0.95$ and the variation of $\mu_{2,3}$. The data in columns 1 are approximate, and in columns 2 – exact. For the data given in the numerators of columns 1 of Table 1, it was assumed that $N = 80$, in the denominators – 2160. The curves in Fig. 3 are built from the results of a numerical solution of equation (6) with $N = 2160$.

From Table 1, 2 it follows that in wide ranges of variation of the magnetic permeabilities μ_2 и μ_3 when the step of the spatial mesh is reduced the absolute discrepancies of the exact and approximate values of σ_m^* и H_i^* are of the order of 10^{-3}. In this case, the relative discrepancies vary from 0.1% to several percent, except for very small values of the calculated value.

Table 1

The values of the surface density of fictitious magnetic charges σ_m^* on the surfaces of a spherical shell

The shell surface	θ_k, рад	$\mu_2 = 50\mu_0, \lambda_1 = 0.961$						$\mu_3 = \mu_0$					
		$\mu_3 = 10\mu_0$ $\lambda_2 = -0.667$		$\mu_3 = 100\mu_0$ $\lambda_2 = 0.333$		$\mu_3 = 1000\mu_0$ $\lambda_2 = 0.905$		$\mu_2 = 50\mu_0$ $\lambda_1 = 0.961$ $\lambda_2 = -0.961$		$\mu_2 = 500\mu_0$ $\lambda_1 = 0.996$ $\lambda_2 = -0.996$		$\mu_2 = 2000\mu_0$ $\lambda_1 = 0.999$ $\lambda_2 = -0.999$	
		1	2	1	2	1	2	1	2	1	2	1	2
Outer	0.2945	0.7312 / 0.7483	0.7490	0.8288 / 0.8348	0.8350	0.8457 / 0.8497	0.8498	0.6067 / 0.6370	0.6383	0.7823 / 0.8339	0.8362	0.8048 / 0.8594	0.8617
	0.6086	1.4404 / 1.4739	1.4753	1.6326 / 1.6443	1.6447	1.6658 / 1.6736	1.6739	1.1951 / 1.2548	1.2573	1.5412 / 1.6426	1.6470	1.5855 / 1.6928	1.6974
	0.9228	2.0087 / 2.0553	2.0572	2.2765 / 2.2929	2.2935	2.3229 / 2.3338	2.3342	1.6668 / 1.7497	1.7532	2.1499 / 2.2906	2.2967	2.2117 / 2.3605	2.3670
	1.2369	2.3812 / 2.4355	2.4378	2.6977 / 2.7171	2.7178	2.7525 / 2.7656	2.7660	1.9765 / 2.0735	2.0776	2.5502 / 2.7144	2.7216	2.6236 / 2.7972	2.8049
	1.5510	2.5335 / 2.5774	2.5798	2.8539 / 2.8754	2.8762	2.9033 / 2.9267	2.9272	2.1023 / 2.1943	2.1986	2.7249 / 2.8725	2.8802	2.8047 / 2.9602	2.9683
Inner	0.2945	−0.0507 / −0.0446	−0.0443	0.0103 / 0.0090	0.0089	0.0208 / 0.0182	0.0181	−0.1286 / −0.1134	−0.1128	−0.0441 / −0.0184	−0.0173	−0.0329 / −0.0057	−0.0045
	0.6086	−0.0999 / −0.0878	−0.0872	0.0203 / 0.0177	0.0176	0.0410 / 0.0359	0.0357	−0.2533 / −0.2234	−0.2222	−0.0868 / −0.0362	−0.0340	−0.0647 / −0.0112	−0.0089
	0.9228	−0.1393 / −0.1224	−0.1217	0.0282 / 0.0247	0.0246	0.0572 / 0.0501	0.0497	−0.3530 / −0.3116	−0.3098	−0.1206 / −0.0505	−0.0474	−0.0898 / −0.0156	−0.0124
	1.2369	−0.1646 / −0.1450	−0.1442	0.0334 / 0.0293	0.0291	0.0678 / 0.0593	0.0590	−0.4174 / −0.3692	−0.3671	−0.1410 / −0.0598	−0.0562	−0.1044 / −0.0185	−0.0147
	1.5510	−0.1319 / −0.1534	−0.1526	0.0139 / 0.0310	0.0308	0.0150 / 0.0627	0.0624	−0.3902 / −0.3906	−0.3885	−0.0764 / −0.0632	−0.0595	−0.0349 / −0.0195	−0.0155

Table 2
The values of the magnetic field intensity H_i^*
penetrated inside the spherical shell

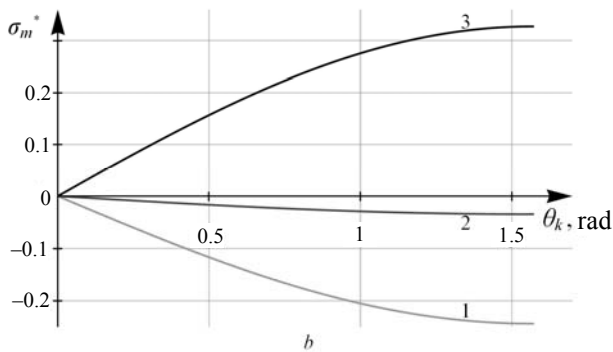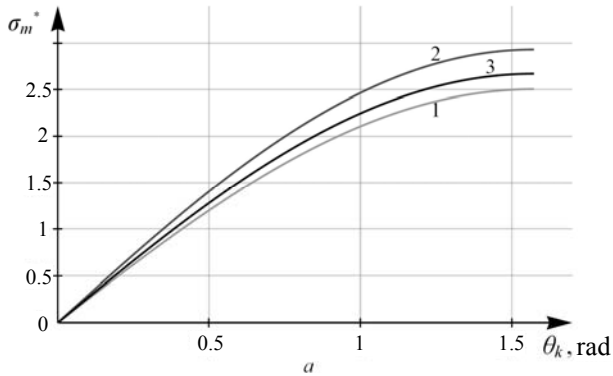| N	$\mu_2 = 50\mu_0$, $\lambda_1 = 0.961$				$\mu_3 = \mu_0$			
	$\mu_3 = 10\mu_0$ $\lambda_2 = -0.667$		$\mu_3 = 100\mu_0$ $\lambda_2 = 0.333$		$\mu_2 = 50\mu_0$ $\lambda_1 = 0.961$ $\lambda_2 = -0.961$		$\mu_2 = 500\mu_0$ $\lambda_1 = 0.996$ $\lambda_2 = -0.996$	
	1	2	1	2	1	2	1	2
80	0.2179		0.0363		0.4502		0.1507	
240	0.2006	0.1908	0.0325	0.0308	0.4159	0.3965	0.0935	0.0596
720	0.1941		0.0314		0.4031		0.0711	
2160	0.1919		0.0310		0.3987		0.0634	

Fig. 3. The distributions of σ_m^* on the outer (*a*) and inner (*b*) surfaces of the spherical shell: for curve 1 $\mu_2 = 100\mu_0$, $\mu_3 = \mu_0$, $2 - \mu_2 = 1000\mu_0$, $\mu_3 = \mu_0$, $3 - \mu_2 = 10\mu_0$, $\mu_3 = 5000\mu_0$

Increasing the accuracy of the numerical solution can also be achieved by using more precise quadrature formulas. From Table 1 and Fig. 3 it follows that the numerical solutions are stable for values of the parameter λ_k close to ± 1. Thus, with the help of an analytical solution of a similar electrostatic problem, the correctness of the compilation of the original integral equation (4) and the algorithm for its numerical solution was confirmed. We note that analytical solutions of problems of the effect of external homogeneous electrostatic field on multilayer dielectric spherical shells are known [12], which can be used to test the algorithm for solving the integral equation in the case of multilayer axisymmetric magnetized shells.

The features of the variation of σ_m^* and H_i^* with the variation of μ_k in the case of a spherical shell. The values of σ_m^* on the calculated part of the contour of the outer surface of the spherical shell ($z > 0$) are positive for all μ_k and vary insignificantly for large μ_2. On the calculated part of the contour of the inner surface of the

shell for $\mu_3 < \mu_2$ ($\lambda_2 < 0$), the values of σ_m^* are negative, and for $\mu_3 > \mu_2$ ($\lambda_2 > 0$) are positive (Table 1). Naturally, on the part of the contour symmetric about the *r*-axis, the signs of σ_m^* are opposite.

At large $\mu_2 \geq 100\mu_0$, the shell shields region 3, which results in small values of H_i^* and σ_m^*. An increase in μ_3 leads to an additional decrease in H_i^* (Table 2).

The described features of the changes of σ_m^* and H_i^* can also be useful in the analysis of the magnetostatic field in the case of axisymmetric shells and solid bodies of a different shape.

Conclusions.

1. Testing the correctness of integral equations for calculating the distribution of fictitious magnetic charges on the axisymmetric boundaries of a piecewise homogeneous magnetized medium and the algorithms of their numerical solutions can be carried out using analytical solutions of problems of analyzing the action of homogeneous electrostatic field on a piecewise homogeneous dielectric medium with a central symmetry of boundaries – single-layer and multilayer spherical shells.

2. In the case of a spherical shell in a wide range of values of the parameter λ_k including those close to ± 1, the numerical solution of the integral equation is stable, and when reducing the mesh step, the relative error in calculating the surface density of fictitious magnetic charges and the magnetic field strength inside the shell is from the tenths percentages to a few percent, except for very small values of these values.

REFERENCES
1. Grinberg G.A. *Izbrannye voprosy matematicheskoi teorii elektricheskikh i magnitnykh iavlenii* [Selected questions of mathematical theory of electric and magnetic phenomena]. Moscow-Leningrad, Acad. of Sci. USSR Publ., 1948. 730 p. (Rus).
2. Tozoni O.V., Maergoiz I.D. *Raschet trekhmernykh elektromagnitnykh polei* [Calculation of three-dimensional electromagnetic fields]. Kiev, Tekhnika Publ., 1974. 352 p. (Rus).
3. Mikhailov V.M. *Raschet elektricheskikh i magnitnykh polei s pomoshch'iu integral'nykh i integrodifferentsial'nykh uravnenii* [Calculation of electric and magnetic fields using integral and integrodifferential equations]. Kiev, EMC HE Publ., 1988. 60 p. (Rus).
4. Polivanov K.M. *Teoreticheskie osnovy elektrotekhniki, ch. 3. Teoriia elektromagnitnogo polia* [Theoretical foundations of electrical engineering, Part 3. Theory of electromagnetic field]. Moscow, Energiya Publ., 1969. 352 p. (Rus).
5. Simonyi K. *Teoreticheskaya elektrotekhnika* [Theoretical Electrical Engineering]. Moscow, Mir Publ., 1964. 775 p. (Rus).
6. Mikhailov V.M., Chunikhin K.V. On electrostatic analogy of magnetostatic field in inhomogeneous magnetized medium. *Electrical engineering & electromechanics*, 2017, no.5, pp. 38-40. (Rus). **doi: 10.20998/2074-272X.2017.5.05.**
7. Kolechitskii E.S. *Raschet elektricheskikh polei ustroistv vysokogo napriazheniia* [Calculation of electric fields of high voltage devices]. Moscow, Energoatomizdat Publ., 1983. 168 p. (Rus).
8. Jungerman J.A. Fourth-order uniform electric field form two charged rings. *Review of Scientific Instruments*, 1984, vol.55, no.9, pp. 1479-1482. **doi: 10.1063/1.1137962.**
9. Ianke E., Emde F., Lesh F. *Spetsial'nye funktsii* [Special functions]. Moscow, Nauka Publ., 1977. 344 p. (Rus).

10. Bondina N.N., Volchkov Iu.I., Konovalov O.Ia. *Modelirovanie elektromagnitnykh polei. Laboratornyi praktikum* [Modeling of electromagnetic fields. Laboratory practice]. Kharkov, NTU «KhPI» Publ., 2007. 168 p. (Rus).

11. Boyko N.I., Bondina N.N., Donets S.E., Levchenko E.V., Mikhailov V.M. Polarization of spherical shells and electric field distribution in biological cell. *Tekhnichna elektrodynamika. Tem. vypusk «Problemy suchasnoyi elektrotekhniky»*, 2002, part 6, pp. 13-19. (Rus).

12. Boyko N.I., Bondina N.N., Levchenko E.V., Mikhailov V.M. Modeling the effect of electric field on objects having a multilayer structure. *Electronic modeling*, 2002, vol.24, no.1, pp. 70-82. (Rus).

V.M. Mikhailov[1], Doctor of Technical Science, Professor,
K.V. Chunikhin[2], Postgraduate Student,
[1] National Technical University «Kharkiv Polytechnic Institute»,
2, Kyrpychova Str., Kharkiv, 61002, Ukraine,
phone +380 57 7076052,
e-mail: valery.m.mikhailov@gmail.com
[2] State Institution «Institute of Technical Problems of Magnetism of the NAS of Ukraine»,
19, Industrialna Str., Kharkiv, 61106, Ukraine,
phone +380 57 2992162,
e-mail: kvchunikhin@gmail.com

J. Ganji

NUMERICAL SIMULATION OF THERMAL BEHAVIOR AND OPTIMIZATION OF a-Si/a-Si/C-Si/a-Si/A-Si HIT SOLAR CELL AT HIGH TEMPERATURES

Purpose. Silicon heterostructure solar cells, particularly Heterojunction with Intrinsic Thin layer (HIT) cells, are of recommended silicon cells in recent years that are simply fabricated at low processing temperature and have high optical and temperature stability and better efficiency than homojunction solar cells. In this paper, at first a relatively accurate computational model is suggested for more precise calculation of the thermal behavior of such cells. In this model, the thermal dependency of many parameters such as mobility, thermal velocity of carriers, band gap, Urbach energy of band tails, electron affinity, relative permittivity, and effective density of states in the valence and conduction bands are considered for all semiconductor layers. The thermal behavior of HIT solar cells in the range of 25-75 °C is studied by using of this model. The effect of the thickness of different layers of HIT cell on its external parameters has been investigated in this temperature range, and finally the optimal thicknesses of HIT solar cell layers to use in wide temperature range are proposed. References 20, tables 4, figures 5.
Key words: **heterojunction with intrinsic thin layer cell, high temperature, thermal behavior.**

Цель. Кремниевые гетероструктурные солнечные элементы, в частности гетеропереходы с ячейками внутреннего тонкого слоя (HIT), в последнее время рекомендуются для использования в качестве кремниевых элементов, поскольку они легко изготавливаются при низкой температуре обработки и имеют высокую оптическую и температурную стабильность, а также более высокий к.п.д., чем солнечные элементы на основе гомоперехода. В настоящей работе впервые предлагается относительно точная вычислительная модель для более точного расчета теплового поведения таких ячеек. В этой модели для всех слоев полупроводника рассматривается температурная зависимость многих параметров, таких как подвижность, тепловая скорость носителей, граница зоны, энергия Урбаха хвостов зоны, сродство электронов, относительная диэлектрическая проницаемость и эффективная плотность состояний в валентной зоне и в зоне проводимости. С использованием данной модели исследуется тепловое поведение HIT солнечных элементов в диапазоне 25-75 °C. В данном диапазоне температур исследовано влияние толщины различных слоев HIT ячейки на ее внешние параметры и в результате предложена оптимальная толщина слоев HIT солнечных элементов для использования в широком диапазоне температур. Библ. 20, табл. 4, рис. 5.
Ключевые слова: **гетеропереходы с ячейками внутреннего тонкого слоя, высокая температура, тепловое поведение.**

Introduction. The Heterojunction with Intrinsic Thin layer (HIT) solar cells are one of the most promising affordable photovoltaic systems to achieve clean energy. Low process temperature and, as a result, more economic modules [1], high open circuit voltage due to higher bandgap of amorphous silicon [2], good efficiency due to low recombination of carriers in the interface of amorphous and crystalline silicon [3], good stability and low temperature dependence [1] are of advantages of these solar cells.

Because of developments during recent years, the efficiency of HIT solar cells has been continuously increased and the efficiency of 25.6 % recorded for these cells by Panasonic company in 2014 [4]. This performance upgrades happen due to research on various subjects like the effect of Indium-Tin-Oxide (ITO) layer on the behavior of the cell [5], the impact of front contact work function [6], the effect of surface texturing of crystalline silicon (c-Si) wafer [7], the role of Fermi state of doped hydrogenated amorphous silicon (a-Si:H) layers and band offsets [8], and the effect of intrinsic layer on the cell function [9].

Dwivedi et al. (2012) optimized different structures of HIT cells through the thickness change of a-Si:H(n) and a-Si:H(i) front layers and c-Si wafer. The highest efficiency achieved in that study was 27.2 % for a cell with ITO/a-Si:H(n)/ a-Si:H(i)/c-Si(p)/a-Si:H(i)/ a-Si:H(p)/metal structure [10]. Jian et al. (2015) reached theoretic efficiency of 27.2 % using simulation of HIT solar cell with TCO/a-Si:H(n)/ a-Si:H(i)/ c-Si(p)/ a-Si:H(p)/Ag structure by varying of thickness and doping of layers [11].

While the modeling of a massive amount of performed research has been done in Standard Test Conditions (STC) and 25 °C, a limited number of them conducted in hot weather conditions like tropical zones in which the cell temperature rises to over to 70 °C or in the concentrated modules which the cell temperature rises up to 100 °C [12]. Taguchi et al. (2008) reported an efficiency decrease with increase of temperature and reduction of efficiency drop with increasing thickness of a-Si:H(i) layer through examination of temperature dependence of external parameters of the Ag/TCO/a-Si:H(p)/a-Si:H(i)/c-Si(n)/a-Si:H(i)/a-Si:H(n)/TCO/Ag cell [13]. In 2013, Vishkasougheh et al. studied changes of external parameters of TCO/a-Si:H(n)/μc-Si:H(i)/c-Si(p)/a-Si:H(p) cell influenced by increase of temperature via simulation [14]. Agarwal and Doosan (2015) performed similar study and investigated the effect of the thickness of a-Si:H(i) layer on the cell's dark saturation current density [15]. Sachenko et al. (2016) studied temperature dependence of a cell with Ag/ITO/aSi:H(p)/aSi:H(i)/a-SiC/c-Si(n)/a-SiC/aSi:H(i)/aSi:H(n)/ITO/Ag structure. The research results showed increase of short circuit current, decrease of open circuit voltage, reduction of fill factor and decrease of cell efficiency in the range of 300-400 K [16]. Dramatic and abnormal increase of mobility of amorphous silicon layer with the temperature has been neglected in most solar cell simulation packages in spite of its important impact on the temperature behavior of solar cell.

The goal of the paper is to provide a relative accurate simulation of HIT solar cells, in which, almost all temperature-dependent layer parameters (the most comprehensive set of parameters in the literature) have been considered. By these simulations, the thermal

coefficient of studied HIT cells is obtained, resulting to optimize the thickness of the HIT layers to gain the least temperature dependency of efficiency.

Simulation tools and method. In the current study, the simulation core is AFORS-HET software, a tool for one-dimensional of homojunction and heterojunction solar cells that has necessary facilities to observe the effect of parallel changes of various structural and environmental parameters on the final characteristics of the solar cell [17, 18]. This software uses defect-pool model [19] to explain amorphous and microcrystalline layers which is used in various types of heterojunction cells including HIT cells, with the ability to define and edit the exponential, Gaussian, linear, and point defect shapes for each layer. Moreover, in order to increase flexibility and performance of simulation, a program was developed for defining a set of parametric structures with the capability of changing the temperature in the desired range and called GDMAT. This program can define layers with regular parametric changes, and through combination of them, it can create structures useable by AFORS-HET software, and also can prepare all outputs of AFORS-HET in the suitable form to plot.

The cell under investigation is based on a p-type silicon wafer as the absorber layer. The emitter has been constituted from a-Si:H(n) and a-Si:H(i) thin film layers, respectively. Two ITO layers have placed in the back and front of cell which act as both anti-reflection layer and transparent electrode. Back Surface Field (BSF) has been formed from a-Si:H(n) and a-Si:H(i) layers in the back of the cell. Fig. 1 shows the structure of defined cell and its bands diagrams.
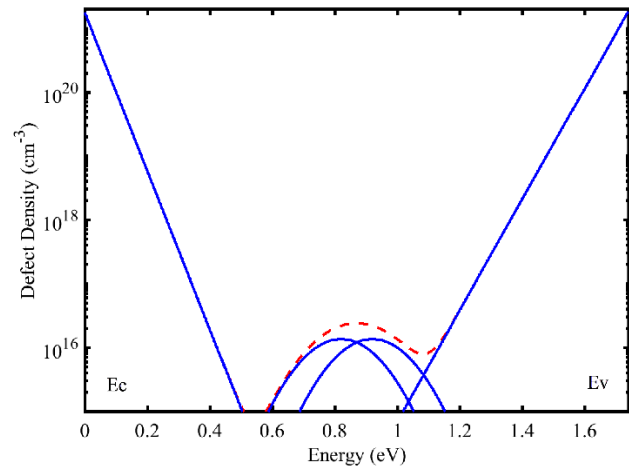

Fig. 1. The defect density diagram of a-Si:H (i) layers used in the simulation. The dashed-line curve represents the total defect density

The defect-pool model has been used to describe non-crystalline layers in which structural defects were defined with exponential band tails and Gaussian–shaped dangling bonds in the midgap. Fig. 2 shows the defect density curves of the a-Si:H (i) layer which is used in the structure.
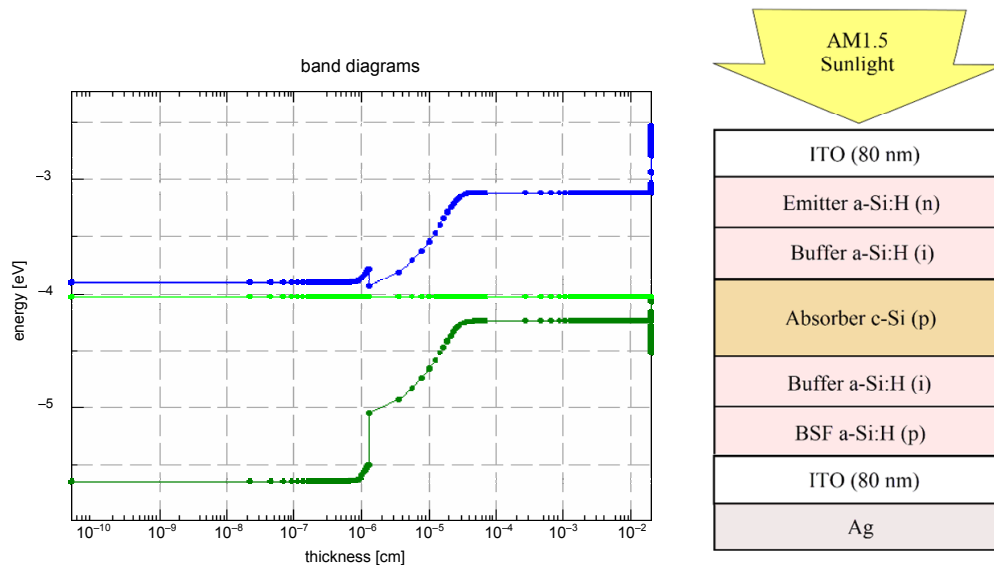

Fig. 2. The structure of simulated HIT cell (*a*). Band diagram of the cell at the thermal equilibrium (*b*)

Table 1 contains the temperature-independent parameters of semiconductor layers in the simulation. The temperature-dependent parameters have been inferred from reference [20] and summarized in Table 2. This parameter values have been briefly recorded only at end temperatures of 300 and 350 K. However, in our simulations, the temperature changing step is considered to be 5.

In the proposed model, parameters that have linear temperature dependence are interpolated with a general relation

$$y(T) = y(298) + [y(348) - y(298)]\left(\frac{T - 298}{348 - 298}\right)$$

at intermediate temperatures. Other parameters, which have exponential dependency, interpolated with relation

$$y(T) = y(298)\left[\frac{y(348)}{y(298)}\right]^{\left(\frac{T - 298}{348 - 298}\right)}$$

in which $y(298)$ and $y(348)$ are the values of considered parameters at 298 K and 348 K that shown in Table 2.

Table 1

Temperature-independent parameters of HIT layers in the current study

Parameter	Unit	a-Si(n)	a-Si(i)	a-Si(p)	c-Si(p)
Conduction Band Tail					
Electron Thermal Cross Section	cm^2	7E-16	7E-16	7E-16	
Hole Thermal Cross Section	cm^2	7E-16	7E-16	7E-16	
Total Trap Density	cm^{-3}	1.36E20	6.4E19	1.6E21	
Specific Trap Density	cm^{-3}	2E21	1.8E21	2E21	
Valence Band Tail					
Electron Thermal Cross Section	cm^2	7E-16	7E-16	7E-16	
Hole Thermal Cross Section	cm^2	7E-16	7E-16	7E-16	
Total Trap Density	cm^{-3}	1.88E20	9.4E19	2.4E20	
Specific Trap Density	cm^{-3}	2E21	1.88E21	2E21	
Dangling Band Acceptor					
Electron Thermal Cross Section	cm^2	3E-15	3E-15	3E-15	
Hole Thermal Cross Section	cm^2	3E-14	3E-14	3E-14	
Total Trap Density	cm^{-3}	6.9E19	5E15	6.89E19	
Specific Trap Density	cm^{-3}	1.3E20	1.38E16	1.3E20	
Energy of Distribution	eV	0.6	0.82	1.2	
Characteristic Energy	eV	0.21	0.144	0.21	
Dangling Band Donor					Point Defect
Electron Thermal Cross Section	cm^2	3E-14	3E-14	3E-14	1E-14
Hole Thermal Cross Section	cm^2	3E-15	3E-15	3E-15	1E-14
Total Trap Density	cm^{-3}	6.89E19	5E15	6.89E19	1E10
Specific Trap Density	cm^{-3}	1.3E20	1.38E16	1.3E20	1E10
Energy of Distribution	eV	0.7	0.92	1.1	0.56
Characteristic Energy	eV	0.21	0.144	0.21	

Table 2

Temperature-dependent parameters of HIT layers at 25 °C and 75 °C

Parameter	Unit	c-Si @348K	c-Si @298K	n,i,p a-Si:H @348K	n,i,p a-Si:H @298K	Sequence Type
Dielectric Constant	-	12.05	11.9	12.05	11.9	Linear
Electron Affinity	eV	34.17	4.05	3.83	3.9	Linear
Mobility Bandgap (E$_g$)	eV	1.106	1.12	1.726	1.74	Linear
Optical Bandgap (E$_{g,opt}$)	eV	1.006	1.02	1.626	1.64	Linear
Effective Conduction Band Density of States	cm^{-3}	3.57E+19	2.8E+19	1.24E+20	1E+20	Exponential
Effective Valence Band Density of States	cm^{-3}	1.39E+19	1.04E+19	1.24E+20	1E+20	Exponential
Electron Mobility	cm^2/Vs	708	1040	20	5	Exponential
Hole Mobility	cm^2/Vs	280	412	4	1	Exponential
Electron Thermal Velocity	cm/s	1.08E+07	1E+07	1.08E+07	1E+07	Exponential
Hole Thermal Velocity	cm/s	1.08E+07	1E+07	1.08E+07	1E+07	Exponential
Urbach Energy of Conduction Band Tail	meV	-	-	78,38,92	68,35,80	Linear
Urbach Energy of Valence Band Tail	meV	-	-	108,57,138	94,50,120	Linear

Simulation steps and results. A 1000 W/cm^2 AM1.5 light was applied to the front surface of studied HIT cell, and simulation process started using AFORS-HET. Due to the large number of parameters to be swept, GDMAT tool was employed to define various cell structures frequently and run AFORS-HET to simulate them as a batch process.

In the first step, the effect of the thickness of layers on the thermal behavior of cell was investigated through change of a-Si(n) layer thickness from 4 nm to 12 nm and observed that increase of the thickness of this layer decreases efficiency of cell, but improves its thermal coefficients (TC). With selection of the minimum value of the range, second phase of simulation was performed through change of a-Si:H(i) layer thickness from 3 nm to 9 nm that obtained same result as the previous one. Therefore, 3 nm thickness was recorded for this layer. Fig. 3 shows the fill factor (FF) and efficiency diagram of cell after this step.

In the next step, wafer thickness was swept from 100 μm to 250 μm. According to the Fig. 3, this increase leads to reduction of open circuit voltage (V_{oc}) and enhancement of short circuit current density (J_{sc}) and a peak was observed in efficiency at 200 μm. Thus, 200 μm was recorded as optimum thickness of wafer.

Decrease of V_{oc} can be considered due increase of recombination of carrier in thicker layer and increasing of J_{sc} is as a result of enhancement of photon absorption rate because of its prolonged pathway in the absorber layer. Results are shown in Fig. 4.

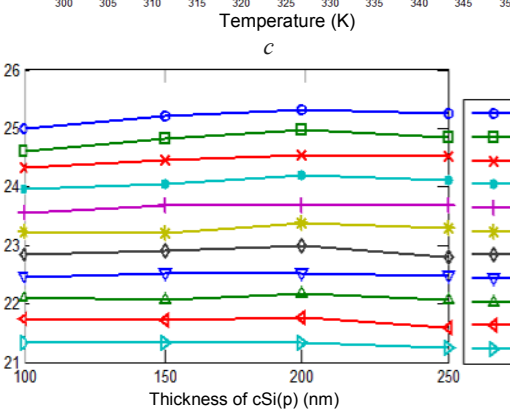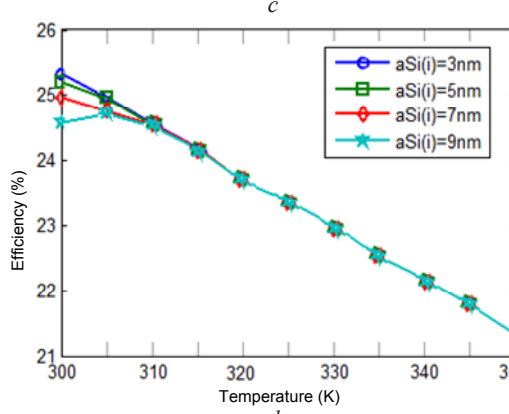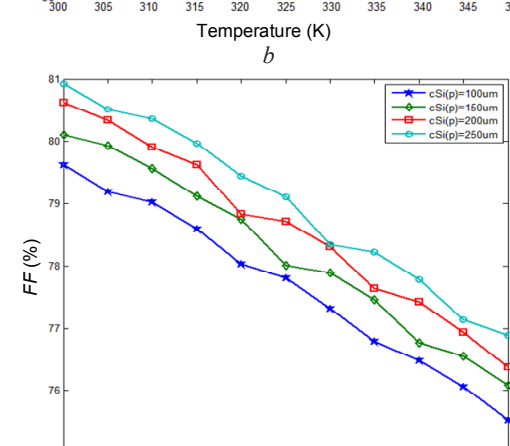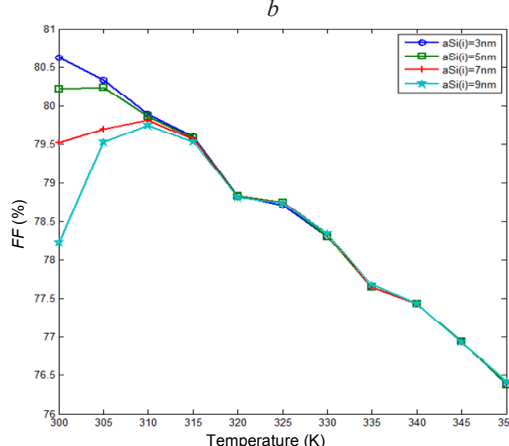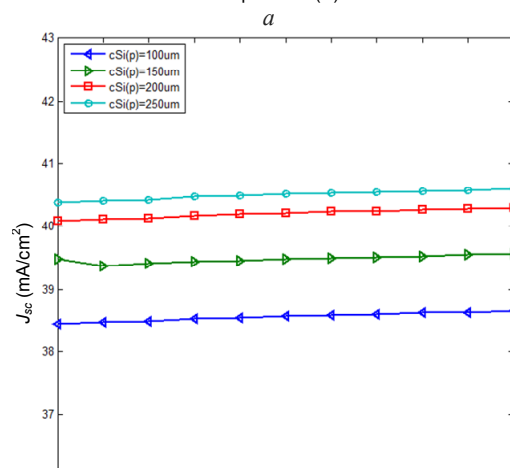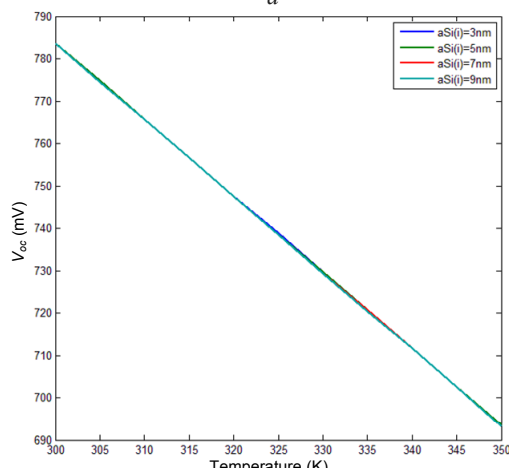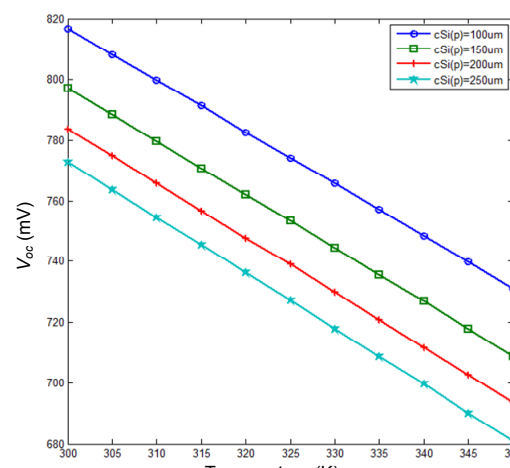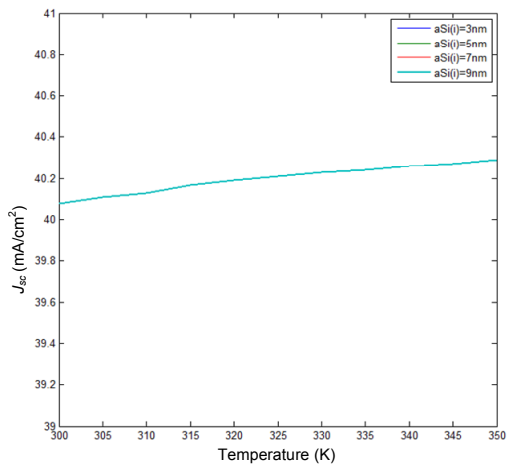Fig. 3. The effect of front a-Si:H(i) layer thickness on the temperature dependency of external parameters of cell

Fig. 4. The effect of c-Si(p) layer thickness on the temperature dependency of V_{oc} (*a*), J_{sc} (*b*), FF (*c*) and efficiency (*d*)

In the fourth step, the thickness of a-Si(i) layer was changed from 3 nm to 9 nm. It was observed that this change has no impact on the J_{sc} and V_{oc} but decreases fill factor and consequently efficiency at temperature near to 300 K. Therefore, value of 3 nm was selected as optimal thickness.

In the fifth and final step, the thickness of a-Si(p) layer was swept from 4 nm to 12 nm but observed no significant change. Summary of all steps is given in Table 3. Furthermore, optimum thickness of layers is included in Table 4 for which open circuit voltage of 783 mV, short circuit current density of 40.08 mA/cm^2, fill factor of 80.6 % and efficiency of 25.4 % have been obtained. In this condition, thermal coefficient of efficiency (TC$_\eta$) and mean efficiency in the range of 25-75 °C are calculated – 0.32 %/°C and 23.38 %, respectively. Current-voltage (I-V) curve of designed cell under light at several temperatures has shown in Fig. 5.
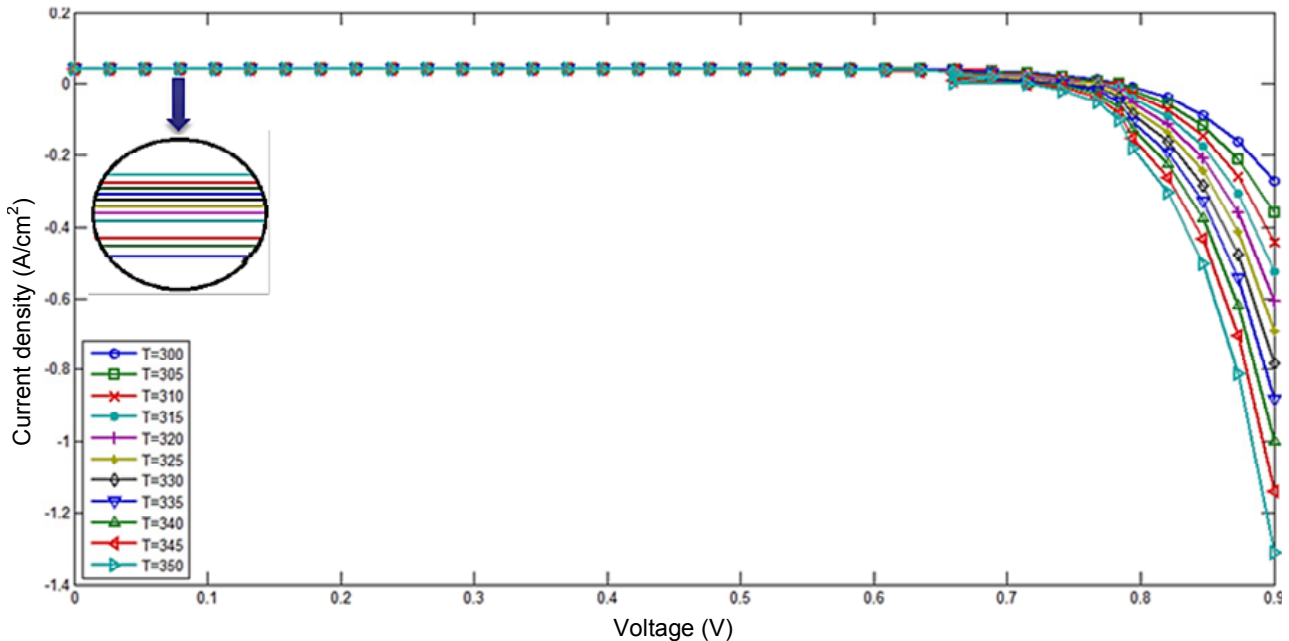

Fig. 5. The I-V Diagram of desired HIT cell in various temperatures under AM1.5 Sun light

Table 3

Summarized results of simulation steps

Order	Parameter	Initial (nm)	Variation (nm)	T (K)	V_{oc} (mV)	J_{SC} (mA/cm^2)	FF (%)	Efficiency (%)	TCη (%/°C) Mean η (%)
1	a-Si:H (n) Thickness		4-12	298	802-760	39.1-36.8	80.1-80.2	25.1-22.4	-0.39, -0.3
				348	677-675	39.3-36.9	76-76.1	20.2-19.0	22.65, 20.7
2	Front a-Si:H (i) Thickness	3	3-9	298	803-763	39.08-38.45	80.1-75.9	25.1-22.2	-0.39, -0.23
				348	673-673	39.29-38.8	76.4-75.3	20.2-19.7	22.65, 21.85
3	c-Si (p) Thickness	150	100-250	298	817-772	38.4-40.3	79.6-81	25-25.4-25.35	-0.29, -0.32
				348	731-681	38.6-40.5	75.5-76.9	21.35-21.25	23.18, 23.3
4	Back a-Si:H(i) Thickness	3	3-9	298	783-783	40.08-40.08	80.6-78.2	25.4-24.55	-0.32, -0.26
				348	693-693	42.09-42.09	76.4-76.4	21.35-21.35	21.38, 22.95
5	BSF a-Si:H(p) Thickness	10	4-12	298	**783**-783	**40.08**-40.08	**80.6**-80.6	**25.4**-25.4	-0.32, -0.31
				348	694-694	42.09-42.09	76.4-76.4	21.35-21.35	**23.38**, 23.32

Table 4

Optimized values of layers thickness'

Layer	Thickness (nm)
a-Si:H (n)	4
a-Si:H (i)	3
c-Si (p)	200
a-Si:H (i)	3
a-Si:H (p)	4

Conclusions. Considering a fairly complete collection of structural dependencies of layers on the temperature, a model was codified to describe the thermal behavior of HIT cell with ITO/a-Si(n)/a-Si(i)/c-Si(p)/a-Si(i)/a-Si(p)/ITO/Ag structure, and simulated the thermal variations of external parameters of cell by using of the model. Moreover, the effect of variation of the thickness of layers on the cell's thermal behavior was investigated.

The following results can be inferred from performed simulations:

1. In the studied cell, increase of temperature causes linear reduction of open circuit voltage, minor increase in short circuit current, less fill factor, and less efficiency.

2. Though increase of the thickness of a-Si:H(n) layer within a few nanometers slightly improves fill factor and thermal coefficient of efficiency but it causes significant decrease of open circuit voltage, short circuit current and output power. Therefore, because of the technological limitations and to avoid the occurrence of quantum effects, it can be chosen in the range of 3-4 nm.

3. Increase of the thickness of a-Si:H(i) layers, located at both sides of the wafer, within a few nanometers improves TC$_\eta$ since this layer participates in the absorption process and increase in the absorption

compensates part of the short-circuit current drop at high temperature. On the other hand, this advantage is disregarded because of significant reduction of open circuit voltage, fill factor and efficiency and thus, thickness is limited to about 3-4 nm.

4. Increase of the c-Si(p) wafer thickness, enhances absorption and short circuit current and on the other hand, reduces the recombination rate and consequently open circuit voltage. These two contradictory effects make this quantity optimal in a certain number. In this research, the optimum amount of wafer thickness has been calculated to be 200 μm. Moreover, this layer as the only crystalline layer, is also the only layer that increase of its thickness doesn't improve thermal coefficient.

5. The changes in the thickness of a-Si(p) BSF layer within a few nanometers does not show a significant effect on the thermal behavior of cell.

6. Selecting the optimized thicknesses for layers, theoretical efficiency at 25 °C and mean efficiency in the range of 25-75 °C have been obtained 25.4 % and 23.38 %, respectively.

REFERENCES

1. Datta A., Chatterjee P. *Computer Modeling of Heterojunction with Intrinsic Thin Layer «HIT» Solar Cells: Sensitivity Issues and Insights Gained, in Solar Cells-Thin-Film Technologies.* InTech Publ., 2011.
2. Pascual Sánchez D. *Crystalline silicon Heterojunction solar cells.* Universitat Politècnica de Catalunya, 2015.
3. Jäger K. et al. *Solar energy fundamentals, technology and systems.* Delft University of technology, 2014. 78 p.
4. Masuko K., Shigematsu M., Hashiguchi T., Fujishima D., Kai M., Yoshimura N., Yamaguchi T., Ichihashi Y., Mishima T., Matsubara N., Yamanishi T., Takahama T., Taguchi M., Maruyama E., Okamoto S. Achievement of More Than 25% Conversion Efficiency With Crystalline Silicon Heterojunction Solar Cell. *IEEE Journal of Photovoltaics*, 2014, vol.4, no.6, pp. 1433-1435. **doi: 10.1109/JPHOTOV.2014.2352151.**
5. Zhang D., Tavakoliyaraki A., Wu Y., R.A.C.M.M. van Swaaij, Zeman M. Influence of ITO deposition and post annealing on HIT solar cell structures. *Energy Procedia*, 2011, vol.8, p. 207-213. **doi: 10.1016/j.egypro.2011.06.125.**
6. Lee S., Tark S.J., Kim C.S., Jeong D.Y., Lee J.C., Kim W.M., Kim D. Influence of front contact work function on silicon heterojunction solar cell performance. *Current Applied Physics*, 2013, vol.13, no.5, pp. 836-840. **doi: 10.1016/j.cap.2012.12.013.**
7. Li G., Zhou Y., Liu F. Influence of textured c-Si surface morphology on the interfacial properties of heterojunction silicon solar cells. *Journal of Non-Crystalline Solids*, 2012, vol.358, no.17, pp. 2223-2226. **doi: 10.1016/j.jnoncrysol.2011.12.106.**
8. Shen L., Meng F., Liu Z. Roles of the Fermi level of doped a-Si: H and band offsets at a-Si: H/c-Si interfaces in n-type HIT solar cells. *Solar Energy*, 2013, vol.97, p. 168-175. **doi: 10.1016/j.solener.2013.08.028.**
9. Hayashi Y., Li D., Ogura A., Ohshita Y. Role of i-aSi:H layers in aSi:H/cSi heterojunction solar cells. *IEEE Journal of Photovoltaics*, 2013, vol.3, no.4, pp. 1149-1155. **doi: 10.1109/JPHOTOV.2013.2274616.**
10. Dwivedi N., Kumar S., Bisht A., Patel K., Sudhakar S. Simulation approach for optimization of device structure and thickness of HIT solar cells to achieve ~27 % efficiency. *Solar energy*, 2013. vol.88: pp. 31-41. **doi: 10.1016/j.solener.2012.11.008.**
11. Jian L., Shihua H., Lü H. Simulation of a high-efficiency silicon-based heterojunction solar cell. *Journal of Semiconductors*, 2015, vol.36, no.4, p. 044010. **doi: 10.1088/1674-4926/36/4/044010.**
12. Wanlass M.W., Coutts T.J., Ward J.S., Emery K.A., Gessert T.A., Osterwald C.R. Advanced high-efficiency concentrator tandem solar cells. *The Conference Record of the Twenty-Second IEEE Photovoltaic Specialists Conference*, 1991. **doi: 10.1109/PVSC.1991.169179.**
13. Taguchi M., Maruyama E., Tanaka M. Temperature dependence of amorphous/crystalline silicon heterojunction solar cells. *Japanese Journal of Applied Physics*, 2008, vol.47, no.2, pp. 814-818. **doi: 10.1143/JJAP.47.814.**
14. Vishkasougheh M.H., Tunaboylu B. Simulation of high efficiency silicon solar cells with a hetero-junction microcrystalline intrinsic thin layer. *Energy conversion and management*, 2013, vol.72, pp. 141-146. **doi: 10.1016/j.enconman.2012.10.025.**
15. Agarwal M., Dusane R.O. Temperature dependent analysis of heterojunction silicon solar cells: Role of intrinsic layer thickness. *2015 IEEE 42nd Photovoltaic Specialist Conference (PVSC)*, Jun. 2015. **doi: 10.1109/PVSC.2015.7356058.**
16. Sachenko A.V., Kryuchenko Y.V., Kostylyov V.P., Bobyl A.V., Terukov E.I., Abolmasov S.N., Abramov A.S., Andronikov D.A., Shvarts M.Z., Sokolovskyi I.O., Evstigneev M. Temperature dependence of photoconversion efficiency in silicon heterojunction solar cells: Theory vs experiment. *Journal of Applied Physics*, 2016, vol.119, no.22, p. 225702. **doi: 10.1063/1.4953384.**
17. Varache R., Leendertz C., Gueunier-Farret M.E., Haschke J., Muñoz D., Korte L. Investigation of selective junctions using a newly developed tunnel current model for solar cell applications. *Solar Energy Materials and Solar Cells*, 2015, vol.141, pp. 14-23. **doi: 10.1016/j.solmat.2015.05.014.**
18. Altermatt P.P. Models for numerical device simulations of crystalline silicon solar cells - a review. *Journal of Computational Electronics*, 2011, vol.10, no.3, pp. 314-330. **doi: 10.1007/s10825-011-0367-6.**
19. Powell M.J., Deane S.C. Improved defect-pool model for charged defects in amorphous silicon. *Physical Review B*, 1993, vol.48, no.15, pp. 10815-10827. **doi: 10.1103/physrevb.48.10815.**
20. Ganji J., Kosarian A., Kaabi H. Numerical modeling of thermal behavior and structural optimization of a-Si:H solar cells at high temperatures. *Journal of Computational Electronics*, 2016, vol.15, no.4, pp. 1541-1553. **doi: 10.1007/s10825-016-0913-3.**

Jabbar Ganji, Ph.D.,
Department of Electrical Engineering, Faculty of Engineering,
Shahid Chamran University of Ahvaz, Ahvaz, Iran,
e-mail: j.ganji@mhriau.ac.ir

Y.L. Anokhin, V.O. Brzhezytskyi, Ya.O. Haran, I.M. Masliuchenko, O.P. Protsenko, Ye.O. Trotsenko

APPLICATION OF HIGH VOLTAGE DIVIDERS FOR POWER QUALITY INDICES MEASUREMENT

Introduction. Determination of power quality indices in high-voltage power grids allows to find the reasons for the deterioration of the power quality. The relevant national and International Standards for power quality contain relevant norms of quality indices and requirements for their accuracy measurement. Problem. The most complicated part in the process of measuring the power quality indices at high voltage is the selection of the corresponding high-voltage scale voltage converters. Therefore, comparing the requirements of IEC 61000-4-30 to high voltage scale voltage converters is an important task. Goal. Analysis of the International Standard IEC 61000-4-30 requirements feasibility for measuring the indices of power quality in high-voltage electrical networks using different types of high-voltage scale voltage converters. Methodology. Comparison of the requirements of IEC 61000-4-30 Standard to high-voltage scale voltage converters, when measuring power quality indices, with the characteristics of high voltage electromagnetic transformers used in Ukraine, and with promising developments of high-voltage converters of other types. Results. It is shown in the study that in order to fulfill some of the requirements for class A of IEC 61000-4-30, the characteristics of electromagnetic voltage transformers should be determined in the substation conditions using mobile calibration high-voltage laboratories. To meet all the requirements for Class A IEC 61000-4-30, it is recommended to use broadband high-voltage dividers of resistive-capacitive type. Originality. In study it is shown firstly that all the requirements of the IEC 61000-4-30 Standard for high-voltage scale voltage converters can be performed on the basis of the use of broadband resistive-capacitive damped voltage dividers. Practical value. Expositions of specific types of resistive-capacitive high-voltage dividers are presented, their parameters are confirmed by the results of state metrological certification. References 17, figures 11.
Key words: **power quality indices, high voltage, electromagnetic transformers, voltage dividers**.

Цель. Анализ выполнимости требований международного стандарта IEC 61000-4-30 при измерениях показателей качества электроэнергии в высоковольтных электрических сетях с использованием различных типов высоковольтных масштабных преобразователей напряжения. Методика. Сравнение требований стандарта IEC 61000-4-30 к высоковольтным масштабным преобразователям напряжения, при измерении показателей качества электроэнергии, с характеристиками электромагнитных трансформаторов высокого напряжения, применяемых в Украине, и с перспективными разработками масштабных преобразователей высокого напряжения других типов. Результаты. Показано, что для выполнения части требований по классу А IEC 61000-4-30 характеристики электромагнитных трансформаторов напряжения должны быть определены в условиях подстанции с помощью мобильных поверочных высоковольтных лабораторий. Для выполнения всех требований по классу А IEC 61000-4-30 рекомендуется использование высоковольтных широкополосных делителей напряжения емкостно-омического типа. Научная новизна. Впервые показано, что все требования стандарта IEC 61000-4-30 к высоковольтным масштабным преобразователям напряжения могут быть выполнены на основе использования широкополосных емкостно-омических демпфированных делителей напряжения. Практическая значимость. Представлены экспозиции конкретных типов емкостно-омических делителей высокого напряжения, их параметры, подтвержденные результатами государственной метрологической аттестации. Библ. 17, рис. 11.
Ключевые слова: **показатели качества электроэнергии, высокое напряжение, электромагнитные трансформаторы, делители напряжения**.

Introduction. The transition to free market economy in the electric power industry of Ukraine in accordance with the recently adopted the Electricity Market Law, as well as the prospect of joining the Ukrainian energy system to the European Union energy system, posed a serious problem of increasing the domestic power quality (PQ) level to the requirements of European Standards. At the same time, this problem is technically divided into two parts: first, it is necessary to create means for measuring power quality indices and perform their metrological certification, and then, using these tools, to improve the power quality at specific power facilities. To reduce the loss of time, it is advisable to perform both tasks in parallel.

It should be noted that, in fact, the power quality at a particular site (at a certain point of connection) is determined only by the voltage characteristics [1], but in order to detect sources of deterioration in the power quality, it is also necessary to have information on the characteristics of the current consumed by the loads connected to this point [2].

In accordance with [1], the power quality indices are normalized for low-voltage networks (for example, 220/380 V), as well as for voltage classes of 6-20 kV; 35 kV; 110-330 kV and separately 500-750 kV.

In accordance with [3], the power quality indices (PQI) are normalized for voltages up to 150 kV, inclusive, while according to [4] - up to 220 kV. For higher voltage classes, the power quality indices are determined based on the contractual relationship between the supplier and the consumer of electricity.

For low-voltage electrical networks in a number of countries (Israel, Germany, Japan and others), firms produce certified (by the international organizations) means of measuring the power quality indices (MM PQI) adapted to certain power quality standards, with a range of input nominal voltages, for example 100/√3 V, 100 V, 110 V, 220 V, 230 V, and so on. [5]. For high-voltage electrical networks, these devices are connected to the outputs of high-voltage measuring transducers [2], among which the most requested are high-voltage measuring electromagnetic voltage transformers and voltage dividers

(current converters intended for the purposes of power quality measurements are not reviewed in this paper).

The feature of the Standards, regulating methods and means of measuring power quality indices [2, 6] is that they establish general requirements for such facilities, and the one who conducts the measurement of power quality indices should select the type of MM PQI. In the existing high-voltage electrical networks, the measurement of PQI is carried out using high-voltage transformers involved in substation circuits (of НОМ, ЗНОМ, НАМИ, НКФ, НОГ types) that do not meet all requirements for large-scale voltage converters for measuring power quality [2, 6]. As a result, they get knowingly «improved» power quality indices that are not true. Unfortunately, this problem has not been systematically studied in the domestic literature.

In foreign publications attention is paid to the problem of measuring power quality in high-voltage systems. For example, in [7] it is noted that if earlier the main problem was power supply interruptions, nowadays the main thing is the quality of electric power, the registration of the power quality indices, while the use of voltage dividers is the preferred one in the role of high-voltage converters.

The paper [8] describes the circuit and design of the divider for a 400 kV network, which, although called a «resistive» voltage divider, is in fact is a resistive-capacitive voltage divider with parallel connection of R, C- elements. Its purpose is to measure harmonics in a 400 kV network. The height of the divider is 3.78 m, the maximum diameter of anti-corona ring is 2.0 m.

The work [9] compares the results of measurements of voltage harmonics in a 400 kV network using a divider and voltage transformers. As a result of the measurement it is shown that the total ratio of higher harmonic components of voltage for the resistive divider and the electromagnetic voltage transformer practically coincide, while for the capacitive voltage transformer dramatically different results are obtained.

In [10], the development of a pulse resistive voltage divider is described for recording a lightning impulse up to 500 kV. The height of the divider is 1.84 m with maximum diameter of the anti-corona ring of 0.96 m. The resistance of the high-voltage arm of the voltage divider is 10.3 kΩ.

Low-voltage experimental studies of the frequency characteristics of a pulsed resistive voltage divider with nominal voltage of up to 1000 kV and a resistive-capacitive divider with nominal voltage of up to 200 kV have been carried out in [11]. Measurements were also made of the reaction time of the dividers by the stepped pulse method, while the first divider reaction time was 47 ns and the second one was 120 ns.

According to the results of the review of foreign publications, it can be concluded that high-voltage dividers are considered as a promising alternative to electromagnetic voltage transformers when measuring power quality in high-voltage systems. In this case, resistive-capacitive voltage dividers have similar dynamic characteristics with impulse resistive dividers.

The goal of the paper. On the basis of the analysis of the requirements for means of measuring the power

quality parameters [2, 6], to justify the necessity of using voltage dividers in high-voltage systems for measuring these indices, and also to generalize the results of studies of high-voltage broadband voltage dividers made at the Department of High Voltage Engineering and Electrophysics of the National Technical University of Ukraine «Igor Sikorsky Kyiv Polytechnic Institute» (HVEE of NTUU «KPI»). At the same time, high voltages will be understood as voltages whose nominal values are 110 kV, 150 kV [3] and 220 kV [4]. The requirements for the measurement parameters will be assigned to class A, since it is a question of the correspondence of the real power quality to the requirements of International Standards [2, 3, 6].

Below we will analyze only those indices that affect the use of high-voltage measuring transducers in determining the power quality in high-voltage networks.

The root-mean-square value of the voltage in accordance with 5.2.1 [2] must take into account the harmonics, interharmonics, telecontrol signals existing in the electrical network. Its measurement uncertainty in accordance with 5.2.2 [2] should not exceed ±0.1 % of the voltage U_{din} (declared input voltage) in the range of 10-150 % of U_{din}, with the range of disturbances according to Table C.1 [2] is 10-200 % of U_{din}.

Electromagnetic voltage transformers (types НКФ – 110, НКФ – 150, НКФ – 220, НОГ 110 – 220) used in most cases at electric stations and substations in accordance with the Interstate Standard [12] are capable of withstanding in the course of 1s 200 % overvoltage of frequency of 50 Hz, but the guaranteed area of their accuracy class (0.2; 0.5) corresponds only to the range of 80-120 % of the nominal voltage.

Concerning the permissible uncertainty in the measurement of ±0.1 % U_{din}, it should be noted that the Department of HVEE of NTUU «KPI» created a mobile calibration laboratory [13] of classes 6-110 kV (Fig. 1) the use of which makes it possible to determine the tolerance of voltage transformers in substations at their actual load, and thus, taking into account the introduction of the corresponding adjustment, to reduce the uncertainty of U_{din} measurement to ±0.03 %.

Fig. 1. A mobile calibration laboratory for classes 6-110 kV

However, taking into account the fact that «electromagnetic voltage transducers of transformer type have frequency and transient characteristics that are applicable for operation at frequencies up to 1 kHz» (cited from [2]), their use for measurements of higher harmonics and interharmonics with order $n > 20$ (and, moreover, the

telecontrol signals) are unreasonable. Thus, high voltage electromagnetic voltage transformers used in electric stations and substations do not meet the requirements for determining the rms voltage value in class A [2].

Voltage of harmonics and interharmonics. In accordance with the above definition [2], electromagnetic voltage transformers are not suitable for an adequate scale conversion of harmonics and interharmonics, with an order that exceeds 20.

The voltage asymmetry is determined by the main voltage harmonics in three-phase networks [2, 6], which are transformed with sufficient accuracy by electromagnetic voltage transformers (subject to corrections, determined using a mobile calibration laboratory [13]). Existing devices for measuring power quality indices [5], as a rule, determine the line voltages with sufficient accuracy when using the results of measuring phase voltages.

The above power quality indices are related to quasistatic modes of three-phase systems. Other indices, such as **flicker, voltage dips and rises, short-term voltage interruptions, telecontrol signals in electrical networks, voltage of transients and fast transients** refer to the dynamic modes in three-phase electrical systems whose scale voltage transformation is not provided by existing high-voltage electromagnetic voltage transformers, since the characteristic value of their time constant is 10-400 ms [14]. In this connection, it can be concluded that a full-scale measurement of power quality indices in high-voltage systems should be carried out using high-voltage measuring dividers. Using the electromagnetic voltage transformers used in high-voltage electrical networks, it is possible to measure the asymmetry of voltages as well as voltage interruptions.

The choice of types of high-voltage dividers for the purposes of measuring the power quality indices has its own specific solution. The Standard [2] states that: «... capacitive dividers may have frequency and phase characteristics, used to operate at frequencies up to hundreds of kilohertz or higher; but in many applications a resonant circuit is added, which makes the frequency response of the capacitive divider inapplicable for measurements at any frequency other than resonant.» The latter refers to the so-called capacitive high-voltage transformers. Therefore, in the above-mentioned publication [9] it is noted that the results of measuring the total coefficient of higher harmonic components for voltage of 400 kV using a capacitive voltage transformer are unacceptable. Similar measurement results for a resistive voltage divider and an electromagnetic voltage transformer are similar [9]. This is because the harmonics with the order $n \leq 20$ are satisfactorily transformed [2, 6] by electromagnetic voltage transformers, which explains the agreement of the results of measuring the total coefficient of higher harmonic voltage components for the «resistive» divider and the electromagnetic voltage transformer [9].

At the same time, as noted above, the «resistive» voltage divider [9] is actually (according to the circuit) a resistive-capacitive voltage divider with a parallel-series connection of R, C- elements. «Resistive voltage dividers can have frequency and phase characteristics that allow

operation at frequencies up to hundreds of kilohertz. However, they can introduce other problems, for example, the capacitive nature of the load of the measuring device can affect the frequency and phase characteristics of the voltage divider» (quoted by [2, 6]). With respect to the above provisions [2, 6], it should be noted that the only correct solution for the type of high-voltage divider for PQI measurements in high-voltage systems is the combination of a resistive and capacitive divider, i.e. the use of a resistive-capacitive voltage divider, as in [9] (the authors' development on this issue will be considered below). This allows, in principle, to ensure the constant amplitude-frequency response (AFR) of the voltage divider from zero to the high-frequency region with «zero» values of the phase-frequency response of the divider in the same frequency range. This solution also makes it possible to remove the question of the effect of the capacitive load of the measuring device on the coefficient of conversion of the voltage divider.

Developments of the Department for High Voltage Engineering and Electrophysics of the NTUU «Igor Sikorsky Kyiv Polytechnic Institute» in the field of research of high-voltage dividers. The task of developing a high voltage divider for the measurement of the PQI is to create a so-called wideband voltage divider whose dividing ratio would be constant (within ±0.1 % of the nominal value) up to frequency of 10 MHz. Although resistive-capacitive dividers with a parallel-series connection of R, C- elements are principally designed for this, however, a number of complex phenomena arise in their implementation.

1. The instability of the amplitude-frequency response caused by the nonidentity of the values of the R, C-elements of the high-voltage arm of the voltage divider (VD). If we present the circuit of a high-voltage resistive-capacitive voltage divider (of a mixed type) in the form (Fig. 2), it can be shown [15] that for the amplitude-frequency response (AFR) and the phase-frequency response (PFR) of the divider, the following expressions can be obtained:

$$AFR = \frac{1}{K} A^*,$$

$$A^* = \sqrt{\frac{1+\gamma^2}{\left(1 + \frac{K-1}{K}f\right)^2 + \gamma^2\left(1 + \frac{K-1}{K}\delta\right)^2}}, \quad (1)$$

$$PFR = \text{arctg}\left(\frac{(\delta - f)\gamma}{f + \frac{K}{K-1} + \gamma^2\left(\delta + \frac{K}{K-1}\right)}\right), \quad (2)$$

where K is the nominal value of the division coefficient of the VD, at which the parameters of the low-voltage arm are determined in the form

$$r = \frac{nR_0}{K-1}, \quad c = \frac{C_0}{n}(K-1), \quad (3)$$

$$R_0 = \frac{1}{n}\sum_{i=1}^{n} R_i, \quad C_0 = \frac{1}{n}\sum_{i=1}^{n} C_i, \quad \gamma = \omega R_0 C_0$$

(the dimensionless angular frequency parameter), and the parameters $f = \dfrac{1}{n}\sum\limits_{i=1}^{n} D_i$, $\delta = \dfrac{1}{n}\sum\limits_{i=1}^{n} G_i$ take into account the functions of the nonidentity of its elements averaged over the elements of the high-voltage arm $\alpha_i = \dfrac{C_i - C_0}{C_0}$,

$\beta_i = \dfrac{R_i - R_0}{R_0}$ in the form of the following formulae

$$D_i = \frac{\gamma^2\left(T_i + \gamma^2 S_i\right)}{\left(1+\gamma^2\right)\cdot\left[1+\gamma^2\left(1+\beta_i\right)^2\left(1+\alpha_i\right)^2\right]}, \quad (4)$$

$$G_i = \frac{\beta_i + 2\alpha_i\beta_i + \alpha_i\beta_i^2 + \gamma^2\left(P_i + \gamma^2 Q_i\right)}{\left(1+\gamma^2\right)\cdot\left[1+\gamma^2\left(1+\beta_i\right)^2\left(1+\alpha_i\right)^2\right]}, \quad (5)$$

and here

$$Q_i = \alpha_i^2\left(1+\alpha_i\right)\left(1+\beta_i\right)^2,$$

$$T_i = -\left(\begin{array}{c}6\alpha_i\beta_i + 6\alpha_i\beta_i^2 + 2\alpha_i\beta_i^3 + \alpha_i^2 + 3\alpha_i^2\beta_i + \\ + 3\alpha_i^2\beta_i^2 + \alpha_i^2\beta_i^3 + 3\beta_i^2 + \beta_i^3\end{array}\right),$$

$$S_i = 2\alpha_i\beta_i + 4\alpha_i\beta_i^2 + 2\alpha_i\beta_i^3 + 3\alpha_i^2 + 7\alpha_i^2\beta_i + \alpha_i^2\beta_i^3 +$$
$$+ 5\alpha_i^2\beta_i^2 + 2\alpha_i^3 + 4\alpha_i^3\beta_i + 2\alpha_i^3\beta_i^2 + \beta_i^2 + \beta_i^3$$

$$P_i = -\left(\begin{array}{c}6\alpha_i\beta_i + 9\alpha_i\beta_i^2 + 4\alpha_i\beta_i^3 + 3\alpha_i^2 + 8\alpha_i^2\beta_i + \\ + 7\alpha_i^2\beta_i^2 + 2\alpha_i^2\beta_i^3 + \alpha_i^3 + 2\alpha_i^3\beta_i + \\ + \alpha_i^3\beta_i^2 + 3\beta_i^2 + 2\beta_i^3\end{array}\right).$$
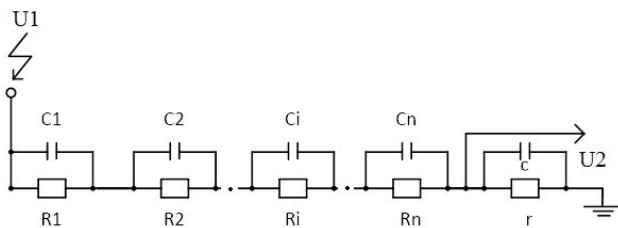

Fig. 2. The circuit of a high-voltage divider of mixed type according to [15] (here R_i, C_i are the values of resistances and capacitances of the elements of the high-voltage divider arm, r, c are the values of the elements of its low-voltage arm)

It should be noted that expressions (1)-(5) were obtained [15] in the general case, without assuming the smallness of the parameters α_i, β_i, γ. In the absence of non-identity of R_i, C_i elements, i.e. $R_1 = R_2 = \ldots = R_i = \ldots = R_n$, $C_1 = C_2 = \ldots = C_i = \ldots = C_n$, $\alpha_i \equiv 0$, $\beta_i \equiv 0$ and from (4), (5) we obtain $f \equiv 0$, $\delta \equiv 0$ and, accordingly, $A^* = 1$ and $PFR \equiv 0$.

In [16], the work [15] was further developed taking into account the assumption of the «triangular» law of the probability distribution of the deviation of the parameters α_i, β_i from the zero value, see Fig. 3*).

Below, according to the data of [16], the dependence of the deviation of the normalized value of the amplitude-frequency response $(A^* - 1)\cdot 100$ %, in % and PFR (′) in angular minutes for mixed type VD on the dimensionless frequency parameter $lg(\gamma)$ is presented (see Fig. 4, 5).
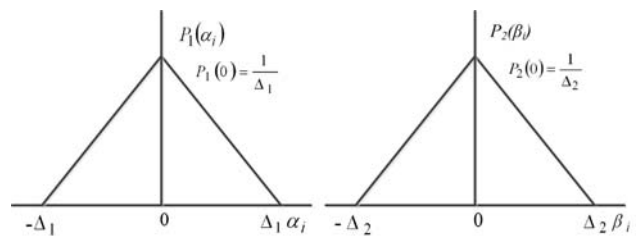

Fig. 3. The graph of the «triangular» probability distribution $P_1(\alpha_i)$ and $P_2(\beta_i)$

Note: Since the number of elements of the high-voltage arm of the VD is usually $n >> 100$, it is advisable to switch to the use of the distribution functions $P_1(\alpha_i)$, $P_2(\beta_i)$
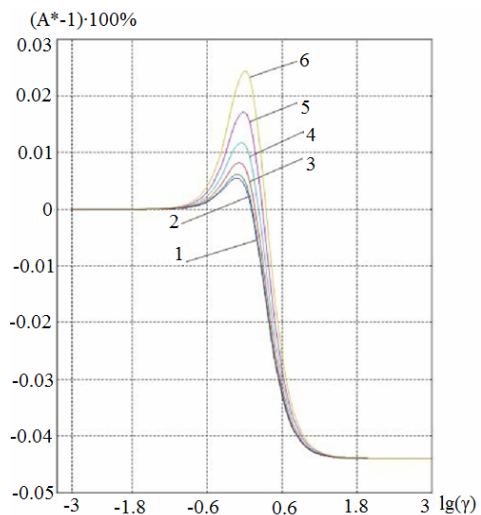

Fig. 4. Dependence $(A^*-1)\cdot 100$ % for mixed type VD depending on the dimensionless frequency parameter γ for fixed $\Delta_1 = 0.05$ when the value of Δ_2 is changed in the range: 0.00...0.05, here the designation 1 corresponds to $\Delta_2 = 0.00$; the designation 2 corresponds to $\Delta_2 = 0.01$; the designation 3 corresponds to $\Delta_2 = 0.02$; the designation 4 corresponds to $\Delta_2 = 0.03$; the designation 5 corresponds to $\Delta_2 = 0.04$; the designation 6 corresponds to $\Delta_2 = 0.05$
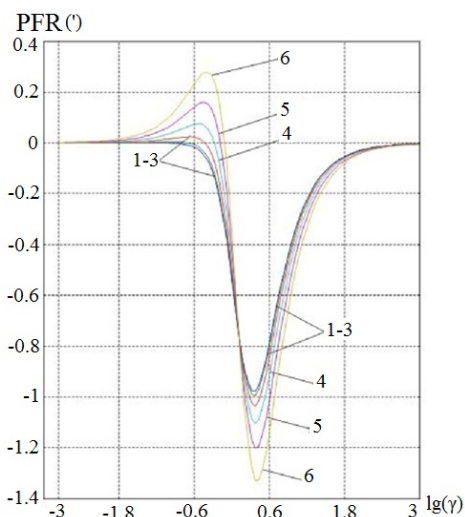

Fig. 5. Phase-frequency response for mixed type VD depending on the dimensionless frequency parameter γ for fixed $\Delta_1 = 0.05$ when the value of Δ_2 is changed in the range: 0.00...0.05, here the designation 1 corresponds to $\Delta_2 = 0.00$; the designation 2 corresponds to $\Delta_2 = 0.01$; the designation 3 corresponds to $\Delta_2 = 0.02$; the designation 4 corresponds to $\Delta_2 = 0.03$; the designation 5 corresponds to $\Delta_2 = 0.04$; the designation 6 corresponds to $\Delta_2 = 0.05$

From the data in Fig. 4, 5 and [16], we can draw conclusions:

• the influence of non-identity – the «scatter» of the values of the elements (R_i, C_i) of the high-voltage arm of a mixed VD leads to instability of its frequency characteristics;

• the influence of the boundaries of the «spread» of the active elements of the high-voltage arm up to $\Delta_2 = 0.01$ (±1 %) is negligible compared to the effect of a «spread» of capacitive elements with a level $\Delta_1 = 0.05$ (±5 %). The «spread» of the capacitance values of the high-voltage arm of the VD (±5 %) is still acceptable, since it leads to a range of AFR oscillations of up to 0.05 %;

• the influence of the «spread» of capacitive elements on the frequency characteristics is proportional to the square of the values of its boundaries ($\sim\Delta_1^2$);

• PFR instability of mixed type VD caused by the nonidentity of its R_i, C_i elements of the high-voltage arm up to $\Delta_1 = 0.05$; $\Delta_2 = 0.01$, is negligible.

2. Dependence of the scale factor of the high-voltage divider on its input voltage level.

As already stated above, the tolerance of high voltage electromagnetic voltage transformers is normalized for a range of 80-120 % of their rated voltage [13], which is due to nonlinear magnetization of their magnetic circuit. For high-voltage dividers of mixed type, this dependence can be significantly weakened when the potential distribution along the internal circuit of the lumped R, C- elements of the high-voltage arm (Fig. 2) is consistent with the distribution of the potential in the spatial-field circuit of the divider due to the electric field between its high-voltage and grounded electrodes.

Fig. 6, 7 show the dependences of the tolerance of the high-voltage divider of the «high-voltage meter of direct and alternating voltage BBH – 0,8 – 100M», developed by the Department of HVEE of NTUU «KPI» (Fig. 8) according to its state metrological attestation at the State Enterprise «Ukrmetrteststandart» (Kyiv) processed in [17]. The tolerance of the high-voltage divider was determined as $\Delta = \dfrac{K_n - K_m}{K_n} \cdot 100\%$, where

K_n is the nominal value of the divider dividing ratio (in this case $K_n = 10000$), and K_m is its actual value, determined by the ratio of the rms values of the input and output voltages, averaged over the results of 10 independent observations. The load of the divider was on the active resistance (10±0.5) MΩ, on capacitance (10±5) pF.

The difference between the dependences 1 and 2 of the tolerance of high-voltage dividers in Fig. 5, 6 is explained by the appearance in the first case of a microcoron on its R, C- elements, which leads to leakage of the current of the high-voltage arm with an increase in the input voltage of the divider, while the actual value of its division factor K_m increases. Thus, it is obligatory to reconcile the distribution of the potentials of the circuit of lumped R, C-elements and the spatial-field circuit of the divider. In this case, the range of oscillations in the tolerance of the voltage divider in the range 10 – 100 kV will be an acceptable value of ±0.1 %.
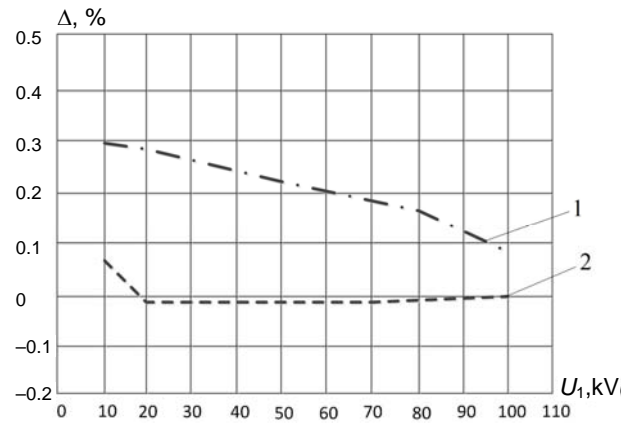
Fig. 6. The experimental dependence of the tolerance of the same voltage dividers of the high voltage meter BBH – 0,8 – 100M in the range of the input DC voltage variation 10...100 kV: 1 – design of the high-voltage arm with a uniform arrangement of R, C- elements in the height of the divider; 2 – design of a high-voltage arm with a coordinated distribution of potentials of the internal circuit with lumped R, C- elements and the spatial-field circuit of the divider.
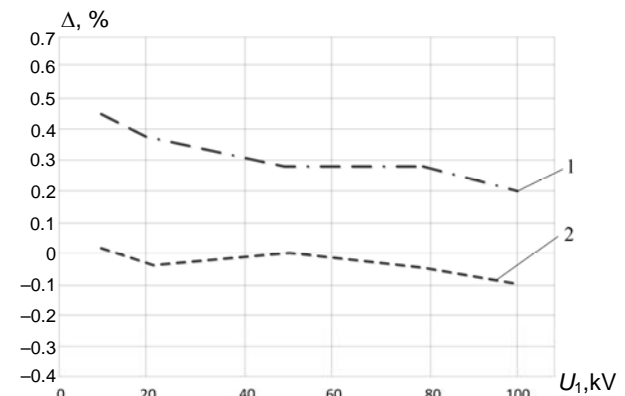
Fig. 7. The experimental dependence of the tolerance of the same voltage dividers of the high voltage meter BBH-0,8-100M in the range of the input AC voltage variation 10...100 kV (frequency 50 Hz): 1 – design of the high-voltage arm with a uniform arrangement of R, C- elements in the height of the divider; 2 – design of a high-voltage arm with a coordinated distribution of potentials of the internal circuit with lumped R, C- elements and the spatial-field circuit of the divider.

Fig. 8. General view of the set for measuring high voltage BBH-0,8-100M in the composition of a high-voltage arm, a low-voltage arm, a specialized digital voltmeter and connecting cables. The separate design of the low-voltage divider arm is due to the possibility of its adjustment and switching for the high-voltage measuring ranges 0.8-10 kV and 10-100 kV

3. Features of broadband voltage dividers for the high frequency region, as well as for measuring pulse voltages. In this case, the low-voltage divider arm should have a low-inductance design and must be built into the overall design of the divider. In addition, it is necessary to use damping resistances in the circuits of the high-voltage and low-voltage divider arms, as well as the matching resistances in the cable connection of the oscilloscope, Fig. 9.

Fig. 9. External view of a high-voltage broadband voltage divider ВДН -75 designed to measure DC, AC and pulse voltages of 110 kV class (the nominal value of the division factor is K_n = 10000)

Fig. 10 shows an oscillogram of the output voltage of ВДН – 75 when a step voltage pulse is applied to its input.
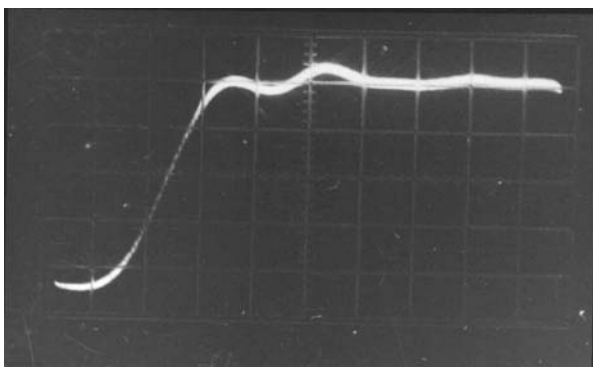

Fig. 10. Output voltage oscillogram of a high-voltage wideband divider ВДН – 75 when a step voltage pulse is applied to its input (vertical scale is 10 mV per division, horizontal scale is 20 ns per division)

Processing of this oscillogram according to the requirements of the Standard IEC 60060-2 determines the response time of the ВДН – 75 divider $\tau_r \sim 25 \cdot 10^{-9}$ s, which allows it to be used for measurement of switching, lightning, and chopped lightning voltage impulses.

Fig. 11 is a general view of the voltage divider of the 220 kV class for measuring the power quality indices in 220 kV electric networks developed by the Department of HVEE of NTUU «KPI» under a contract with State Enterprise «NEC Ukrenergo».

To test high-voltage voltage dividers in substation conditions, it is advisable to develop the capabilities of high-voltage mobile calibration laboratories [13] for

metrological certification, both transformers and voltage dividers with their actual load.

Fig. 11. A high-voltage divider class 220 kV for measuring the power quality indices (outdoor design)

Conclusions.

1. In accordance with the requirements of the International Standard IEC 61000-4-30, electromagnetic voltage transformers used in substations can be used to measure such high-voltage power quality indices as voltage asymmetry and voltage interruption (tripping), provided they are metrologically certified on site using mobile calibration laboratories.

2. According to the results of the research, among the large-scale high-voltage converters of various types, high-voltage broadband voltage dividers of resistive-capacitive type have the most acceptable characteristics of the accuracy of high voltage conversion in accordance with class A of the International Standard IEC 61000-4-30.

3. Among the main scientific problems of the development of the theory and practice of high-voltage broadband voltage dividers, one should note the influence of the non-identical parameters of the R, C- elements of the high-voltage arm, the matching of the distribution of the potentials of the circuit of lumped R, C- elements and the spatial-field circuit of the divider, as well as the optimal damping of its circuit connections.

4. It is necessary to create high-voltage mobile calibration laboratories for metrological certification of both transformers and voltage dividers with their actual load at the substations.

REFERENCES
1. GOST 13109-97. Elektricheskaya energiya. Sovmestimost' tehnicheskih sredstv elektromagnitnaya. Normy kachestva elektricheskoi energii v sistemah elektrosnabzheniya obschego naznacheniya [State Standard 13109-97. Electric Energy. Electromagnetic compatibility of technical equipment. Power quality limits to general purpose power systems]. Moscow, IPK Publishing house of standards Publ., 1999. 35 p. (Rus).
2. DSTU IEC 61000-4-30:2010. Elektromahnitna sumisnist'. Chastyna 4-30. Metody vyprobuvannya ta vymiryuvannya. Vymiryuvannya pokaznykiv yakosti elektroenerhiyi [State Standard DSTU IEC 61000-4-30:2010. Electromagnetic compatibility (EMC). Part 4-30. Testing and measurement

techniques. Power quality measurement methods]. Kyiv, DP «UkrNDNC» Publ., 2016. 49 p. (Ukr).

3. DSTU EN 50160:2014. Kharakterystyky napruhy elektropostachannya v elektrychnykh merezhakh zahal'noyi pryznachenosti [State Standard DSTU EN 50160:2014. Voltage characteristics of electricity supplied by public electricity networks]. Kyiv, Ministry of Economic Development of Ukraine Publ., 2014. 27 p. (Ukr).

4. GOST 32144-2013. Elektricheskaia energiia. Sovmestimost' tekhnicheskikh sredstv elektromagnitnaia. Normy kachestva elektricheskoi energii v sistemakh elektrosnabzheniia obshchego naznacheniia [State Standard 32144-2013. Electric Energy. Electromagnetic compatibility of technical equipment. Power quality limits to general purpose power systems]. Moscow, Standartinform Publ., 2014. 16 p. (Rus).

5. ELSPEC LTD. *G4K. Fixed Power Quality Analyzer. User & Installation Guide.* 2013. Available at: http://elspec-ltd.com/download/g4400-user-guide/ (accessed 26 August 2017).

6. IEC 61000-4-30:2015. *Electromagnetic compatibility (EMC). Part 4-30. Testing and measurement techniques. Power quality measurement methods*.

7. Muscas C. Power quality monitoring in modern electric distribution systems. *IEEE Instrumentation & Measurement Magazine*, 2010, vol.13, no.5, pp. 19-27. **doi: 10.1109/MIM.2010.5585070.**

8. Pawelek R., Wasiak I. Comparative measurements of voltage harmonics in transmission grid of 400 kV. *16th International Conference on Harmonics and Quality of Power (ICHQP)*, 2014, pp. 606-610. **doi: 10.1109/ICHQP.2014.6842763.**

9. Blajszczak G. Resistive voltage divider for higher harmonics measurement in 400 kV network. *11th International Conference on Electrical Power Quality and Utilisation*, 2011, pp. 1-4. **doi: 10.1109/EPQU.2011.6128953.**

10. Harada T., Wakimoto T., Sato S., Saeki M. Development of Japan's national standard class 500 kV lightning impulse voltage divider. *IEEE Power Engineering Society Winter Meeting. Conference Proceedings (Cat. No.00CH37077)*, 2000, vol.3, pp. 1564-1568. **doi: 10.1109/PESW.2000.847575**.

11. Prochazka R., Hlavacek J., Knenicky M., Mahmoud R. Determination of frequency characteristics of high voltage dividers in frequency domain. *17th International Scientific Conference on Electric Power Engineering (EPE)*, 2016, pp. 1-4. **doi: 10.1109/EPE.2016.7521821.**

12. GOST 1516.3. Elektrooborudovanie peremennogo toka na napriazhenii ot 1 do 750 kV. Trebovaniia k elektricheskoi prochnosti izoliatsii [State Standard 1516.3. Electrical equipment of alternating current for voltage from 1 to 750 kV. Requirements for dielectric strength of insulation]. Moscow, IPK Publishing house of standards Publ., 1998. 50 p. (Rus).

13. Brzhezytskyi V.O., Brzhezytskyi V.V., Isaiev V.V., Kikalo V.M., Lapchenko A.M., Masliuchenko I.M., Trotsenko Ye.O. Mobile verification laboratory of voltage classes 0.22 ... 110 kV. *Metrolohichne zabezpechennya obliku elektrychnoyi enerhiyi: Mater. 6-yi nauk.-prakt. konf.* [Materials of the 6th Scientific and Technical Conference «Metrological maintenance of electric energy accounting»]. Kyiv, AVEGA Publ., 2007, pp. 202-204. (Ukr).

14. Bolotin I.B., Eidel L.Z. *Izmereniia v perekhodnykh rezhimakh korotkogo zamykaniia* [Measurements in transient short-circuit conditions]. Leningrad, Energiya Publ., 1981. 192 p. (Rus).

15. Atarod S., Brzhezytskyi V.O., Garan Ya.O., Masliuchenko I.M., Anokhin Yu.L. Characteristics of high voltage dividers designed for power quality measurement. *Scientific Works of National University of Food Techn*ologies, 2013, no.51, pp. 91-102. (Ukr).

16. Brzhezytskyi V.O., Desiatov O.M., Masliuchenko I.M., Yatsenko I.S. Frequency characteristics due to the nonidentical R, C-elements of the high voltage divider for measuring power quality. *Scientific Works of National University of Food Techn*ologies, 2017, vol.23, no.1, pp. 158-172. (Ukr).

17. Atarod S. *Udoskonalennya vysokovol'tnykh podil'nykiv postiynoyi ta zminnoyi napruhy (chastoty 50 Hts) Diss. cand. techn. nauk* [Improvement of high-voltage dividers direct and alternating voltage (frequency 50 Hz). Cand. tech. sci. diss.]. Kyiv, 2014. 134 p. (Rus).

Y.L. Anokhin[1], *Head of the Research Department of Electrical Quantities Measurement*,
V.O. Brzhezytskyi[2], *Doctor of Technical Science, Professor*,
Ya.O. Haran[2], *Engineer*,
I.M. Masliuchenko[2], *Candidate of Technical Science, Associate Professor*,
O.P. Protsenko[2], *Candidate of Technical Science, Associate Professor*,
Ye.O. Trotsenko[2], *Candidate of Technical Science, Associate Professor*,
[1] State Enterprise «Ukrmetrteststandart»,
4, Metrolohichna Str., Kyiv, Ukraine, 03168,
e-mail: hivolt@ukrcsm.kiev.ua,
phone +380 44 5263485
[2] National Technical University of Ukraine «Igor Sikorsky Kyiv Polytechnic Institute»,
37, Prosp. Peremohy, Kyiv, Ukraine, 03056,
e-mail: v.brzhezitskiy@ukr.net, garan.yaroslav@gmail.com, i.masluchenko@gmail.com, apro54@ukr.net, trotsenko@email.ua
phone +380 44 2367989

M.I. Baranov, S.V. Rudakov

APPROXIMATE CALCULATION OF BASIC CHARACTERISTICS OF PLASMA AT THE AIR ELECTRIC EXPLOSION OF METAL CONDUCTOR

Purpose. Obtaining approximate calculation correlations for determination of maximal values of temperature T_m, and pressures P_m at a shock wave and speed v_m distribution of a shock wave in the plasma products of air electric explosion (EE) of metall conductor under act of large impulsive current (LIC). Methodology. Theoretical bases of the electrical engineering, scientific and technical bases of electrophysics, thermal physics and electrophysics bases of powerful high-voltage impulse technique, related to the theory and practice of the phenomenon EE metallic explorer in gas environments under action of LIC. Results. New calculation correlations are got for approximate calculation in a local area of EE in atmospheric air of metallic explorer of maximal values of temperature T_m, pressures P_m and speeds of v_m of shock wave in "metallic plasma" appearing from an explosion under action of LIC of its conducting structure. It is set that numeral values of the sought after sizes of temperature T_m, pressures P_m and speeds v_m as it applies to air EE thin copper conductor under the action of LIC of the microsecond temporal range can arrive at a few ten of thousands of Kelvin, hundreds of technical atmospheres and thousands of meters in a second accordingly. It is shown that similar values of speed v_m of shock wave in "metallic plasma" are comparable at speed of detonation wave in hard explosives. An accent is in this connection done on expedience of application air EE thin short metallic conductors at injury of live ammunitions with an ordinary and nuclear explosive. The real technical suggestions are offered on a possible receipt in the discharge circuit of powerful high-voltage generator of LIC of condenser type of "record" (most) values of the examined descriptions of "metallic plasma" at air EE thin metallic conductors. Comparison of the obtained results is executed for the probed descriptions of plasma at air EE of the metal conductor with known in the world information in area of electrophysics and thermal physics EE metal in gas environments. Originality. The obtained new theoretical results in area of high-current electrophysics and high-temperature thermal physics extend our physical views about the phenomenon of EE in atmospheric air of thin metallic conductors under action of LIC of the nanosecond and microsecond duration. Practical value. Application of the calculation correlations obtained in practice for the indicated descriptions of "metallic plasma" will allow technicians-and-engineers in a certain measure to accelerate and improve adjusting of difficult electric charts of powerful high-voltage generator of LIC at a receipt in his discharge circuit by air EE of thin metal conductors required on protocol of lead through of heavy-current electrophysics experiments of parameters of plasma in the local zone of its explosion. References 14.
Key words: **powerful high-voltage generator of current pulses of condenser type, metallic conductor, high pulse current, electric explosion of conductor, plasma, temperature, pressure, speed of distribution of shock wave in the plasma products of explosion, calculation.**

Приведены результаты приближенного расчета максимальных значений температуры T_m, давления P_m и скорости v_m распространения ударной волны в «металлической плазме», образующейся при воздушном электрическом взрыве (ЭВ) тонкого металлического проводника под воздействием большого импульсного тока (БИТ). Показано, что при ЭВ в атмосферном воздухе тонкого медного проводника в разрядной цепи высоковольтного генератора БИТ микросекундного временного диапазона максимальные значения температуры T_m, давления P_m и скорости v_m в локальной зоне ее взрыва могут достигать соответственно нескольких десятков тысяч градусов кельвина, сотен технических атмосфер и тысяч метров в секунду. Сформулированы возможные пути получения в разрядной цепи мощной конденсаторной батареи высоковольтного генератора БИТ «рекордных» значений температуры T_m, давления P_m и скорости v_m. Библ. 14.
Ключевые слова: **мощный высоковольтный генератор импульсов тока конденсаторного типа, металлический проводник, большой импульсный ток, электрический взрыв проводника, плазма, температура, давление, скорость распространения ударной волны в плазменных продуктах взрыва, расчет.**

Introduction. The electric explosion (EE) of thin metal conductors in vacuum, gas and liquid media under the influence of a high pulsed current (HPC) flowing through them is currently widely used [1-9]: in experimental physics in the study of plasma; in nuclear engineering when creating local high-pressure zones; in high-voltage pulse technology (HVPT) in tests for the lightning strength of external and internal insulation of electric power equipment; in the HPC technique when creating fast circuit breakers of high-current circuits; in the technique of powerful pulsed light sources; in electrotechnologies in the production of micro- and nanopowders for the production of new composite materials; in electric discharge technologies for impact treatment of liquids and solids. The undesirable manifestation of EE of metal can be observed in the field of HVPT and HPC technique and with an unreasonable choice of the cross-sections of current-carrying parts of high-voltage high-current circuits of the corresponding equipment. Engineering personnel who carry out EE of thin metal conductors, usually in air and industrial water [4, 6] when debugging the required operating modes of used HVPT and predicting the devastating consequences

for HVPT from the possible EE of its metallic conductors, simplified and convenient in practical applying approximate relationships for the operative calculation of the maximum levels of the temperature T_m, the pressure P_m, and the velocity v_m of the propagation of the shock wave in the plasma products («metallic plasma»). However, as analysis of literary sources shows, insufficient attention is paid to obtaining such calculated ratios in the world. In this connection, obtaining approximate relations for the estimated quantitative determination of these parameters T_m, P_m and v_m is an actual applied scientific and technical problem both in the field of electrophysics and thermal physics.

The goal of the paper is obtaining approximate calculated relations for determining the maximum values of the temperature T_m, the pressure P_m in the shock wave, and the velocity v_m of propagation of the shock wave in the plasma products of the air electric explosion of a metallic conductor under the influence of a large pulse current.

1. Problem definition. Let us consider a thin metallic conductor of rectangular or cylindrical geometric shape located in the air under normal atmospheric conditions, along which HPC flows in its longitudinal direction from a high-voltage pulse energy source (for example, from a powerful charged low-inductance capacitor bank), whose amplitude-temporal parameters (ATPs) are sufficient to achieve in a conductive structure a conductor with a rectangular or circular cross section S_0 of the numerical value of the integral J_k a current, which is critical for the test conductor. By the current integral J_k we mean an integral defined in time t by an expression of the form

$$J_k = \int_0^{t_k} \delta_k^2(t)dt \,,$$ where $\delta_k(t)$ is the critical density of a

pulsed current in a conducting material of a conductor; t_k is the time of the EE of the conductor [3-6]. For definiteness, we note that for a copper conductor in air at room temperature 20 °C, the critical value of the indicated current integral J_k is numerically about $11.95 \cdot 10^{17}$ A^2·s·m^{-4} [3]. In addition, it should be borne in mind that for EE of metallic conductors, «fast» HPC generators are commonly used whose ATPs change in time according to the law of a damped sinusoid [6, 8]. When a critical value of the current integral J_k is reached in the conductor, the conducting structure of the latter will be subjected to an EE accompanied by rapid evaporation and sublimation of its material [3-6]. We assume that the density $\delta_k(t)$ of the pulse current has a uniform distribution along the cross section of the conductor under consideration [4]. We assume that at the initial stage of the EE of the thin conductor, the maximum values of the temperature T_m and the pressure P_m of the «metallic plasma» are uniformly distributed over the cross section of the sublimated material of the conductor, which is still within its section S_0 [3, 4]. We

assume that the temperature T_m is determined by the electron plasma temperature, which, in turn, is determined by the heat flow density g_m in the conductor cross-section S_0. The initial air surrounding the conductor before its EE and the «metallic plasma» formed in place of the solid body of the conductor under study are assumed to be ideal gas media that satisfy the classical concept of an «ideal gas» with its limited volume [10]. Taking into account the normal atmospheric conditions to the EE of the conductor, the following basic characteristics for the initial air can be used [10]: the air pressure is $P_1 \approx 1.013 \cdot 10^5$ Pa; the air temperature was equal to $T_1 \approx 273.15$ K; the molar volume of air is $V_{M1} \approx 22.41 \cdot 10^{-3}$ m^3/mol. We confine ourselves to a quasi-static adiabatic process in the local zone around an electrically exploding metal of a conductor with a HPC flowing along it, in which there will be no heat exchange processes with the surrounding volume of the conductor with air surrounding the conductor [3, 4]. Taking into account the assumed assumptions, it is necessary to obtain approximate relations for the engineering estimation of the maximum values of the temperature T_m, the pressure P_m, and the velocity v_m of the propagation of the shock wave in the plasma products of air EE of the metallic conductor under the influence of HPC.

2. Calculated estimation of the maximum temperature T_m in the «metallic plasma» at the air EE of the conductor. Applying the Stefan-Boltzmann law to the plasma under consideration [10], for its temperature T_m we write the following calculated relation:

$$T_m \approx (\pi \sigma_c^{-1} g_m)^{1/4} \,, \tag{1}$$

where $\sigma_c = 5.67 \cdot 10^{-8}$ W·(m^2·K^4)$^{-1}$ is the Stefan-Boltzmann constant which characterizes the equilibrium thermal radiation of the «metallic plasma» in the EE region.

To find the value of the greatest heat flux density g_m in the «metallic plasma» formed from the EE of the conductor, we use the following electrophysical relation [11]:

$$g_m \approx \delta_{mk} U_e, \tag{2}$$

where $\delta_{mk} \approx I_{mk}/S_0$ is the amplitude of the critical current density in a conductor at its EE; I_{mk} is the amplitude of the current flowing through the conductor at the time of its EE; U_e is the near-electrode voltage drop in the edge zones of a sublimated conductor numerically not exceeding 10 V [12] for its basic metals used in HVPT and HPC technique.

In (2), the amplitude of the impulse current I_{mk} in the high-current discharge circuit of the high-voltage HPC generator with the conductor under investigation can be found from the following approximate expression [8]:

$$I_{mk} \approx (2 J_k S_0^2 I_m \omega)^{1/3} \,, \tag{3}$$

where I_m is the amplitude of the discharge current in the electrical circuit of the HPC generator, which varies with time t with a circular frequency ω determined by the

electrical parameters of the discharge circuit of the generator.

Then, from (1) – (3), for the maximum temperature Tm in the «metallic plasma» for air EE of a thin metal conductor under the influence of the HPC flowing through it in the final form, we obtain the following approximate relation:

$$T_m \approx \left[\pi \sigma_c^{-1} U_e (2 J_k S_0^{-1} I_m \omega)^{1/3} \right]^{1/4} . \quad (4)$$

It follows from (4) that in order to obtain the «record» (largest) temperatures T_m in the «metallic plasma» formed in the air EE of the conductor due to the action of the HPC on it, the conductor material should be chosen with the largest values of J_k and U_e, the cross-section S_0 the conductor is required to be taken as the smallest, while the amplitude I_m and the circular frequency ω (the rate of increase) of the pulsed current in the discharge circuit of the HPC generator are the largest. That is why, in order to achieve high T_m temperatures, it is advisable to use HPC generators with low-inductance and low-resistance discharge circuits and short thin electrically exploding conductors through which a pulse exponentially decaying sinusoidal current of nanosecond time range occurs.

The calculated estimation from (4) of the numerical value of the temperature T_m of the «metallic plasma» for the experimental case of air EE of a thin circular copper conductor of radius $r_0 \approx 0.1$ mm and length $l_0 \approx 110$ mm under the influence of the HPC of the microsecond time range described in [8] ($J_k \approx 1.95 \cdot 10^{17}$ A$^2 \cdot$s$\cdot$m^{-4}; $U_e \approx 10$ V; $S_0 \approx 3.14 \cdot 10^{-8}$ m^2; $I_m \approx 190$ kA; $\omega \approx 26.18 \cdot 10^3$ s^{-1}) shows that in the considered approximation it will be approximately equal to $92.67 \cdot 10^3$ K. To compare this calculated temperature T_m of the «metallic plasma» with the world-known data in the field of thermal physics of the EE of a metal, we indicate , according to the results of theoretical studies given in [13], the maximum explosion temperature in a vacuum of a lithium conductor ($2r_0 \approx 0.127$ mm, $l_0 \approx 10$ mm) included in the discharge circuit of a high-voltage HPC generator with the stored in its capacitors electric energy in it 100 kJ, at the time of introduction of thermal energy into the conductor of 200 ns, reached a numerical value of about $113.54 \cdot 10^3$ K.

It should be pointed out that in [3] the experimental numerical values of the critical current integral J_k are given, only for aluminum and copper conductors. In [14], data were presented for calculating the value of J_k for other conductive materials used in HVPT and HPC technique for EE of thin metals when the current density δ_k in them is not less than 10^{10} A/m^2.

3. Calculated estimation of the maximum pressure P_m in the «metallic plasma» at the air EE of the conductor. Taking into account the assumed assumptions and the equation of state of an ideal gas corresponding to the Clapeyron-Mendeleyev equation [10], for one mole of the air medium surrounding the metal conductor under investigation before the HPC is

exposed to it and one mole of the «metallic plasma» in the air after the air EE of the conductor under consideration, write the following gas equation:

$$P_1 V_{M1} / T_1 = P_m V_{M2} / T_m = R , \quad (5)$$

where $R = 8.314$ J/(K·mol) is the universal gas constant [10]; V_{M2} is the molar volume of plasma products in the local zone of EE in the air of the conductor being studied, caused by the action of the HPC on it.

To determine V_{M2} in (5), we use the following approximate relation [10]:

$$V_{M2} \approx (M_1 + M_2) / d_2 , \quad (6)$$

where M_1, M_2 are, respectively, the molar mass of the initial air and the «metal plasma» formed in it in the local zone of the air EE of the metallic conductor; d_2 is the density of plasma products formed in the air local area after the EE of the conductor under the influence of HPC.

For the density d_2 of plasma products after the air EE of the metallic conductor, in the first approximation, we use a relationship of the form:

$$d_2 / d_1 \approx (M_1 + M_2) / M_1 , \quad (7)$$

where $d_1 \approx 1.293$ kg/m^3 is the density of the received initial air surrounding the conductor before its EE [10].

According to (7), at the air EE of copper conductor ($M_1 \approx d_1 \cdot V_{M1} \approx 28.97 \cdot 10^{-3}$ kg/mol; $M_2 \approx 63.55 \cdot 10^{-3}$ kg/mol [10]) it follows that $d_2 \approx 4.129$ kg/ m^3. It can be seen that in this case the plasma products from the explosion of copper are only about 3.2 times denser than the initial air.

From (6) and (7) for the molar volume V_{M2} of plasma products after EE in the air of a metallic conductor, in the approximation obtained we obtain:

$$V_{M2} \approx M_1 / d_1 \approx V_{M1} \approx 22.41 \cdot 10^{-3} \text{ m}^3/\text{mol}. \quad (8)$$

Taking into account (8), from (5) for the required pressure P_m in the «metallic plasma» we find:

$$P_m = P_1 T_m / T_1 . \quad (9)$$

After substituting (4) into (9) for the maximum shock wave pressure P_m in the local EE zone in the air of the metallic conductor caused by the action on its conductive material of HPC, we have:

$$P_m \approx P_1 T_1^{-1} \left[\pi \sigma_c^{-1} U_e (2 J_k S_0^{-1} I_m \omega)^{1/3} \right]^{1/4} . \quad (10)$$

From (10) for the described above in Section 2 case of EE in air ($P_1 \approx 1.013 \cdot 10^5$ Pa; $T_1 \approx 273 15$ K) of the thin copper conductor with the microsecond HPC ($r_0 \approx 0.1$ mm; $l_0 \approx 110$ mm; $S_0 \approx 3.14 \cdot 10^{-8}$ m^2; $\sigma_c = 5.67 \cdot 10^{-8}$ W·(m^2·K^4)$^{-1}$; $J_k \approx 1.95 \cdot 10^{17}$ A$^2 \cdot$s$\cdot$m^{-4}; $U_e \approx 10$ V; $I_m \approx 190$ kA; $\omega \approx 26.18 \cdot 10^3$ s^{-1}) it follows that in this case a shock gas-dynamic pressure of up to $P_m \approx 343.7 \cdot 10^5$ Pa (up to 339.3 atm) will appear in the local zone of its explosion. According to (9) and (10), in order to obtain the largest values of the shock pressure P_m in the local air EE zone of the metallic conductor, it is necessary to create «record» levels of the absolute temperature T_m of the «metallic plasma» in this zone (this zone). For this purpose it is required to use the smallest cross sections S_0 of short conductors, as well as «fast»

HPC generators reproducing the largest amplitudes I_m and the circular frequencies ω of their discharge current.

4. Calculation estimation of the maximum velocity v_m of a shock wave in the «metallic plasma» at the air EV of the conductor. In the analyzed electrophysical case, the expression for the maximum velocity v_m of propagation of the shock wave in the plasma products of the air EE of the metallic conductor can be represented in the form [10]:

$$v_m \approx (\gamma_a R T_m)^{1/2}, \qquad (11)$$

where γ_a is the dimensionless adiabatic index.

Taking into account (4), the approximate relation (11) for the maximum velocity v_m of the shock longitudinal wave in the «metallic plasma» from the EE in the air of the conductor takes the following final form:

$$v_m \approx (\gamma_a R)^{1/2} \left[\pi \sigma_c^{-1} U_e (2 J_k S_0^{-1} I_m \omega)^{1/3} \right]^{1/8}. \qquad (12)$$

As for the numerical value in (11) and (12) of the dimensionless adiabatic index γ_a, for the equilibrium heat-radiating system «high-current plasma discharge channel-air» it is approximately equal to $\gamma_a \approx 4/3$ [10]. Then for the case of the air EE of the thin copper conductor used in [8] ($r_0 \approx 0.1$ mm; $l_0 \approx 110$ mm; $S_0 \approx 3.14 \cdot 10^{-8}$ m^2; $U_e \approx 10$ V; $J_k \approx 1.95 \cdot 10^{17}$ A$^2 \cdot$s·m^{-4}; $\sigma_c = 5.67 \cdot 10^{-8}$ W·(m^2·K^4)$^{-1}$) in the discharge circuit of the high-voltage generator of microsecond HPC ($I_m \approx 190$ kA; $\omega \approx 26.18 \cdot 10^3$ s^{-1}) from (12) we find that the maximum velocity v_m of the shock wave in the plasma explosion products reaches a numerical value of about 4020 m/s. With the calculated estimations by (11), (12) for the maximum values of v_m, it should be remembered that by modulus 1 mol, for example, for copper, according to the laws of molecular physics, is numerically $63.55 \cdot 10^{-3}$ kg [10] (remember that the dimension of the mole enters the universal gas constant R). Non-observance of the rules of the theory of dimensions in the practical application of the calculated relations (11) or (12) can lead to incorrect quantitative results for the sought value of the velocity v_m. The estimated numerical value of the maximum velocity $v_m \approx 4020$ m/s of the gas-dynamic shock wave in the «metallic plasma» obtained according to (12) corresponds to the velocity of the detonation wave in «slow» solid explosives [9, 10]. In this connection, from the point of view of the possible attainment of these high velocities v_m of the shock wave in plasma products of EE of metal, it seems expedient to use the air EE of thin metal conductors in high-efficiency electric detonators.

It follows from (12) that in order to obtain the «record» values of the velocity v_m of a shock wave in the «metallic plasma» at the EV in the air of the conductors under consideration, it is necessary to use the minimum possible cross-sections S_0 of short metal conductors, as well as the maximum possible values for the high-voltage HPC generator of the amplitude I_m and the circular frequency ω (the rate of increase) of its pulse discharge current which varies in time t according to the law of a damped sinusoid.

Conclusions.

1. New relations (4), (10) and (12) are obtained for the engineering calculation, respectively, of the maximum values of the absolute temperature T_m, the shock pressure P_m and the velocity v_m of the propagation of the shock wave in the «metallic plasma», formed from the air EE of the metallic conductor under the action of the flowing on it HPC.

2. It is shown that for the EE in the air of thin metallic conductors connected in the discharge circuit of the high-voltage generator of HPC of the microsecond time range, the maximum calculated values of the temperature T_m, pressure P_m and velocity v_m can reach numerical values of several tens of thousands Kelvin, hundreds of technical atmospheres and thousands of meters per second.

3. On the basis of the calculated relationships (4), (10) and (12), real technical proposals for obtaining with the help of the EV in atmospheric air of thin metal conductors «record» (largest) values of the temperature T_m, the pressure P_m and the shock wave velocity v_m in the local zone of their explosion under the influence of HPC.

4. The new theoretical results obtained for certain assumptions for the required values of the temperature T_m, the pressure P_m, and the velocity v_m allow us to deepen our physical representations in the field of high-current electrophysics and high-temperature thermal physics for the phenomenon of air EE of a thin metal conductor under the influence of the HPC of nano- and microsecond duration.

5. Taking into account the high calculated values of the velocity v_m of the shock wave in the «metallic plasma», it can be concluded that the practical application of air EE of thin short metal conductors in high-efficiency electric detonators is advisable.

REFERENCES

1. Mesiats G.A. *Impul'snaia energetika i elektronika* [Pulsed power and electronics]. Moscow, Nauka Publ., 2004. 704 p. (Rus).

2. Dashuk P.N., Zayents S.L., Komel'kov V.S., Kuchinskiy G.S., Nikolaevskaya N.N., Shkuropat P.I., Shneerson G.A. *Tehnika bol'shih impul'snyh tokov i magnitnyh polej* [Technique large pulsed currents and magnetic fields]. Moscow, Atomizdat Publ., 1970. 472 p. (Rus).

3. Knopfel' G. *Sverkhsil'nye impul'snye magnitnye polia* [Ultra strong pulsed magnetic fields]. Moscow, Mir Publ., 1972. 391 p. (Rus).

4. Stolovich N.N. *Elektrovzryvnye preobrazovateli energii* [Electroexplosion energy converters]. Minsk, Nauka & Tehnika Publ., 1983. 151 p. (Rus).

5. Burtsev V.A., Kalinin N.V., Luchynskiy A.V. *Elektricheskiy vzryv provodnikov i ego primenenie v elektrofizicheskikh ustanovkakh* [Electric explosion of conductors and its application in electrophysical options]. Moscow, Energoatomisdat Publ., 1990. 288 p. (Rus).

6. Gulyi G.A. *Nauchnye osnovy razriadno-impul'snykh tekhnologii* [Scientific basis of the discharge-pulse technology]. Kiev, Naukova Dumka Publ., 1990. 208 p. (Rus).

7. Lerner M.I. Formation of nano-sizes phase at the electric explosion of explorers. *Russian Physics Journal*, 2006, vol.49, no.6, pp. 91-95.

8. Baranov M.I., Lysenko V.O. The main characteristics of an electric explosion of a metallic conductor at high impulse currents. *Electricity*, 2013, no.4, pp.24-30. (Rus).

9. Baranov M.I. An anthology of the distinguished achievements in science and technique. Part 40: The scientific opening of the method of explosive implosion for the obtaining above critical mass of nuclear charge and Ukrainian «track» in the «Manhattan» American atomic project. *Electrical engineering & electromechanics*, 2017, no.5, pp. 3-13. **doi: 10.20998/2074-272X.2017.5.01.**

10. Kuz'michev V.E. *Zakony i formuly fiziki* [Laws and formulas of physics]. Kiev, Naukova Dumka Publ., 1989. 864 p. (Rus).

11. Baranov M.I. *Izbrannye voprosy elektrofiziki: Monografija v 2-h tomah. Tom 2, Kn. 1: Teorija elektrofizicheskih effektov i zadach* [Selected topics of Electrophysics: Monograph in 2 vols. Vol. 2, book. 1: Theory of electrophysics effects and tasks]. Kharkov, NTU «KhPI» Publ., 2009. 384 p. (Rus).

12. Raiser Yu.P. *Fizika gazovogo razryada* [Physics of gas discharge]. Moscow, Nauka Publ., 1987. 592 p. (Rus).

13. Rose K. *Maksimal'naya temperatura vzryva provolochek v vakuume / V kn. per. s angl.: Elektricheskiy vzryv provodnikov* [The maximum temperature of a wire explosion in a vacuum / In book trans. with English: Electric explosion of conductors]. Moscow, Mir Publ., 1965, pp. 43-46. (Rus).

14. Baranov M.I. Analytical calculation of critical values of integral of current for parent metals, applied in the technique of large impulsive currents at the electric explosion of explorers. *Technical Electrodynamics*, 2008, no.6, pp. 14-17. (Rus).

M.I. Baranov[1], *Doctor of Technical Science, Chief Researcher,*
S.V. Rudakov[2], *Candidate of Technical Science, Associate Professor,*
[1] Scientific-&-Research Planning-&-Design Institute «Molniya», National Technical University «Kharkiv Polytechnic Institute», 47, Shevchenko Str., Kharkiv, 61013, Ukraine,
phone +380 57 7076841,
e-mail: baranovmi@kpi.kharkov.ua
[2] National University of Civil Protection of Ukraine, 94, Chernyshevska Str., Kharkiv, 61023, Ukraine,
phone +380 57 7073438,
e-mail: serg_73@i.ua

G.V. Bezprozvannych, A.V. Roginskiy

THE STABILITY MONITORING OF THE MANUFACTURING PROCESS OF ELECTRICAL INSULATING SYSTEMS OF TRACTION ELECTRIC MACHINES

Introduction. Electrical insulation systems make up about 0.03 % of the traction electric machines (TEM) mass, but they are of exceptional importance and affect the design capabilities and manufacturing techniques of electric machines, ultimately - on their specific weight and overall dimensions, on the reliability and durability of the TEM. Purpose. The monitoring of the stability of the manufacturing process of electrical insulating systems of the TEM based on the insulation resistance measurements. Methodology. The analysis of the manufacturing process is carried out for three versions of the case of insulation of the magnetic system of the DC traction electric motor. Practical value. Construction and analysis of special graphs (charts) of individual values and cumulative sums of insulation resistance, sliding range MR allow to find out whether the technological process of manufacturing electric insulating systems of traction electric machines is in a statistically controllable state. References 11, tables 1, figures 4.*
Key words: **traction electrical machines, electrical insulation systems, insulation resistance, cumulative sum control chart, manufacturing process stability.**

Показано, что сопротивление изоляции может служить информативным параметром стабильности технологического процесса изготовления электроизоляционных систем тяговых электрических машин. Установлено, что сопротивление изоляции находится в пределах ±3σ относительно среднего значения каждой выборки трех вариантов исполнения электроизоляционной системы. Представлены контрольные карты индивидуальных значений и кумулятивных сумм сопротивления изоляции магнитной системы тяговых электродвигателей постоянного тока. Библ. 8, табл. 1, рис. 4.
Ключевые слова: **тяговые электрические машины, электроизоляционные системы, сопротивление изоляции, контрольные карты кумулятивных сумм, стабильность технологического процесса.**

Introduction. Electrical insulation systems make up about 0.03 % of the mass of traction electric machines (TEM) but they have an exceptional importance and influence the possibilities of design solutions and the technology of manufacturing electric machines, as a result – on their specific weight and overall dimensions, for reliability and durability of TEM. Improvement of electrical insulating composite systems of TEM is carried out by creating new, more progressive materials and technological processes [1].

Insulation resistance is an integral indicator of manufacturing process stability. Monitoring of product quality in the process of its production is always acute for producers. In modern production conditions, methods and procedures based on statistical analysis of product characteristics are used [2-4]. Quantitatively, the accuracy of manufacturing processes is estimated using the coefficient

$$K_T = \frac{6\sigma}{T},$$

where $T = T_{up} - T_{lower}$ is the tolerance of the product to the controlled parameter (the difference between the upper and lower values), σ is the standard quadratic deviation of the controlled quantity.

The accuracy of the manufacturing process is assessed based on the following criteria:

• at $K_T \leq 0.75$ – the manufacturing technological process is accurate;
• at $K_T = (0.75 - 0.98)$ – it requires close observation;
• at $K_T > 0.98$ – unsatisfactory.

The criterion for assessing the state of electrical insulating systems in production is the value of insulation resistance R_{ins}. This value is indicated in the normative and technical documentation [5]. Thus, for high-voltage electrical insulation systems of TEM, the insulation resistance R_{ins} relative to the housing (the lower threshold value) must be at least 20 MΩ in the cold state for machines with rated voltage above 400 V. The upper value of the insulation resistance is not regulated. Resistance of insulation is an integral statistical characteristic, which depends, first of all, on the electrophysical properties of the composite system, and the technological process of manufacturing assembly units and the TEM itself. It should be noted that the peculiarity of the technological process of manufacturing TEM insulating systems is a high level of non-mechanized (manual) production.

The goal of the paper is monitoring of the stability of the technological process for the manufacture of electrical insulating systems of TEM based on the insulation resistance measurements in the production.

Monitoring the stability of the manufacturing process by control charts of individual values. The analysis of the manufacturing process is carried out for three versions of the case insulation of the magnetic system of the DC traction electric motor. In each of the three versions of the housing insulation – by 12 samples each differing in the number of layers and the type of insulation tapes. Insulation resistance measurements were made with a MI 2077 teraohmmeter at constant voltage of 2500 V.

Fig. 1,*a* presents the results of measurements, Fig. 1,*b* – statistical characteristics of the insulation resistance of the three versions of the housing insulation. The statistical spread of the measured insulation resistance values (Fig. 1,*b*) within each version of the insulation system is associated with at least two reasons [6]. The

first one is due to unavoidable random measurement errors and the impossibility of absolutely accurate reproduction of test conditions. The second reason is deeper and consists in the fact that the insulation resistance reflects the existing structural and technological defects in the insulation system, and is associated with unhomogeneous insulation material, technological equipment, personnel qualification.
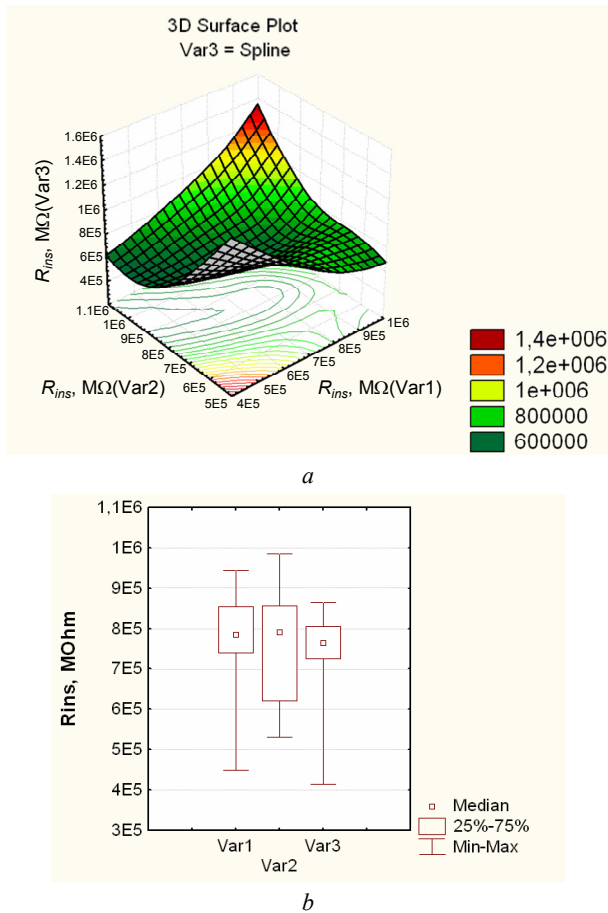

a

b

Fig. 1. Samples of insulation resistance of three versions of the housing insulation system

For all three options, the insulation resistance is within $\pm3\sigma$ of the nominal (mean) value for each sample (Fig. 2), which corresponds to the concept of «Six Sigma» [7].

In the production process, one of the main monitoring tools is the control charts (or Shewhart control charts) that visualize the statistical characteristics of the manufacturing process under investigation [4, 8]. Control charts of individual quantities (Fig. 3) allow to detect deviations (*X*) or sliding range (*MR*) of insulation resistance which are due to non-accidental reasons.

When using maps of individual values, the control limits are calculated on the basis of a measure of variation obtained from the sliding ranges of two observations. The sliding range (*MR*) is the absolute value of the measurement difference in consecutive pairs (the difference between the first and second measurements, the second and third ones, etc.).

On the basis of sliding ranges, the average sliding range is calculated, which is used to build control charts.

The lower and upper boundaries on the chart (Fig. 3, dot-dash lines) are at a distance of $3*\sigma$ from the mean (central line). Here, there are no systematic shifts (trends), nor any other signs of the process exit from control: the points of both charts fluctuate evenly (based on visual analysis) relative to the corresponding midlines. The points on both control charts are inside the control limits. The value of the second measurement is close enough to the lower control limit, but against the background of a general positive picture this is not an alarming event.
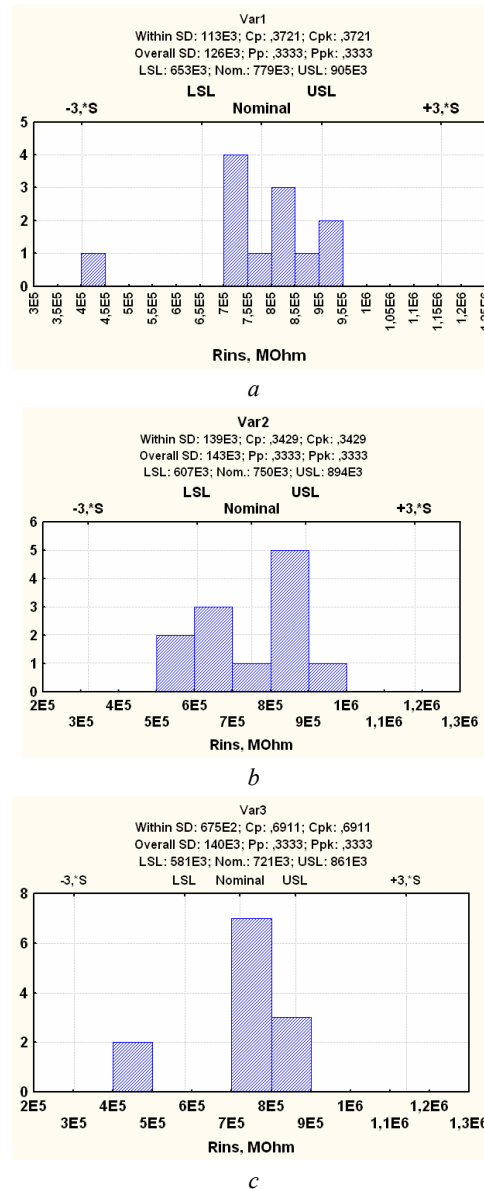

a

b

c

Fig. 2. On homogeneity of insulation resistance samples

To specify the criteria for finding a series of points, the area of the individual control chart above the central line and below it is divided into three «zones»: A, B and C [4]. By default, zone A is defined as a region located at distance from $2*\sigma$ to $3*\sigma$ on either side of the center line. Zone B is a region spaced from the central line at a distance from $1*\sigma$ to $2*\sigma$, and the zone C is the region located between the central line on both sides of it and bounded by a straight line drawn $1*\sigma$ away from the central line.
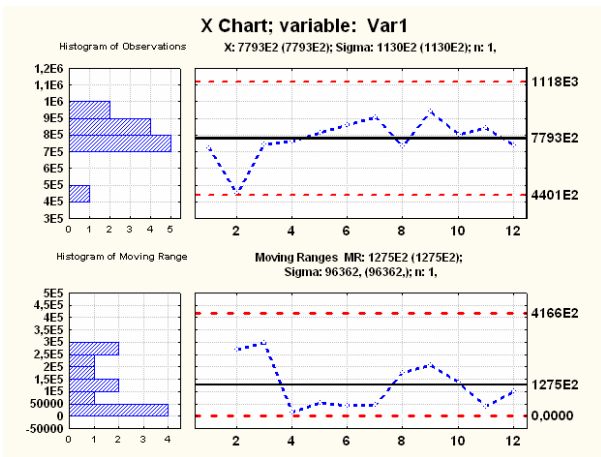
Fig. 3. A control chart of individual values of insulation resistance and sliding ranges for version 1 of the housing insulation system

Depending on the number of points and their location in one of the zones of the control chart, seven criteria are established.

When a criterion is fulfilled in the table of testing results, the row corresponding to this criterion is highlighted in red, and instead of *OK* in the columns, the numbers of points that fall into the risk zone are indicated (Table 1).

The results of testing (Table 1) performed for the *MR*- control chart (Fig. 3) and for the other two versions of the housing insulation show that under all criteria of testing the manufacturing process by insulation resistance, the investigated indicators are in statistically controllable state. There was no signal about the need to take precautionary measures.

Table 1

Stability test results for the manufacturing process

| Zones A/B/C: (3.0/2.0/1.0)*σ	Variable var1 MR-chart Central line 127545.45 MΩ, σ = 96361.95 MΩ	
	from the sample	to the sample
9 points on one side of the central line	OK	OK
6 points of growth / decrease	OK	OK
14 points alternate upwards and down	OK	OK
2 out of 3 points in zone A or outside	OK	OK
4 out of 5 points in zone B or outside	OK	OK
15 points in zone C	OK	OK
8 points outside zone C	OK	OK

The control charts of cumulative sums (CuSum) [4] (Fig. 4) which represent the accumulated sums of deviations of individual values of the observed variable (insulation resistance) from the mean value have greater sensitivity to process disturbances.

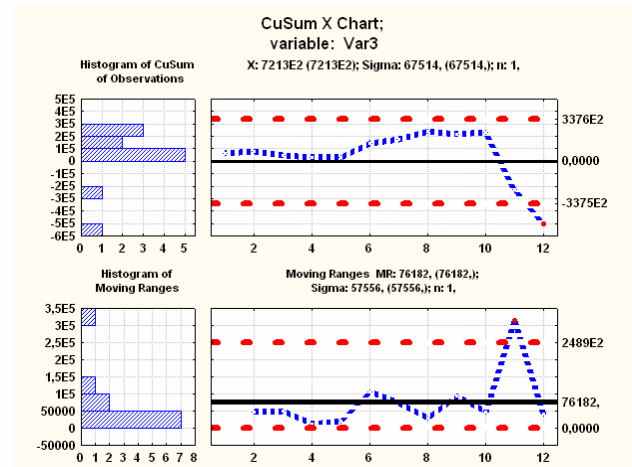Fig. 4 shows the control charts of cumulative (accumulated) sums for three versions of housing insulation. For the twelfth CuSum observation (Fig. 4,*c*), the pass from the lower boundary is noted and for the eleventh – from the upper one for the *MR* which can serve as a sign of the beginning of the manufacturing process disruption. Here, for this variant, the trend of sample values of CuSum also appears which requires clarification of the reasons for its appearance.
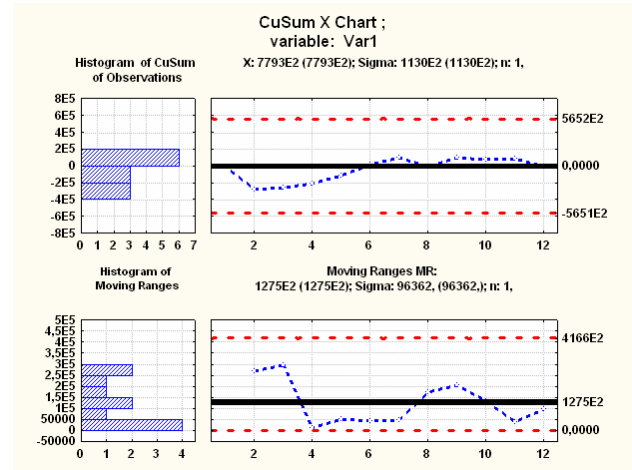
a
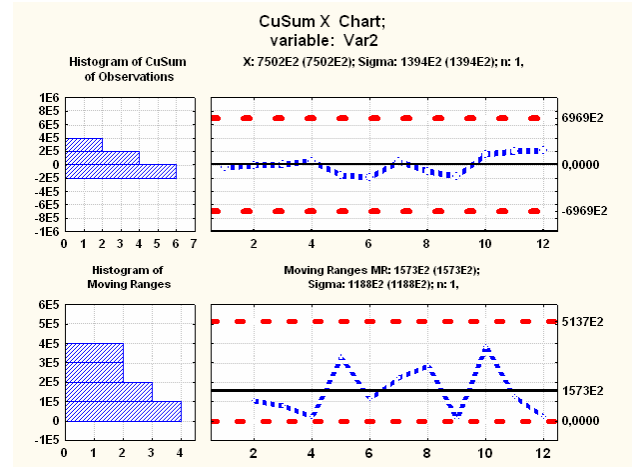
b

c

Fig. 4. Control charts of cumulative sums and sliding ranges of insulation resistance of three options of the casing insulation system

Conclusions. Construction and analysis of special graphs (charts) of individual values and cumulative sums of insulation resistance, sliding range *MR* allow to find out whether the technological process of manufacturing electric insulating systems of traction electric machines is in a statistically controllable state.

The presented monitoring procedure can be used to analyze the stability of technological processes for manufacturing electrical insulation systems of turbo and hydro generators.

REFERENCES
1. Ogonkov V.G., Serebryannikov S.V. *Elektroizoliatsionnye materialy i sistemy izoliatsii dlia elektricheskikh mashin. V dvukh knigakh. Kn. 2* [Electrical insulation materials and insulation systems for electrical machines. In 2 books. Book 2]. Moscow, Publishing house MEI, 2012. 304 p. (Rus).
2. Hartman K., Letsky E., Shefer V. *Planirovanie eksperimenta v issledovanii tekhnologicheskikh protsessov* [Planning an experiment in the study of technological processes]. Moscow, Mir Publ., 1977. 552 p.(Rus).
3. Draper N., Smith H. *Prikladnoi regressionnyi analiz. Mnozhestvennaia regressiia. Applied Regression Analysis* [Applied regression analysis. Multiple regression. Applied Regression Analysis. 3rd ed.]. Moscow, Dialectics Publ., 2007. 912 p. (Rus).
4. ISO 7870-4:2011. Cumulative sum charts – Guidance on quality control and data analysis using CUSUM techniques.
5. GOST 2582-2013. *Mashiny elektricheskie vrashchaiushchiesia tiagovye. Obshchie tekhnicheskie usloviia* [State Standart 2582-2013. Electric rotating traction machines. General specifications]. Moscow, Standardinform Publ., 2014. 56 p. (Rus).
6. Bezprozvannych A.V., Moscvitin E.S. Double-kink number as an indicator of degree of cable paper ageing. *Electrical engineering & electromechanics*, 2011, no.3, pp. 62-66. (Rus). **doi: 10.20998/2074-272X.2011.3.16.**
7. Eckes G. *Six Sigma Team Dynamics: The Elusive Key to Project Success*. Hoboken: John Wiley &Sons, 2003. 262 p.
8. Zolotarev V.M., Antonets Yu.A., Gurin A.G., Shebenyuk L.A., Golik O.V. Investigation of the correlation of electrical and mechanical parameters of double insulation of enamel wires. *Electrical engineering & Electromechanics*, 2005, no.2, pp. 78-80. (Rus).

G.V. Bezprozvannych[1]*, Doctor of Technical Science, Professor,*
A.V. Roginskiy[2]*, Postgraduate Student,*
[1] National Technical University «Kharkiv Polytechnic Institute»,
2, Kyrpychova Str., Kharkiv, 61002, Ukraine,
phone +380 57 7076010,
e-mail: bezprozvannych@kpi.kharkov.ua
[2] SE Plant Electrotyazhmash,
299, Moskovsky Ave., Kharkiv, 61089, Ukraine,
phone +380 50 5158552 49,
e-mail: roginskiy.av.@gmail.com

S.Yu. Shevchenko, N.A. Savchenko, A.V. Tretjak

MANAGING THE LOAD SCHEDULE OF THE ADMINISTRATIVE BUILDING TAKING INTO ACCOUNT EMERGING RISKS WHEN CONNECTING THE KINETIC ENERGY STORAGE TO THE POWER SUPPLY SYSTEM

Purpose. The purpose of the paper is to analyze load schedules of the administrative building and develop a structural scheme for connecting the kinetic energy storage in the power supply system of this building, which will allow using it as a consumer regulator, as well as a theoretical study of the risks that arise. Methodology. To conduct the research, the theory of designing internal electrical networks of buildings, the theory of plotting electric load graphs, methods of the theory of electromechanical systems and for analyzing the risk system, the T. Saati method of hierarchies were used. Results. The structure of kinetic energy storage (KES) connection to the power supply system of the administrative building is developed and the structural diagram of the KES proposed for installation is given, the average daily winter and summer load schedules are presented, a set of groups and subgroups of risks and their influence on the work of the power supply system of the building are connected with the connection of the KES. Originality. For the first time, the application of the kinetic energy storage in the power supply system of the building with the analysis of emerging risks is considered, which makes it possible to improve the reliability of the developed system and the efficiency of load regulation. Practical value. The application of the proposed scheme will make it possible to use administrative buildings as load regulators of the external power supply system, and also effectively manage the load in the internal power supply system of the building. References 9, tables 2, figures 4.
Key words: **power supply system, kinetic energy storage (KES), electric load schedule, risk system, consumer regulator**.

Цель. Целью статьи является разработка структурной схемы подключения кинетического энергонакопителя в систему электроснабжения административного здания, что позволит использовать это здание в качестве потребителя - регулятора, а также теоретическое исследование возникающих при этом рисков. Методика. Для проведения исследований использовались теория проектирования внутренних электрических сетей зданий, теория построения графиков электрической нагрузки, методы теории электромеханических систем и для анализа системы рисков метод иерархий Т. Саати. Результаты. Разработана структура подключения кинетического энергонакопителя (КЭН) в систему электроснабжения административного здания и приведены суточные графики нагрузок, исследован набор групп и подгрупп рисков и их влияние на работу системы электроснабжения здания при подключении КЭН. Научная новизна. Впервые рассмотрено применение кинетического энергонакопителя в системе электроснабжения здания с анализом возникающих рисков, что позволяет повысить надежность работы разработанной системы и эффективность регулирования нагрузки. Практическое значение. Применение предложенной схемы позволит использовать административные здания в качестве регуляторов нагрузки внешней системы электроснабжения, а также эффективно управлять нагрузкой во внутренней системе электроснабжения здания. Библ. 9, табл. 2, рис. 4.
Ключевые слова: **система электроснабжения, кинетический энергонакопитель (КЭН), график электрической нагрузки, система рисков, потребитель-регулятор.**

Introduction. The problem of covering non-uniform electric load schedules is currently being solved by three main methods [1]:

• creation of an optimal structure of generating capacities in the power system;

• use of overflows with neighboring power systems;

• attracting consumers to align the load schedule.

The Ukrainian power system is not an exception among other energy systems of the world and there is an imbalance in the generation and consumption of electricity. Thus, consumption during peak hours sometimes significantly exceeds generation capacity to cope with loads. To solve the existing problem, the implementation of various storage devices and accumulators in the power supply systems of consumers and the use of these consumers as load regulators in the power system can help.

To date, electrochemical batteries for energy storage which have a significant shortcoming –

fragility are widely used. Therefore, at present, as an alternative, many researchers propose the use of kinetic energy storage (KES) [2-6]. This device is intended for the storage of mechanical energy and its further transformation into electrical energy which can be used to regulate the load of the power system as a whole or its individual links.

At the moment, there are developments on the application of KES in autonomous power supply systems of buildings together with alternative energy sources [5, 6] and for energy storage in power systems [2, 4, 5].

Modern KES can store energy up to 20 MJ and produce power of 250-350 kW, while the size of the storage is small, and the efficiency is 85-90 % [9]. Also KES performs additional functions when operating in the customer's network, such as: implementation of a full galvanic isolation from the network, ensuring the quality of power supply, filtering distortion of harmonics and

voltage peaks, eliminating current micro breakdowns of duration less than 50 ms.

The use of KES for energy storage and load regulation is an important step in improving the energy efficiency of power supply systems. The stored energy can be used during peak hours for regulation purposes in power supply systems for administrative buildings which is attractive from an economic point of view, but this is due to a number of risks. The analysis of the risk system and their minimization is an important factor in improving the reliability of power supply systems.

The goal of the work is development of a structural scheme for connecting the kinetic energy storage to the power supply system of the administrative building to regulate the load of both the building itself and its use as a consumer – the load regulator of the power system as a whole.

Analysis of daily schedules of the administrative building (the 1st educational building of the Donbass National Academy of Construction and Architecture (DonNACA)). Daily schedules are necessary to record changes and obtain visual information about periods of peak load. They contain the information obtained on a certain day of the month and the season of the year. As the investigated object, the DonNACA educational building with a total area of $2,250 \text{ m}^2$ is considered, which includes classrooms and laboratories, a rector's office, a public catering enterprise equipped with electric cookers.

Daily fluctuations in consumption schedules and seasonal fluctuations are largely determined by meteorological factors: ambient air temperature, illumination, humidity, wind speed [7].

Analysis of the dynamics of electricity consumption shows (Fig. 1) that with increasing temperature and increasing illumination in summer, energy consumption is reduced [7]. As can be seen from the schedules, in the winter and summer for the object under study, we have the morning maximum load. The peak load falls on the period from 7.00 am to 2.00 pm. The minimum load is observed in the evening and at night between 6 pm and 7 am.
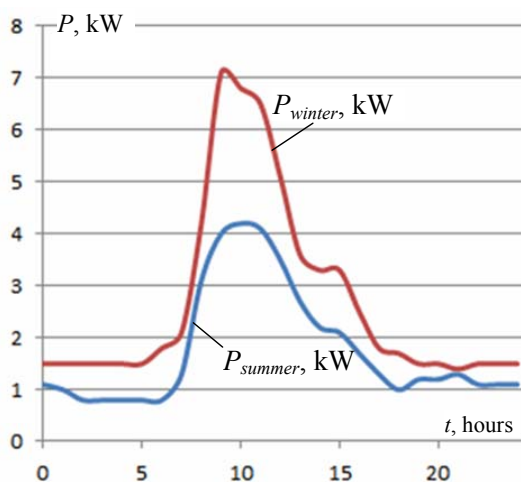

Fig. 1. Average daily load schedules of summer (P_{summer}) and winter (P_{winter}) days for the educational building

The connection of a KES to the power supply system of the building will give an opportunity to regulate (equalize) the load schedule of the building, namely, during the hours of load decay the KES will operate as an electric power consumer, and at peak hours as a generator that will allow the building to be used as a consumer – load regulator.

The scheme of connecting the KES to the power supply system of the administrative building. The developed structural scheme of connecting the KES to the power supply system of the administrative building, presented in Fig. 2, consists of a control unit (CU), kinetic energy storage (KES), load sensor (S), and inverter (I).

The operation is carried out as follows. At low load of the building, the value of which is controlled by the load sensor installed on the building supply line, automatic charging of the KES takes place. With increasing load in the building, the control unit (CU) switches the inverter to the generation mode synchronously with the network, feeding the building, after the load is reduced, the inverter turns off and the KES charging is performed.

Standard current transformers (CT) installed in the input node of electricity metering can serve as a current sensor. As a control unit (CU), you can use a programmable logic controller (PLC) with several analog inputs and outputs. If you need to connect to energy storage systems in other buildings or regional power system, you can use a controller with an Ethernet control channel.
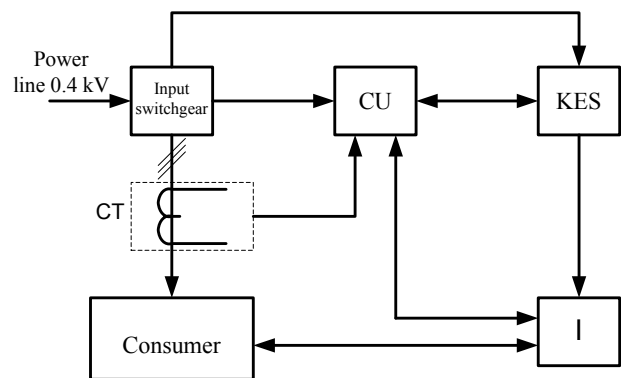

Fig. 2. The structural scheme of connecting the KES to the power supply system of the building

The KES consists of a storage flywheel (Fig. 3), a charging system motor M and a generator G, it is also possible to use a charging motor as a generator, but with a complicated switching system.

The power of the generator and the storage capacity of the flywheel are selected based on the value of the building's load. The charging system of the KES consists of an electric motor and a frequency converter (FC) operating in a closed system (with feedback). If it is necessary to charge the KES, the CU supplies the corresponding FC signal for start-up and the flywheel is accelerated with the set acceleration time parameters.

After the flywheel is completely accelerated, the FC maintains its stable rotation through feedback.
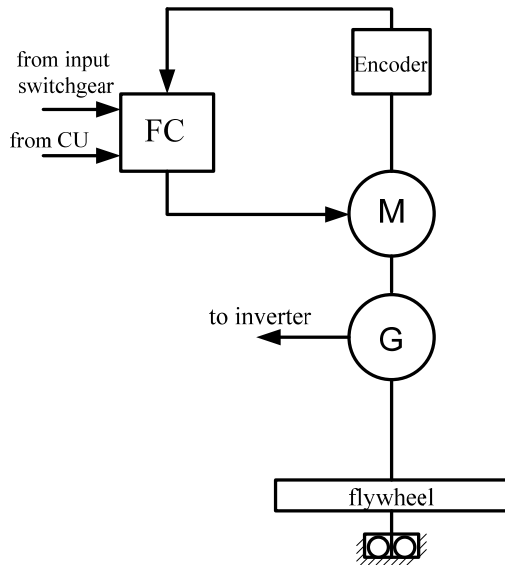

Fig. 3. The KES structural scheme

The charging motor of the KES and its FC is advisable to use of significantly less power than the generator, because charging takes a much longer time than discharge. This will reduce the price of the structure as a whole. The flywheel should be installed in a specially equipped pit near the building.

With increasing load in the building, the CU issues a command to the inverter (I) for the start, which, in turn, instructs the FC to stop feeding the KES. When the speed of the KES flywheel is reduced to a critical one, or the power consumption in the building is reduced, the inverter turns off automatically and, if possible, recharges the KES.

In order to increase the reliability and efficiency of the developed scheme of connecting the KES to the power supply system of the building, an analysis was made of the groups and subgroups of risks arising from the functioning of this system.

Analysis of risks in the operation of the power supply system of the building with KES. To determine and investigate common risks in the operation of power supply systems with the KES of administrative buildings, the hierarchy analysis method (HAM) developed by T. Saati was applied.

The hierarchy analysis method (HAM) is used to derive relationship scales from both discrete and continuous paired comparisons in multi-level hierarchical structures.

HAM has specific aspects related to the deviation of judgments from consistency and the measurement of this deviation, as well as the dependence within groups and between groups of elements of a hierarchical structure [8].

When using HAM for modeling, it is necessary to construct a hierarchical or network structure for the representation of the problem, then, pairwise comparing the elements of this structure, to obtain dominance matrices from which the scales of relations are derived.

In general, the hierarchical structure is composed from three levels: the first level – the goal from the point of view of management, the second level – the criteria on which the following levels depend, the third or the lowest level – the list of alternatives (Fig. 4).
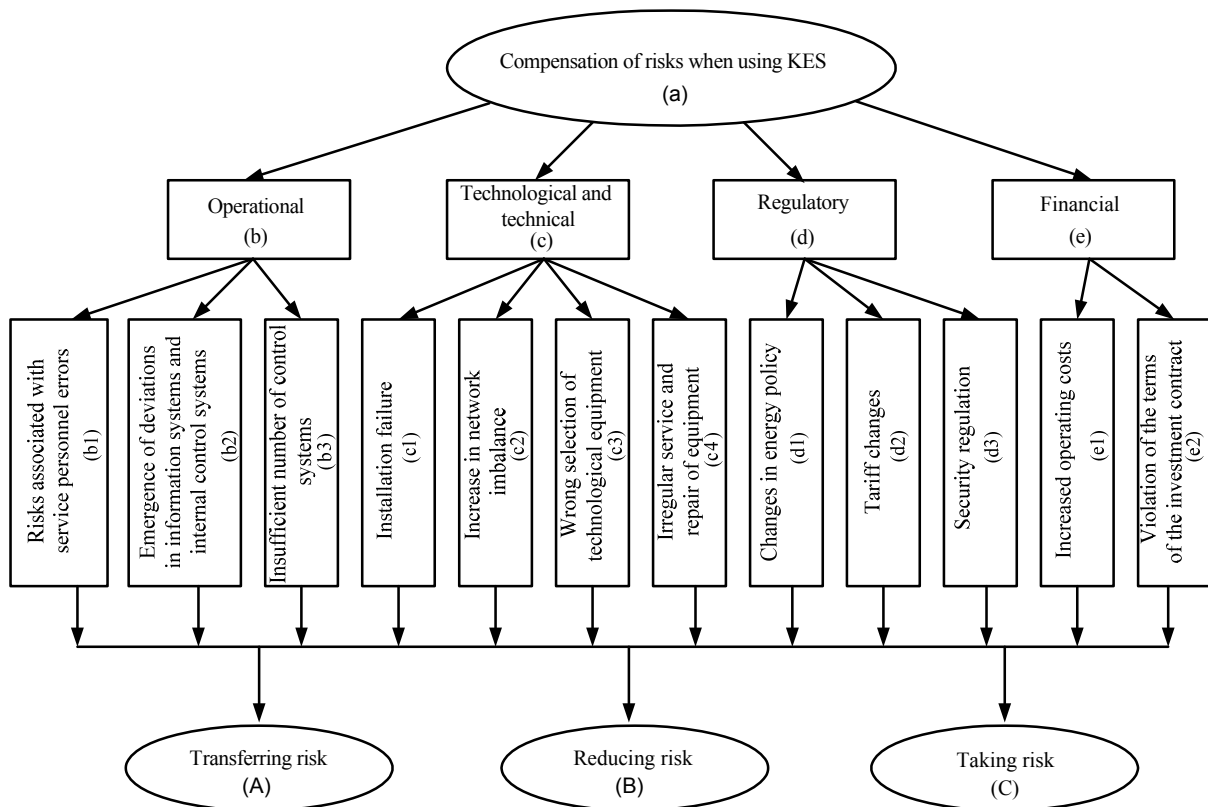

Fig. 4. A model of the hierarchical structure of risk analysis

The following notation is used in the model:

1. Purpose, or the main criterion (compensation of risks when using KES) – a.

2. Criteria for the first level (risk groups – operational, technological and technical, regulatory, financial) – b, c, d, e.

3. Criteria of the second level (subgroups of risks of the first level) – b1, b2, b3, c1, c2, c3, c4, d1, d2, d3, e1, e2.

4. Alternatives to achieving the goal (transferring risk, reducing risk, taking risk) – A, B, C.

The second stage of the HAM is the compilation of an algorithm for achieving the goal, namely: it is necessary to determine the impact of risk groups on the system as a whole. We use the technique described in [8] which consists in the following: firstly, matrices of pairwise comparisons of intermediate criteria with respect to higher-level criteria are written, for comparison, a scale of relative importance developed by T. Saati [8] is used; secondly, the transition from matched matrices to priority vectors is performed; thirdly, the quality of matrices of pairwise comparisons is checked, or the consistency index is calculated.

Expert data were used to compile the matrix of pairwise comparisons. The results of calculations of the matrix of pairwise comparisons of criteria for the first level of the hierarchy are presented in Table 1. In the same way, comparisons are made for the second level of the hierarchy.

Table 1

Determination of the most important risk group with a view to their compensation

Risk group	Operational	Technological and technical	Regulatory	Financial	Normalized estimates of the priority vector	Rang
Operational	1	1/3	4	1	0.2164	2
Technological and technical	3	1	5	3	0.5216	1
Regulatory	1/4	1/5	1	1/2	0.0801	4
Financial	1	1/3	2	1	0.1820	3
Total	5.25	1.86	12.00	5.50		
Consistency index CI = 0,024						
Consistency relation CR = 0.027 = 2.7 %						

According to the calculations, we have CR = 0.027 ≤ 0.1 which allows us to conclude that the assessments of experts in the matrix are consistent and do not need revision.

The main result of pairwise comparisons is the determination of the importance of alternatives which are given in Table 2.

Based on the results of the calculations, we have the highest estimation of 0.4427 for the alternative «reducing risk» – this is an opportunity to reduce the consequences of the occurrence of risks. Risks that can not be reduced or transferred are in second place and have the estimation of 0.3458. Risks that can partially be compensated by

transfer to the second responsible persons have the lowest estimation – 0.2115.

Table 2

Determination of the importance of alternatives

Alternative	Assessment of the importance of the alternative	Rang
Transferring risk	0.2115	3
Reducing risk	0.4427	1
Taking risk	0.3458	2

The performed analysis of the risk system shows that in order to increase the reliability and efficiency of the power supply system of a building with a connected KES, it is necessary to perform a number of administrative and technical measures to reduce technological, technical and operational risks, financial risks may be partially transferred to third parties (investors and insurance companies), and regulatory risks should be taken into account, as the impact on them is completely absent.

Conclusions.

1. The schedules of the load of a real building are given and analyzed. On the basis of the analysis, a method for regulating the load of a building and its simultaneous use as a consumer regulator is defined.

2. The structural scheme of connection of the kinetic energy storage to the power supply system of the building is developed which increases the efficiency of its operation and allows to regulate the load.

3. The analysis of the risk system at the use of kinetic energy storage in the building energy supply systems is carried out which will allow to minimize them and provide increased reliability of the power supply system.

REFERENCES

1. Gurtovtsev A.L., Zabello E.P. Electrical load of the power system. Aligning the schedule. *Electrical engineering news*, 2008, no.5(53). Available at: http://www.news.elteh.ru/arh/2008/53/19.php (Accessed 12 May 2017). (Rus).

2. Daoud M.I., Abdel-Khalik A.S., Massoud A., Ahmed S., Abbasy N.H. On the development of flywheel storage systems for power system applications: a survey. *2012 XXth International Conference on Electrical Machines*, Marseille, France, 2-5 September 2012, pp. 2119-2125. **doi: 10.1109/icelmach.2012.6350175.**

3. Yali Y., Yuanxi W., Feng S. The latest development of the motor/generator for the flywheel energy storage system. *2011 International Conference on Mechatronic Science, Electric Engineering and Computer (MEC)*, Jilin, China, 19-22 August 2011, pp. 1228-1232. **doi: 10.1109/mec.2011.6025689.**

4. Babuska V., Beatty S.M., deBlonk B.J., Fausz J.L. A review of technology developments in flywheel attitude control and energy transmission systems. *2004 IEEE Aerospace Conference Proceedings (IEEE Cat. No.04TH8720)*, Big Sky, MT, USA, 6-13 March 2004, pp. 2784-2800. **doi: 10.1109/aero.2004.1368076.**

5. Chen H., Cong T.N., Yang W., Tan C., Li Y., Ding Y. Progress in electrical energy storage system: A critical review. *Progress in Natural Science*, 2009, vol.19, no.3, pp. 291-312. **doi: 10.1016/j.pnsc.2008.07.014.**

6. Aljohani T.M. The flywheel energy storage system: a conceptual study, design, and applications in modern power systems. *International Journal of Electrical Energy*, 2014, vol.2, no.2, pp. 146-153. **doi: 10.12720/ijoee.2.2.146-153.**

7. Savchenko N.A., Shevchenko S.Yu. Determination of input parameters of the information base for load prognostication in distribution networks 6-10 kV. *Electrical networks and systems*, 2010, no.3, pp. 9-14. (Rus).

8. Saati T. *Priniatie reshenii. Metod analiza ierarkhii* [Making decisions. The method of analyzing hierarchies]. Moscow, Radio and Communication Publ., 1993. 278 p. (Rus).

9. Available at: http://www.atz gmbh.com/Products/HTS_bearing/Flywheel/body_flywheel.htm (accessed 15 September 2017).

S.Yu. Shevchenko[1], Doctor of Technical Science, Professor,
N.A. Savchenko[2], Postgraduate Student,
A.V. Tretjak[2], Postgraduate Student,
[1] National Technical University «Kharkiv Polytechnic Institute»,
2, Kyrpychova Str., Kharkiv, 61002, Ukraine,
phone +380 57 7076312,
e-mail: syurik42@gmail.com
[2] Donbas National Academy of Civil Engineering
and Architecture,
14, Geroev Nebesnoi Sotni Str., Kramatorsk, Donetsk region,
84333, Ukraine,
phone +380 62 6461999,
e-mail: natali_a_savchenko@ukr.net,
tretjak_a.v@ukr.net